# Molecular Dynamics study of structure and stability in Au nanoparticles

**A thesis submitted in fulfilment of requirements**

**for admission to the Degree of**

**Doctor of Philosophy**

**by**

**Yu Hang Chui**

**B.Sc., MPhil. (H. K.)**

**November 2007**

**Applied Physics**

**School of Applied Sciences**

**RMIT University**

**Melbourne, Australia**

This thesis is dedicated to:

My fiancé, parents and sister.

# Declaration

I certify that

- except where due acknowledgment has been made, this work is that of the author alone;

- this work has not been submitted previously, in whole or in part, to qualify for any other academic award;

- the content of this thesis is the result of work which has been carried out since the official commencement date of the approved research program;

  and

- any editorial work, paid or unpaid, carried out by a third party is acknowledged.

Yu Hang CHUI

# Acknowledgments

I would like to give my thanks to my supervisors, Salvy P. Russo and Ian K. Snook. I benefited a lot from their patient guidance, invaluable advice and encouragement throughout my research work. Their previous comments on the draft of this thesis are much appreciated.

Special thanks go to Greg Grochola and Robert J. Rees. They made the simulation and structural analysis available for the development of my research work.

I would like to thank the member of the simulation group at RMIT: Akin, Istvan, Ryan, Nicole, Manolo, Tobias, Shane, Terry, Michelle, David, Tanya, Tim and Peter. For administrative matter, I would like to thank Anjani, Geoff, Stan, Helen and Kaarina. Specially, I would like to thank Akin for sharing his studying and living experience in Australia with me, which is important to an overseas student like me.

I would like to formally acknowledge the Victorian Partnership for Advanced Computing (VPAC) and the Australian Partnership for Advanced Computing (APAC) for the computational time and the support from the staff therein.

My greatest debt lies with my parents for their support and encouragement throughout my formal and informal education, and also my research at RMIT University. Without them, I could not have overcome all the hurdles and complete my doctoral study. Finally, I wish to thank Melanie for her affection, encouragement during my research study in Australia. We lived together and experienced everything in Australia. Although we had some difficulties about our study and living, we solved the problem together and support with each other. Truly, these 3 years would be the most precious moment in my life.

Thanks all.

## Refereed Journal publications

- **Y. H. Chui**, R. J. Rees, I. K. Snook, B. O' Malley and S. P. Russo, Topological characterization of crystallization of gold nanoclusters, The Journal of Chemical Physics, 2006, **125**, 114703.

- G. Grochola, I. K. Snook, **D.Chui** and S. P. Russo, Exploring the effects of different immersion environments on the growth of gold nanostructures, Molecular Simulation, 2006, **32**, 1255-1260.

- **Y. H. Chui**, G. Grochola, I. K. Snook and S. P. Russo, Theoretical Study of Gold Nanostructures with unusual Morphologies, Journal of Computational and Theoretical Nanoscience, 2007, **4**, 291-298.

- **Y. H. Chui**, G. Grochola, I. K. Snook and S. P. Russo, Molecular dynamics investigation of the structural and thermodynamic properties of gold nanoclusters of different morphologies, Physical Review B, 2007, **75**, 033404.

- **Y. H. Chui**, I. K. Snook and S. P. Russo, Visualization and analysis of structural ordering during crystallization in a gold nanoparticle, Physical Review B, in press.

- **Y. H. Chui**, I. K. Snook and S. P. Russo, Molecular Dynamics study of crystallization of gold nanoparticles, The Journal of Physical Chemistry C, in preparation.

## Conference presentations

- **Y. H. Chui**, G. Grochola, S. P. Russo, I. K. Snook and D. E. Mainwarning, "Modelling structural morphology and free energies of gold nanoclusters", 16$^{th}$ Australian Institute of Physics (AIP) Congress (31 Jan 2005 – 5 Feb 2005), Australian National University, Australia.

- **Y. H. Chui**, I. K. Snook and S. P. Russo, "Simulations and Modeling of Zero- and One-dimensional Gold Nanostructures", 17$^{th}$ Australian Institute of Physics (AIP) Congress (3-8 Dec 2006), Brisbane Convention Centre, Australia.

- **Y. H. Chui**, I. K. Snook and S. P. Russo, "The EAM Method Applied to Au Nanostructures", Workshop: Interaction Energies and the Structure of Surfaces and Nano-structures (19-21 Feb 2007), RMIT University, Australia.

# Summary

The study of nano-scaled gold particles has been one of the topical areas in material science, as tiny gold particles give a wide range of potential applications in electronics, medicine and catalysis. In this thesis, gold nanostructures of 923 – 10179 atoms (3-8nm in diameters) were modeled and simulated using Molecular Dynamics and two atomistic potentials: the Embedded Atom Method (EAM) Glue potential and the Force-matching potential. Structure, stability and crystallization kinetics of the gold nanoparticles were studied at finite temperature. In our simulations, we found that the icosahedral morphology is dominant within the size range we considered, and this is supported by the recent high resolution Transmission Electron Microscopy (HRTEM) work on gold nanoparticles with the same size range produced in helium gas. According to our free energy calculations, we also find that the surface reconstruction of gold nanoclusters give rise to a higher thermodynamical stability. In addition, we investigated the crystallization kinetics of gold nanoparticles cooled from the melt. Following the evolution of our crystallization results indicated that crystallization of the surface precedes that of the core. The mechanism of the crystallization is clearly shown using the planar graph method.

# Table of Contents Page

## List of figures

**Page**

## List of tables Page

# Chapter 1

# Introduction

## 1.1 Gold nanostructures: Historical and Current Perspectives

### 1.1.1 Nano-scaled gold particles

Nano-scaled gold particles are believed to be one of the oldest nano-materials discovered in the history of mankind. Colloidal gold has been used since Ancient Roman times to colour glass an intense shades of yellow, red, or mauve, depending on the concentration of gold [1]. Between 1480 and 1486, a stained-glass window in the Milan Cathedral, Italy, showing the birth of St. Eligius, patron saint of gold smiths, was made by Niccolo da Varallo. A well-dispersed spherical gold colloid was used to generate red color in stained glass [2]. In the $16^{th}$ century, the alchemist Paracelsus claimed to have created a potion called Aurum Potabile (Latin: potable gold) [1]. In the $17^{th}$ century, Johann Kunckel developed the first systematic procedures for incorporating gold into molten silica, and produced the well-known “ruby glass” [1].

In 1842, John Herschel invented a photographic process called Chrysotype (from the Greek word for gold) that used colloidal gold to record images on paper. Paracelsus' work is known to have inspired Michael Faraday to prepare the first pure sample of colloidal gold, which he called 'activated gold', by electric discharge method, in 1857. He used phosphorus to reduce a solution of gold chloride. Faraday was the first to recognize that the colour was due to the minute size of the gold particles [3].

The first quantitative theoretical description of the colours of nanoscopic metal particles occurs in 1904 with the work of Maxwell-Garnett [4], who used expressions for spherical particle polarizability derived by Rayleigh and Lorenz to define effective

composite optical constants. On the other hand, in 1908 Gustav Mie represented the first rigorous theoretical treatment of the optical properties of spherical metal particles [5]. Mie's theory yielded extinction coefficients for nanoscopic gold particles which compared well with the experimental spectra of gold sols. In early $20^{th}$ century, the aqueous gold particles were model system for the study of colloidal stability and nucleation [6]. In 1951, the first solution synthesis method was proposed by Turkevitch et al. [1]. The method is used to produce spherical gold nanoparticles suspended in water of around 10–20 nm in diameter. Larger particles can be produced, but this comes at the cost of monodispersity and shape. The other solution synthesis method was discovered by Brust and Schifrinn in early 1990s [1], and can be used to produce gold nanoparticles in organic liquids that are normally not miscible with water (like toluene). On the other hand, the discovery of the surface-enhanced Raman scattering effect (SERS) sparked a renewed interest in the optics and physics of metal nanoparticles, including nanoscaled-gold particles. Although many workers were interested primarily in the SERS effect during mid-1970s to mid-1980s, their work provided important insights into the fundamental linear optical properties of metal nanoparticles [7]. Also, with the help of electronic microscope, the structure and dynamics of gold nanoclusters were also investigated in 1990s [8]. These initial studies provided a basic understanding of the structural and physical properties of gold nanoclusters from which we can proceed.

### 1.1.2 Recent investigations into gold nanoclusters

#### 1.1.2.1 Structural characterization

Recent work into the preparation and structural characterization of gold nanoclusters has proceeded steadily. Vogel et al. [9] have prepared stable gold clusters of around 1 nm in size by evaporation of the metal into an organo-silicon polymer solution. X-ray

diffraction and simulation calculations using Debye functions of model clusters of different sizes and both crystallographic and non-crystallographic symmetry were used to characterize these particles. Rousset et al. [10] produced supported Au clusters by laser vaporization of pure bulk gold. Transmission Electron Microscopy (TEM) and Energy Dispersive X-ray Spectroscopy (EDS) of these clusters gave the size distribution and binding energy of gold at the nano-scale. Benfield et al. [11] characterized the structure and bonding of gold clusters, colloids and nanowires by Extended X-ray Absorption Fine Structure (EXAFS), Extended X-ray Absorption Edge Structure (XANES) and wide-angle X-ray scattering (WAXS). These experimental methods are well-suited to characterizing the geometric and electronic structure of nanomaterials, and they showed a clear pattern of buildup of metallic structure and bonding as the number of gold atoms increases. Williams et al. [12] applied three-dimensional imaging to characterize microstructure in gold nanocrystals. The structural orientation inside the gold nanocrystals was investigated during their formation at high temperature.

Population distributions of gold nanoparticle morphologies were derived as a function of size by collecting a large number of high-resolution electron microscopy (HREM) images [13]. The gold nanoparticles were generated from an inert gas aggregation source using helium and deposited on amorphous carbon films. In the samples, icosahedral type particles dominated over other structural morphologies over the observed size range. Hernández et al. [14] determined the surface structure of gold nanoparticles and gold nanorods by studying the behavior of electrochemical reactions sensitive to the structure and compared their result to that obtained by other structure characterization techniques.

#### 1.1.2.2 Synthesis

Recently, room temperature, high-yield synthesis of multiple shapes of gold nanoparticles in aqueous solution has been proposed [15]. The morphology and dimension of gold nanoparticles could be varied by manipulation of the synthesis parameters at room temperature, and with reduced usage of surfactant. Jin et al. [16] demonstrated the thermally induced formation of gold clusters and conversion into nanocubes. These gold nanocubes can serve as building blocks on a substrate. Moreover, synthesis of novel shapes of gold nanocrystals, such as plates [17], tetrahedral [18], branched [19], ring [20], tadpole [21], cage [22], hollow sphere [23], rod [24], tube [25] and wire [26] have been reported. Different solution synthesis methods produce different types of shapes of gold nanoparticles. Gold nanoparticles with hexagonal (icosahedral) and pentagonal (decahedral) profiles were synthesized by vapor deposition methods [27]. Chen et al. and Hao et al. reported the synthesis of a mixture of branched gold nanocrystals by using two different colloid chemical synthesis protocols [28]. Scherer and co-workers found that gold nanoclusters they prepared can serve as building blocks allowing the synthesis of gold nanocubes on a substrate [29]. Ah et al. also found that on adjusting the reaction rates by insufficient addition of the reductant, the reaction proceeds in a two-step manner with self-seeding that results in the formation of gold nanoplates [30]. Sau and Murphy proposed a mechanism for the evolution of cylindrical rod shapes in aqueous solution by the seeded growth method [31]. Later on, using the same synthesis method, they produced a collection of morphologies (rod, cube, star, tetra-pod and multi-pod) and dimension of the gold nanoparticles at room temperature by manipulating the synthesis parameters (the concentration of seed gold particles and other reactants). For hollow gold nanostructures, Xia and co-workers synthesized gold nanocage of <40 nm using the galvanic replacement reaction between silver nanocubes and aqueous gold ions [32]. By

controlling the molar ratio between silver and gold ions, the gold void/pore size of gold nanocages and also the optical properties can be tuned.

Other than solution chemical synthesis method, the experimental generation of gold particles in solution can also be done by sonolysis [33]. In one such process based on ultrasound irridiation of an aqueous solution of $HAuCl_4$ containing glucose the reducing agents are hydroxyl radicals and sugar pyrolysis radicals (forming at the interfacial region between the collapsing cavities and the bulk water) and the morphology obtained is that of nanoribbons with width 30 -50 nm and length of several micrometers. Moreover, the gold nanoparticles with the diameters of 3-18 nm were generated from an inert gas aggregation (IGA) source using helium and deposited on amorphous carbon films [13]. Protected gold clusters were also generated by laser vaporization technique in gas phase [34].

A technique has been described very recently to make uniform one-dimensional arrays of tunable gold nanoparticles with tunable interparticle distances [35]. Additionly, periodic square-like gold nanoparticle arrays were templated by self-assembled 2D DNA nanogrids on a surface [36]. These gold nanoparticle arrangements are evenly distributed with accurate control of interparticle spacing. Such gold nanoparticle patterns may find practical applications in nanoelectronic and nanophotonic devices. Nikoobakht et al. [37] have generated and characterized self-assembled gold nanorods into one-, two- and three-dimensional structures under appropriate conditions.

Currently, there are two main types of synthesis of gold nanostructures: The inert gas aggregation (IGA) and solution synthesis. In IGA, bulk gold is heated and melted in vacuum and gold nanoparticles are generated in a source chamber by cooling gold vapours with purified helium [13]. In this project, we assume that there is only very weak Van der Waals' force between cooled gold clusters and helium gas and this inter-atomic force would not affect the formation and growth of gold nanoparticles. With the

assumption, we set up the simulations of model gold nanoparticles in a box without periodic boundary condition.

### 1.1.3 Potential applications

#### 1.1.3.1 Optics

When cluster sizes are comparable to the Fermi wavelength of an electron, the discrete energy levels of the nanoclusters become accessible and the optical properties are significantly modified [38-40]. The plasmon resonance excitation of gold nanoparticles gives rise to Raman-enhancing capabilities, intense colors and their utility as labels in bio-detection platforms [41]. The wavelength of the plasmon resonance can be tuned by the size and shape of the nanoparticle and also by its surrounding dielectric medium [42-44]. Surface passivated gold nanoclusters ranging in size from 28 atoms to small clusters (<1.2 nm) have been shown to have emission in the near-IR [45], visible red [46] and blue [47]. Recently, blue emission from water soluble Au8 with more than 100-fold enhancement in quantum yield has been reported [48]. For one-dimensional gold nanostructures, the longitudinal optical modes can be tuned to span across the spectral region from visible to near-infrared (NIR) by controlling their aspect ratios [49]. It is also found that a gold nanorod with an aspect ratio of 2.0 -5.4 could fluoresce with a quantum yield more than one million times than that of a metal [50]. These properties, combined with biological inertness, may make the practical application of zero-dimensional (0D) and one-dimensional (1D) gold nanodots as a novel fluorophore possible [48, 51].

For optics, gold nanoparticles usually display an intense colour due to surface plasmon resonance (SPR) scattering, which originates from the collective oscillation of their conduction electrons in response to photon excitation [52, 53]. Interestingly, the SPR band has been shown to strongly depend on their structure (solid vs. hollow) and on the

dielectric constant of the environment surrounding the particles [52, 54]. This dependence allows one to tune the spectral position of a SPR band, as well as to design new types of optical sensors.

Figure 1.1 compares the UV-vis extinction spectra of aqueous dispersions of gold solid particles (with a mean diameter of ~50nm) and nano-shells made of gold (with a core diameter of ~50nm and wall thickness of ~4.5nm) [52]. The solid colloids exhibited an intense, sharp peak at ~530 nm, while the SPR peak for nanoshells was broader and res-shifted to ~680 nm.

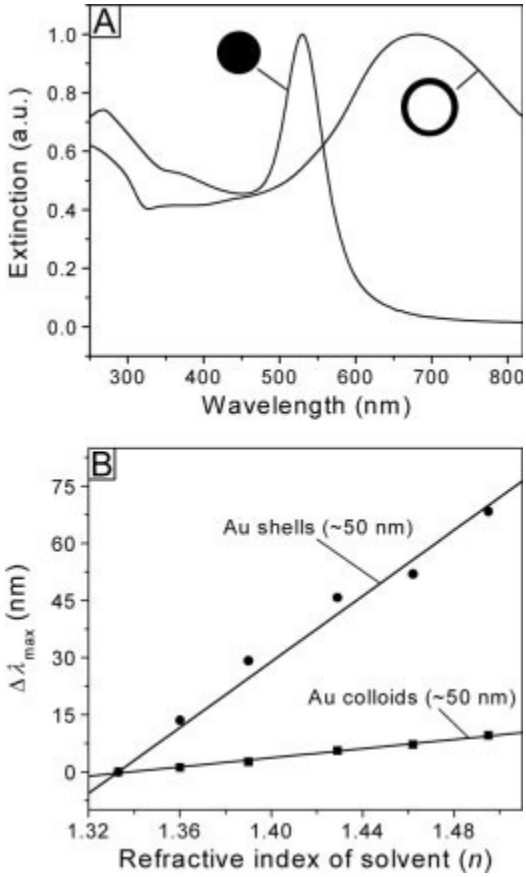


**Figure 1.1 [Reference 52]** a) A comparison between the UV-vis extinction spectra of Gold solid colloids (~50nm in diameter) and gold shells with core diameter of ~50nm and wall thickness of ~4.5nm). b) Plot of the dependence of peak shift ($\Delta\lambda_{max}$, relative to the peak position obtained with water as the dispersion solvent) on the refractive index (n) of surrounding medium. The sensitivity factors, $\Delta\lambda_{max}/\Delta n$, were ~60 and ~410

nm/RIU for ~50nm gold solid colloids and ~50nm gold nanoshells, repectively.

#### 1.1.3.2 Electronics

The electronic properties of one-dimensional gold nanostructures have been studied extensively and these nanostructures can be a wire as thin as a single linear chain of atoms and short in length [55]. These gold nanostructures are believed to be ideal for application as nano-devices based on the transport of charge, such as Field Effect Transistors (FETs) [41]. Recently, Searson's group [56] has reported the synthesis and characterization of single nanoporous gold nanowires. Adsorption of charged species on the surface of gold nanowire gives rise to a change in conductivity. This property may lead to potential application of single nanoporous gold nanowires as chemical sensors.

The structures of Au nanoparticles have been shown to affect the electronic properties decisively [57, 58]. For examples, a pronounced energy gap has been revealed by PES and DFT for a 20-atom Au cluster with a tetrahedral structure and atomic packing similar to that of bulk gold [59], and a metal-to-insulator transition is observed as the size of Au nanoparticles decrease below 3nm by measuring the tunneling current as a function of the bias voltage $(I\text{-}V)^2$ and by measuring the local barrier height (LBH) [58].

#### 1.1.3.3 Bio-detection and cancer treatment

Because of biological inertness, ability of bio-conjugation, rich and controllable optical properties, and a similar size scale to biological structures (viruses and bacteria) and molecules (proteins and DNA), gold nanoparticles of different sizes and shapes have drawn a great deal of attention in biomedical research.

Gold nanoparticles have been demonstrated to be potential materials in cell imaging [32, 60], targeted drug delivery [61], and cancer diagnostics and therapeutic applications [62-65]. One of the recent examples is that of gold nanocages of sizes smaller than 40

nm in dimension which were synthesized and bio-conjugated with antibodies. These functionalized nanocages have been demonstrated for specific targeting of breast cancer cells [32]. Compared to filled nanoparticle, there are two advantages of gold nanocages in biomedical application. First, their scattering and absorption coefficients can be easily varied by changing the void sizes and number of truncated corners. Second, the nanocages can be made extremely small (<50nm) while still exhibiting resonance peaks in the near-IR region. Also the size and shape dependence of a gold nanoparticle's uptake into mammailian cells has been studied [66].

#### 1.1.3.4 Catalysis

The catalytic activity of supported gold clusters was discovered by Haruta [67]. Now it has been known that the size of the gold nanparticles plays an important role with medium-sized gold particles with diameters of 2-4 nm being the most catalytically active [68-71]. The origins for the catalytic property of supported gold nanoparticles are still unknown. The catalytic activity of gold nanoparticles has been related to the existence of metallic strain, the presence of active sites due to surface defects, and also the unique electronic properties of gold nanoclusters compared to bulk gold [72-75].

For catalysis, the nature of active Au structures and sites remain unclear. In general, this originates from one or more of three contributions: (i) presence of low coordination Au sites; (ii) charge transfer between the support and Au; (iii) quantum size effects [76]. Here, we only discuss the factor (i) and (iii). Catalytically active Au has only been observed for Au particles less than 8nm in diameter, and the observed activities are highly dependent on the support materials. The low-coordination Au sites, such as corner or edge sites at the perimeter/contact area of the interface between the Au particles and the support are purported to serve as a unique reaction site where the reactant are activated [76].

Figure 1.2 shows the comparison of catalytic activities of supported Au thin film and nanoparticles for CO oxidation [77]. The blue bars of the histogram are the computed rates based on total Au. The rates obtained for the ordered bilayers are approximately 1 order of magnitude higher than the rates for the high-surface-area supported catalysts. The observation may arise due to (1) electronic effect caused by particle contact area, particle shape, etc. (2) a steric effect in that the reactants have multidirectional access to the bilayer structure but only unidirectional access to the Au nanoparticles. (3) the fact that various sizes and shapes of the nanoparticles coexist on the surface.

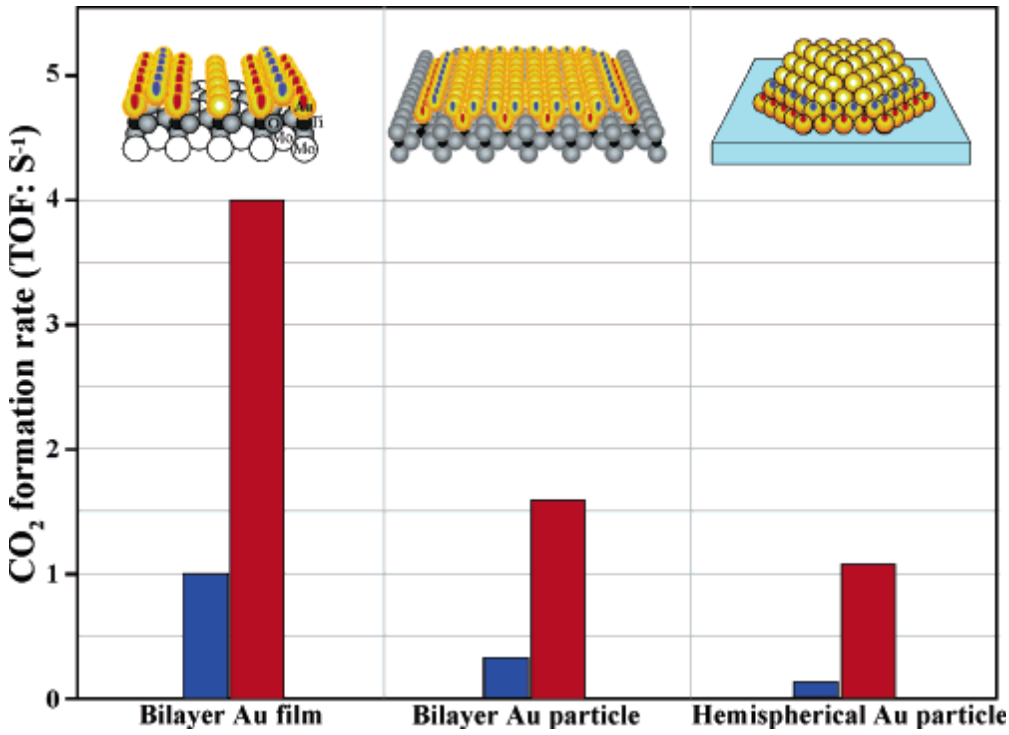


**Figure 1.2 [Reference 77]** Comparison of catalytic activities for CO oxidation on the Mo(112)-(1x3)-(Au,TiO2),Au/TiO2(110), and Au supported on high-surface-area TiO2 with a mean particle size of ~3nm. The inserts show structural models using red and blue marks to indicate the active sites.

#### 1.1.3.5 The importance of thermal stability of gold nanostructures to their applications

The thermal stability of gold nanostructures at finite temperatures is particularly important to their applications in optics, electronics, catalysis, medical therapies and drug delivery. For optics, electronics and catalysis, the thermal stabilities of their structures and shape at high temperatures are critical to their performances. For example, during heating of gold nanorod with using laser source, the shape transformation from rod to sphere may occur and the optical properties of gold nanoparticle would be dramatically changed.

For the medical purposes, the gold nanoparticles act as targeted thermal agent and could extend the precision of thermal effects below cellular dimension [78]. Gold nanoparticles are leading candidate materials for these applications because of their biocompatibility and because well-developed surface chemistries are available to functionalize Au nanoparticles for attachment to selected biological molecules or materials [79]. In the photothermal therapy, the functionialized gold nanoparticles are taken into the body of the patient and pass through several thermal gradients inside the human body. After getting into targeted cancer cell, the gold nanoparticles absorbs the near-infrared (NIR) laser energy from light source outside the human body, transforms the optical energy into thermal energy and effectively kill cancer cells, leaving the healthy cells unaffected [80]. Therefore, the theoretical would help understand the thermal behaviour of gold nnaoparticles of different sizes and shapes.

## 1.2 Theoretical studies of gold nanostructures

### 1.2.1 Zero-dimensional nanostructures

Theoretical studies on gold nanostructures have been performed for over 10 years. By the ab-initio approach, the geometrical and electronic structures of small gold clusters in zero- [81-87] and one- [88-91] dimension have been studied extensively.

For modeling using empirical (Embedded Atom) type potentials, the pioneering work was done by Ercolessi, Andreoni and Tosatti [92], in which the melting mechanism of small gold particles of different sizes was studied using the 'Glue' potential [93], which they developed. For the first time, they provided a microscopic description of the melting transition of metal clusters, revealing the formation of a liquid skin as precursor effect for N > 350 atoms. Also, the experimentally observed sharp decrease of the melting temperature with decreasing size was recovered. Later, Lewis, Jensen, and Barrat studied the melting, freezing and coalescence of gold nanoclusters using the Embedded-Atom Method (EAM) [94]. Again, they found that melting begins at the surface then proceeds inwards. Moreover, Cleveland et al. [95] revealed the thermal evolution of these clusters is punctuated by diffusionless solid-to-solid structural transformation from the low-temperature optimal structures to icosahedral structures.

Recently, the melting of gold nanoclusters has been further studied and new information was provided. Liu et al. [96] found that the melting process has three characteristic time periods for the intermediate sized nanoclusters. The whole process includes disordering and reordering, followed by surface melting and then overall melting. Wang et al. [97] investigated the surface melting of Mackay icosahedral gold clusters. They found that the facets on the cluster surface soften but do not pre-melt below the bulk melting temperature. The surface softening would lead to inter-layer and intra-layer diffusion, and shrinkage of the average facet size. As a result, the cluster is nearly spherical at

melting.

On the other hand, in studying freezing of gold nanoparticles with Molecular Dynamics, Shim et al. [98] showed that with decreasing cooling rate, the final structure of the particle changes from amorphous to crystalline via an icosahedron-like structure. While Nam et al. [99] demonstrated the formation of an icosahedral structure through a surface-induced mechanism. Just after freezing, ordered nanosurfaces with a five-fold symmetry were formed with an interior atom remaining in the disordered state. Further lowering of the temperature induced crystallization of core atoms that proceeded from the surface towards the core region, finally leading to an icosahedral structure.

### 1.2.2 One-dimensional nanostructures

The structure, phase transition, thermal stability and mechanical properties of one-dimensional nanostructures have been studied by Molecular Dynamics. Gold nanowires were first investigated via classical simulations by Bilabegović [100]. After this, the structural evolution of gold nanowires of different diameters was investigated [101]. Recently, the local structure of one-dimensional gold nanowires has been studied by Hui et al [102].

In addition to structural properties, phase transitions in one-dimensional gold nanostructures have been modeled. Recently, surface-stress-induced phase transformation in gold nanowires has been predicted using the EAM potential [103]. It was found that the transformation of nanowires could be controlled by the wire size, initial orientation and temperature.

For thermal stability, Wang et al. [104] studied the melting behavior of helical multiwalled cylindrical gold nanowires using Molecular Dynamics. They found that the interior melting temperature in nanowires is lower than that of the surface melting temperature. Wang and Dellago [105] also simulated shape transition of gold nanorods

exposed to low-energy laser pulses. A mechanism was suggested that explains the intermediate structures and internal defects of gold nanorods observed in laser heating experiments.

Finally, mechanical properties of gold nanowires are important for their applications to nano-devices and strength, yield stress and Young's modulus of the nanowires have been studied in detail [106].

### 1.2.3 First-principle study of gold nanostructures

Other than the classical simulations of gold nanostructures, the first-principle methodology has been widely applied to gold nanostructures. Although the computational power nowadays has been greatly enhanced, the electronic structure calculation of the clusters consisting of heavy metal atom like gold is very computationally expensive, and the size of gold clusters is limited to less than 100 atoms. Wang et al. calculated lowest-energy structures and electronic properties of Au clusters consisting of 2-20 atoms [107], and Landman and co-workers investigated the electronic and atomic structures of small anionic gold clusters consisting of 4-14 atoms [108]. After these, hollow gold nanoclusters, such as Au32 [109], Au42 [83] and Au50 [110] have been predicted to be stable theoretically. On the other hand, the ligand protected gold nanoclusters (Au20 and Au38), which have been synthesized in the experiments, were also investigated by ab-initio calculation [59, 111].

## 1.3 The aim of this thesis

Many classical theoretical studies of zero-dimensional gold nanostructures have been performed. Although the melting and freezing processes were extensively studied, and in different studies different structures at different sizes were predicted to be the most possible or energetically stable one by different atomistic potentials, the change of the

structural preference of gold nanoparticles with the sizes is still not clearly understood. By studying the formation kinetics and thermodynamics of these kinds of gold nanostructures of different sizes in details, the problems about the structural properties of gold nanostructures may be solved.

There are 6 Chapters in this thesis. In Chapter 1, the introduction, we have given a justification of why the study of gold nanoparticles is important. In Chapter 2, simulation and analytical methods used to model and analyze the gold nanoparticles crystallized from the melt using Molecular Dynamics are described. Chapter 3 gives an account of how different analytical methods are applied to study the structural properties of gold nanoparticles. In Chapter 4, the thermodynamics of gold nanoparticles of different sizes and morphologies were studied. In Chapter 5 we described the crystallization kinetics of gold nanoparticles. Finally in Chapter 6 we summarize the main conclusions and describe avenues for future work in this area.

**References**

[1] "Colloidal gold", Wikipedia.

(Available at http://en.wikipedia.org/wiki/Colloidal_gold)

[2] C. J. Murphy, Science **298**, 2139-2141 (2002).

[3] M. Faraday, Philos. Trans **147**, 145 (1857); L. P. Williams, The Selected Correspondence of Michael Faraday, Vol. 2, Cambridge University Press, London, 1971.

[4] J. C. Maxwell-Garanett, Philos. Trans. R. Soc. A **203**, 385 (1904).

[5] G. Mie, Ann. Phys. **25**, 377 (1908).

[6] H. B. Weiser, Inorganic Colloid Chemistry, Vol.1, Wiley, New York, 1933.

[7] M. Meier and A. Wokaum, Optics Lett. **8**, 851 (1983); E. J. Zeman and G. C. Schatz, J. Phys. Chem. **91**, 634 (1987); P. W. Barber, R. K. Chang and H. Massoudi, Phys. Rev. B **27**, 7251 (1983).

[8] A. Pinto, A. R. Pennisi, G. Faraci, G. D'Agostino, S. Mobilio and F. Boscherini **51**, 5315 (1995); W. Krakow, M. Jóse-Yacamán and J. L. Aragón, Phys. Rev. B **49**, 10591 (1994).

[9] W. Vogel, J. Bradley, O. Vollmer and I. Abraham, J. Phys. Chem. B **102**, 10853-10859 (1998).

[10] J. L. Rousset, F. J. Cadete Santos Aires, B. R. Sekhar, P. Mélinon, B. Prevel and M. Pellarin, J. Phys. Chem. B **104,** 5430-5435 (2000).

[11] R. E. Benfield, D. Grandjean, M. Kröll, R. Pugin, T. Sawitowski and G. Schmid, J. Phys. Chem. B **105**, 1961-1970 (2001).

[12] G. J. Williams, M. A. Pfeifer, I. A. Vartanyants and I. K. Robinson, Phys. Rev. Lett. **90**, 175501 (2003).

[13] K. Koga and K. Sugawara, Surf. Sci. **529**, 23-25 (2003).

[14] J. Hernández, J. Solla-Gullón, E. Herrero, A. Aldaz and J. M. Feliu, J. Phys. Chem. B **109** 12651-12654 (2006).

[15] T. K. Sau and C. J. Murphy, J. Am. Chem. Soc. **126**, 8648-8649 (2004).

[16] R. Jin, S. Egusa and N. F. Scherer, J. Am. Chem. Soc. **126** 9900-9901 (2004).

[17] C. S. Ah, Y. J. Yun, H. Y. Park, W. –J. Kim, D. H. Ha and W. S. Yun, Chem. Mater. (2005).

[18] H. –F Zhang, M. Stender, R. Zhang, C. Wang, J. Li and L. –S. Wang, J. Phys. Chem. B **108**, 12259-12263 (2004).

[19] E. Hao, R. C. Bailey, G. C. Schatz, J. T. Hupp and S. Li, Nano Letts. **4**, 327-330 (2004); C.-H. Kuo and M. H. Huang, Langmuir **21**, 2012-2016 (2005).

[20] Y. Sun and Y. Xia, Adv. Mater. **15**, 695- 699 (2003).

[21] J. Hu, Y. Zhang, B. Liu, J. Liu, H. Zhou, Y. Xu, Y. Jiang, Z. Yang and Z. Tian, J. Am. Chem. Soc. **126**, 9470-9471 (2004).

[22] J. Chen, F. Saeki, B. J. Wiley, H. Cang, M. J. Cobb, Z. –Y. Li, L. Au, H. Zhang, M.

B. Kimmey, X. D. Li and Y. Xia, Nano Lett. **5**, 473-477 (2006).

[23] H. –P. Liang, L. –J. Wan, C. –L. Bai and L. Jiang, J. Phys. Chem. B **109**, 7795-7800 (2005).

[24] Y. Y Yu, S. –S. Chang, C. L. Lee and C. R. C. Wang, J. Phys. Chem. B **101**, 6662-6664 (1997); T. K. Sau and C. J. Murphy, Langmuir **20**, 6414-6420 (2004).

[25] Y. Oshima, A. Onga and K. Takayanagi, Phys. Rev. Lett. **91**, 205503 (2003); M. A. Sanchez-Castillo, C. Couto, W. B. Kim and J. A. Dumesic, Angew. Chem. Int. Ed. **43**, 1140-1142 (2004).

[26] Y. Kondo and K. Takayanagi, Science **289**, 606-608 (2000).

[27] M. J.Yacaman, J. A. Ascencio, H. B. Liu and J. Gardea-Torresday, J. Vac. Sci. Technol. B **19**, 1091-1103 (2001); C. Y. Yang, K. Heineman, M. J. Yacaman and H. Poppa, Thin Solid Films **58**, 163-168 (1979); A. Renou and M. Gillet, Surf. Sci. **106**, 27-34 (1981).

[28] S. Chen, Z. L. Wang, J. Ballato, S. H. Foulger and D. L. Carroll, J. Am. Chem. Soc. **125**, 16186-16187 (2003); E. Hao, R. C. Bailey, G.. C. Schatz, J. T. Hupp and S. Li, Nano Lett. **4**, 327-330 (2004).

[29] R. Jin, S. Egusa and N. F. Scherer, J. Am. Chem. Soc. **126**, 9900-9901 (2004).

[30] C. S. Ah, Y. J. Yun, H. J. Park, W.-J. Kim, D. H. Ha and W. S. Yun, Chem. Mater. **17**, 5558-5561 (2005).

[31] T. K. Sau and C. J. Murphy, J. Am. Chem. Soc. **126**, 8648-8649 (2004).

[32] J. Chen, F. Saeki, B. J. Wiley, H. Cang, M. J. Cobb, Z. –Y. Li, L., Au, H. Zhang, M. B. Kimmery, X. Li, Y. Xia, Nano Lett. **5**, 473-477 (2005).

[33] J. Zhang, J. Du, B. Han, Z. Liu, T. Jiang and Z. Zhang, Angew. Chem. Int. Ed. **45**, 1116 - 1119 (2006).

[34] J. Cyriac, V. R. Rajeev Kumar, T. Pradeep, Chem. Phys. Lett. **390**, 181-185 (2004).

[35] M. K. Corbierre, J. Beerens, J. Beauvais and R. B. Lennox, Chem. Mater. **18**, 2628-

2631 (2006).

[36] J. P. Zhang, Y. Liu, Y. G.. Ke and H. Yan, Nano letts. **6**, 248-251 (2006).

[37] B. Nikoobakht, Z. L. Wang and M. A. El-Sayed, J. Phys. Chem. B **104**, 8635-8640 (2000).

[38] S. Empedocles and M. Bawendi, Acc. Chem. Res. **32**, 389-396 (1999).

[39] M. A. El-Sayed, Acc. Chem. Res. **34**, 257-264 (2001).

[40] S. Link and M. A. El-Sayed, Int. Rev. Phy Chem. **19**, 409-453 (2000).

[41] E. K. Payne, K. L. Shuford, S. Park, G. C. Schatz and C. A. Mirkin, J. Phys. Chem.B **110**, 2150-2154 (2006).

[42] C. F. Bohren and D. R. Huffman, Absorption and Scattering of Light by Small Particles; John Wiley & Son: New York (1998).

[43] P. Mulvaney, Langmuir **12**, 788 (1996).

[44] U. Kreibig, B. Schmitz, H. D. Brewer, Phys. Rev. B **36**, 5027 (1987).

[45] S. Link, A. Beeby, S. FitzGerald, M. A. El-Sayed, T. G.. Schaaff, R. L. Whetten, J. Phy. Chem. B **106**, 3410-3415 (2002).

[46] T. Huang and R. W. Murray, J. Phy. Chem. B **105**, 12498-12502 (2001).

[47] J. P. Wilcoxon, J. E. Martin, F. Parsapour, B. Wiedenman, D. F. Kelley, J. Chem. Phys. **108**, 9137-9143 (1998).

[48] J. Zheng, J. T. Petty, and R. M. Dickson, J. Am. Chem. Soc. **125**, 7780-7781 (2003).

[49] Y. Xia, P. Yang, Y. Sun, Y. Wu, B. Mayers, B. Gates, Y. Yin, F. Kim and H. Yan, Adv. Mater. **15**, 354-389 (2003).

[50] M. B. Mohamed, V. Volkov, S. Link, M. A. El-Sayed, Chem. Phys. Lett. **317**, 517 (2000).

[51] Y. Sun and Y. Xia, Anal. Chem. **74**, 5297 (2002).

[52] Y. Sun, B. Mayers and Y. Xia, Adv. Mater. **15**, 641- 646 (2003).

[53] C. F. Bohren and D. R. Huffman, Absorption and Scattering of Light by Small

Particles, Wiley, New York (1983).

[54] M. D. Malinsky, K. L. Kelly, G.. C. Schatz and R. P. van Duyne, J. Am. Chem. Soc. 123, 1471 (2001); F. Cocchini, F. Bassani, M. Bourg, Surf. Sci. **156**, 851 (1985); P. Mulvaney, L. M. Liz-Marzán, M. Giersig, T. Ung, J. Mater. Chem. **10**, 1259 (2000); S. Underwood and P. Mulvaney, Langmuir, **10**, 8427 (1994).

[55] A. L. Yanson, G. R. Bollinger, H. E. van den Brom, N. Agrgit, J. M. van Ruitenbeek, Nature **395**, 783 (1998).

[56] C. Ji and P. C. Searson, J. Phys. Chem. B **117**, 4494-4499 (2003); Z. Liu and P. C. Searson, J. Phys. Chem. B **110**, 4318-4322 (2006).

[57] M. C. Daniel and D. Astruc, Chem.Rev. **104**, 293-346 (2004);

[58] Y. Maeda, M. Okumura, S. Tsubota, M. Kohyama, M. Haruta, Appl. Surf. Sci. **222**, 409-414 (2004).

[59] J. Li, X. Li, H. –J. Zhai, L. –S. Wang, Science **299**, 864- 867 (2003)

[60] S. Shukla, A. Priscilla, M. Banerjee, R. R. Bonde, J. Ghatak, P. V. Satyam and M. Sastry, Chem. Mater. 17, 5000-5005 (2005).

[61] P. –H. Yang, X. Sun, J. –F. Chiu, H. Sun and Q. –Y. He, Bioconjugate Chem. 116, 494-496 (2005).

[62] L. R. Hirsch, R. J. Stafford, J. A. Bankson, S. R. Sershen, B. Rivera, R. E. Price, J. D. Hazle, N. J. Halas, J. L. West, Proc. Natl. Acad. Sci. U.S.A **100**, 1549-1554 (2003).

[63] C. Loo, A. Lin, L. Hirsch, M. H. Lee, J. Barton, N. Halas, J. West, R. Brezek, Technol. Cancer Res. Treat. **3**, 33-40 (2004).

[64] J. Chen, B. Wiley, D. Campbell, F. Saeki, L. Cang, L. Au, J. Lee, X. Li and Y. Xia, Adv. Mater. **17**, 2255 (2005).

[65] J. F. Hainfeld, D. N. Slatkin, H. M. Smilowitz, Phys. Med. Biol. **49**, N309-N315 (2004).

[66] B. D. Chithrani, A. A. Ghazani and W. C. W. Chan, Nano Lett. **6**, 662-668 (2006).

[67] M. Haruta, T. Kobayashi, H. Samo and N. Yamada, Chem. Lett., 405-408 (1987).

[68] P. Schwerdtfeger, Angew. Chem. **115**, 1936-1939 (2003); P. Schwerdtfeger, Angew. Chem. Int. Ed. **42**, 1892-1895 (2003).

[69] M. Haruta, Catal. Today **36**, 153-166 (1997).

[70] G. C. Bond, Catal. Today **72**, 5-9 (2002).

[71] R. Grisel, K. –J. Weststrate, A. Gluhoi, B. E. Nieuwenhuys, Gold Bull. **35**, 39-45 (2002).

[72] M. Valden, X. Lai and D. W. Goodman, Science **281**, 1647 (1998).

[73] M. Mavrikakis, P. Stoltze, J. K. Norskov, Catal. Lett. **64** 101 (2000).

[74] H. G. Boyen, G. Kastle, F. Weigl, B. Koslowski, C. Dietrich, P. Ziemann, J. P. Spatz, S. Riethmuller, C. Hartmann, M. Moller, G. Garnier, P. Oellhafen, Science **297**, 1533 (2002).

[75] S. K. Shaikhutdinov, R. Meyer, M. Naschitzki, M. Bäumer, H. –J. Freund, Catal Lett. **86**, 211 (2003).

[76] M. Haruta, N. Yamada, T. Kobayashi, S. Ijima , J. Catal. 115, **301**-309 (1989); J. J. Pietron, R. M. Stroud, D. R. Rolison, Nano Lett. **2**, 545-549 (2002), G. Mills, M. S. Gordon, H. Metiu, J. Chem. Phys. **118**, 4198-4205 (2003).

[77] M. S. Chen and D. W. Goodman, Acc. Chem. Res. **39**, 739-746 (2006).

[78] G. Huttmann and R. Birngruber, IEEE J. Sel. Top. Quantum **5**, 954-962 (1999).

[79] Z. Ge, Y. Kang, T. A. Taton, P. V. Braun and D. G. Cahill, Nano Lett. **5**, 531-535 (2005).

[80] C. Loo, A. Lowery, N. Halas, J. West, R. Drezek, Nano Lett. **5**, 709-711 (2005); I. H. El-Sayed, X. Huang, M. A. El-Sayed, Cancer Lett. **239**, 129-135 (2006).

[81] P. Pyykkö, Angew. Chem. Int. Ed. **43**, 4412-4456 (2004).

[82] M. P. Johansson, D. Sundholm and J. Vaara, Angew. Chem. Int. Ed. **43**, 2678-2681 (2004).

[83] Y. Gao and X. C. Zeng, J. Am. Chem. Soc. **127**, 3698-3699 (2005).

[84] H. Häkkinen, R. N. Barnett and U. Landman, Phys. Rev. Lett. **82**, 3264-3267 (1999); I. L. Garzón, C. Rovira, K. Michaelian, M. R. Beltrán, P. Ordejón, J. Junquera, D. Sánchez-Portal, E. Artacho and J. M. Soler, Phys. Rev. Lett. **85**, 5250-5251 (2000).

[85] J. A. Larsson, M. Nolan and J. C. Greer, J. Phy. Chem. B **106**, 5931-5937 (2002).

[86] J. Wang, J. Jellinek, J. Zhao, Z. Chen, R. B. King, P. von Ragué Schleyer, J. Phy. Chem. A **109**, 9265-9269 (2005).

[87] J. Wang, G. Wang and J. Zhao, Phys. Rev. B **66**, 035418 (2002).

[88] X. Yang and J. Dong, Phys. Rev. B **71**, 233403 (2005).

[89] P. Z. Coura, S. B. Legoas, A. S. Moreira, F. Sato, V. Rodrigues, S. O. Dantas, D. Ugarte and D. S. Galvão, Nano Lett. **4**, 1187-1191 (2004).

[90] E. Z. da Silva, F. D. Novaes, A. J. R. da Silva and Fazzio, Phys. Rev. B **69,** 115411 (2004).

[91] R. T. Senger, S. Dag and S. Ciraci, Phys. Rev Lett. **93**, 196807 (2004).

[92] F. Ercolessi, W. Andreoni and E. Tosatti, Phys. Rev Lett. **66**, 911-914 (1991).

[93] F. Ercolessi, M. Parrinello and E. Tosatti, Philos. Mag. A **58**, 213 (1988).

[94] L. J. Lewis, P. Jensen and J. –L. Barrat, Phys. Rev. B **56**, 2248-2257 (1997).

[95] C. L. Cleveland, W. D. Luedtke and U. Landman, Phys. Rev. Lett. **81**, 2036-2039 (1998);

C. L. Cleveland, W. D. Luedtke and U. Landman, Phys. Rev. B **60**, 5065-5077 (1999).

[96] H. B.Liu, J. A. Ascencio, M. Perez-Alvarez and M. J. Yacaman, Surf.Sci. **491**, 88-98 (2001).

[97] Y. Wang, S. Teitel and C. Dellago, Chem. Phys. Lett. **394** 257-261 (2004); Y. Wang, S. Teitel and C. Dellago, J. Chem. Phys. **122** 214722 (2005).

[98] J. –H. Shim, S. –C. Lee, B. –J. Lee, J. –Y. Suh and Y. W. Cho, J. Crystal Growth **250**, 558-564 (2003).

[99] H. –S. Nam, N. M. Hwang, B. D. Yu and J. –K. Yoon, Phys. Rev. Lett. **89**, 275502 (2002).

[100] G.. Bilabegović, Phys. Rev. B **58**, 15412-15415 (1998); G.. Bilabegović, Comp. Mater. Sci. **18**, 333-338 (2000); G.. Bilabegović, Solid State Comm. **115** 73-76 (2000).

[101] B. Wang, S. Yin, G.. Wang, A. Buldum and J. Zhao, Phys. Rev. Lett., **86**, 2046 (2001).

[102] L. Hui, F. Pederiva, G. H. Wang and B. L. Wang, J. Chem. Phys. **119**, 9771-9776 (2003).

[103] J. Diao, K. Gall and M. L. Dunn, Nature Mater. **2**, 656-660 (2003); J. Diao, K. Gall and M. L. Dunn, Phys. Rev. B **70**, 075413 (2004).

[104] J. Wang, X. Chen, G. Wang, B. Wang, W. Lu, J. Zhao, Phys. Rev. B **66**, 085408 (2002).

[105] Y. Wang and C. Dellago, J. Phys. Chem. B **107**, 9214-9219 (2003).

[106] K. Gall, J. Diao and M. L. Dunn, Nano Lett. (2004); J. Diao, K. Gall and M. L. Dunn, Acta Mater. **54** 643-653 (2006); J. –S. Lin, S. P. Ju and W. –J. Lee, Phys. Rev. B **72**, 085448 (2005).

[107] J. Wang, G..Wang and J. Zhao, Phys. Rev. B **66**, 035418 (2002).

[108] H. Häkkinen, B. Yoon , U. Landman, X. Li, H. –J. Zhai, and L. –S. Wang, J. Phys. Chem. A **107**, 6168-6175 (2003).

[109] M. P. Johansson, D. Sundholm and J. Vaara, Angew. Chem. Int. Ed. **43**, 2678-2681 (2004).

[110] J. Wang, J. Jellinek, J. Zhao, Z. Chen, R. B. King and P. von Ragué Schleyer, J. Phys. Chem. A **109**, 9265-9269 (2005).

[111] H. Häkkinen, R. N. Barnett and U. Landman, Phys. Rev. Lett. **82**, 3264-3267 (1999).

# Chapter 2

# Simulation Methods

In this chapter we give an introduction and review of the computational/theoretical methods we used in this thesis to study gold nanoclusters.

## 2.1 Molecular Dynamics

Molecular Dynamics (MD) is a technique for determining the dynamics (ie the positions and velocities as a function of time) of a many body system. In classical MD, the equations of motion for an atom are given by Newton's laws, which are numerically integrated to give velocities and positions. All of the physics of the system is contained in the interatomic potential which is used to generate the forces on the atoms. The time over which the atomic (or molecular) dynamics occurs is typically in the range from femtosecond ($10^{-15}$s) to nanoseconds ($10^{-9}$s) time scale. We give a brief overview of this method below.

### 2.1.1 Equations of motion

For particles interacting via non-impulsive forces (termed 'soft particles'), there is no precise definition of the time of a collision. Therefore we need to solve the equations of motion numerically.

The initial positions of particles $\mathbf{r}_1, \mathbf{r}_2, \mathbf{r}_3, \ldots \mathbf{r}_N$, and velocities of particles $\mathbf{v}_1, \mathbf{v}_2, \mathbf{v}_3, \ldots \mathbf{v}_N$, of the system are given. At each position $\mathbf{r}_i$, the acceleration of each particle $\mathbf{a}_i$ is known from the intermolecular force function since $\mathbf{a_i} = \mathbf{f_i}$ /m, where m is the mass of the atom. The total force on a particle $\mathbf{f_i}$ is the sum of interaction forces with all other particles (2.1):

$$\mathbf{f}_i = \sum_{j \neq i}^{N} \mathbf{f}_{ij} \quad , \tag{2.1}$$

the self interaction term j = i is avoided. An assumption has been made that the presence of other particles will not perturb the magnitude of the interaction between a pair of particles. This is called the pairwise additive assumption. Investigations on the accuracy of this assumption have been made [1].

A numerical algorithm is applied to solving the coupled differential equations of motion (ie Newton's second law). A popular algorithm proposed by Verlet [2] is as follows (2.2):

$$\begin{aligned} \mathbf{r}(t+\delta t) &= \mathbf{r}(t) + \delta t\, \mathbf{v}(t) + \frac{1}{2}\delta t^2\, \mathbf{a}(t) \\ \mathbf{v}(t+\delta t) &= \mathbf{v}(t) + \frac{1}{2}\delta t\, [\mathbf{a}(t) + \mathbf{a}(t+\delta t)] \end{aligned} \quad , \tag{2.2}$$

The first step determines the new position using information from the last time step. The second step determines the new velocity using the average of accelerations the particle feels before and after the time step. Hence the trajectories of the particles can be determined by choosing an appropriate time step interval.

### 2.1.2 Thermostat and velocity scaling

All our MD simulations were done in either the NVT or NVE ensemble. For NVT, the temperature of the system is required to be a constant, which is externally set. A thermostat algorithm is implemented in order to keep the temperature of a system at a constant value. The constant temperature is achieved by use of simple ad-hoc scaling of velocities by the method of Woodcock [3]. Adjustment of particle velocities is applied at every time step. The scaled velocity of particle *i* at t+Δt is given by

$$\mathbf{v}(t+\delta t) = \sqrt{\frac{T_{Ext}}{T(t)}}\mathbf{v}(t) \qquad (2.3)$$

where $T_{Ext}$ is the externally set temperature and T(t) is the calculated kinetic temperature at time t. This ensures that the temperature of the system remains at $T_{Ext}$.

## 2.2 Interatomic Potentials for simulating gold nanostructures

The choice of interatomic potential used to simulate the system is critical for accurate MD simulations, as it is this potential that determines all the interatomic interactions and therefore the physics of the system.

### 2.2.1 Embedded Atom Method (EAM) and Modified Embedded Atom Method (MEAM)

The most widely used potential model for metal systems is the Embedded Atom Method (EAM) [4]. This potential gives a good description of bulk metal systems but not necessarily of the surface properties.

The total energy is given by

$$E_{tot} = \sum_i F_i(\rho_h, i) + \frac{1}{2}\sum_{\substack{i,j \\ i \neq j}} \phi_{ij}(R_{ij}), \qquad (2.4)$$

where $\Phi_{ij}$ is the pair potential and $F_i$ is embedding term which models electronic interaction between gold atoms.

The Modified Embedded Atom Method (MEAM) [5] is based on original EAM framework, with inclusion of directional term to mimic the orbital interaction between metal atoms. In principle, MEAM has better description of metal systems but unfortunately, for gold, it cannot predict the bulk (100) semihexagonal reconstruction, which is a well-known phenomenon from experiments [6].

### 2.2.2 Glue potential

In order to describe the surface properties correctly in a molecular dynamics simulation, Ercolessi et al. developed a potential based on the EAM framework, with parameters obtained from gold surface experiments. This potential was named the "glue" potential. This potential is able to predict the (100) semihexagonal reconstruction of the gold surface [6] and other surface properties, and gives a reasonable description of bulk properties [7].

### 2.2.3 Force-Matching potential

A new interatomic potential for gold has also been developed by our group very recently [8]. This new potential was fitted using an improved force-matching methodology, which includes high-temperature solid lattice constants and liquid densities.

### 2.2.4 Performance of Glue and Force-matching potential

To justify the use of Glue and Force-Matching potential in this project, we consider a collection of bulk and surface properties of gold predicted by these two potentials, which has been compared to the experimental results [8]. Generally, Force-matching potential gives good overall agreement to a range of bulk properties including experimental lattice cohesive energy, lattice constant versus temperature, elastic constants, stacking fault energy, radial distribution function and fcc/hcp/bcc lattice energy differences. Compared to Force-Matching potential Glue potential gives reasonable bulk properties however, the elastic constant predicted by Glue potential is in significant disagreement with the experimental value.

For surface properties, Glue potential performs generally better than Force-Matching potential does. The surface energies predicted by Glue potential are in

relatively good agreement with the experimental data. Also, the Glue potential can correctly predict both (1x2) missing row reconstruction on (110) surface and (100) semihexagonal reconstruction, while the Force-matching potential can only predict the reconstruction on (110) surface. On the other hand, the melting temperature is reproduced correctly by Glue potential, but the Force-matching potential predicts a lower melting temperature.

Compared to these two potentials, the traditional EAM potentials (Johnson's and Foiles, Baskes and Daw (FBD)) give poor description of gold surface. In overall, both bulk and surface properties are reasonably reproduced by Force-Matching potential. In contrast, Glue potential gives very good agreement with the experimental data of gold surface and fair agreement with the experimental data of bulk.

Due to different percentages of surface and core atoms, the suitability of an interatomic potential may vary with the nanoparticles of different sizes and shapes. In this study, we will compare the crystallization process of gold nanoparticles of different sizes modeled by the glue and the force-matching potential.

## 2.3 Generation of initial gold nanostructures of different sizes

In this project, initial particles of icosahedral morphology of different sizes were generated from a C program written by Wang [9]. This program generates a Mackay icosahedron structure with a designated number of layers. We used this program to generate ideal icosahedral morphologies of gold clusters ranging in size from 923 – 10179 atoms. Before the start of an MD simulation, the bond length in the gold nanoclusters was scaled to the bulk Au-Au distance, and then a trial MD simulation was performed at 5 K to examine the stability of the gold nanoclusters.

## 2.4 Structural analysis

### 2.4.1 Radial distribution function

The Radical Distribution Function (RDF), g(r), is a measure of the structure of an atomic system. It is the probability of finding another atom at distance r away from a given central atom compared to the averaged density:

$$g(r) = \frac{\rho(r)}{\rho} \quad , \tag{2.5}$$

where ρ(r) is the density at r away from the central atom and ρ is the average density of the system. Figure 2.1 illustrates this.

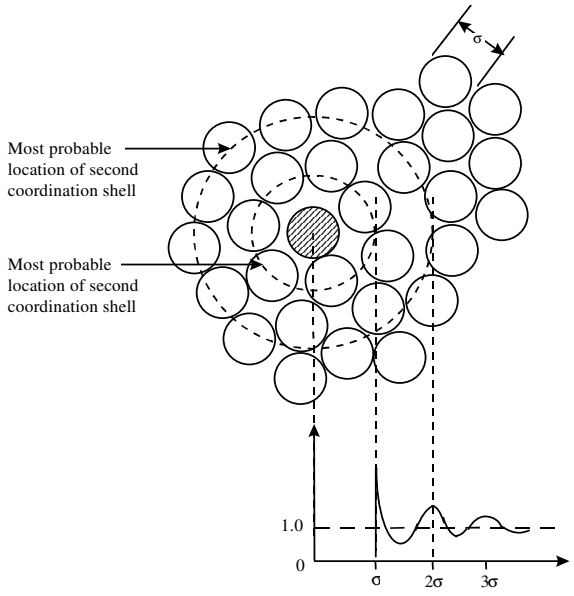


**Figure 2.1** Graphical representation of radial distribution function.

The RDF is the Fourier transform of the static structure factor, S(q), which can be measured in scattering experiments. In experimental studies of crystallization, the behaviour of peaks in the S(q) are used to characterize the crystal nucleation and

growth. As the positions of all atoms in the system are known, more detailed information can be obtained to investigate the structural properties of our system. Therefore MD simulation of crystallization can provide information at the early stage of crystallization, which is too early to be observed experimentally and also be used to measure structural properties which are not accessible to experiment [10]. In MD simulations, g(r) is normally calculated as a discrete function by storing the positions of atoms at definite intervals ($\Delta r$). Then a histogram is constructed between r and r + $\Delta r$ and this discrete function will tend to the true value of g(r) when $\Delta r \rightarrow 0$.

Structure measures such as the RDF and bond-angle distribution function (BADF) can only provide a spatial average of the local environment of individual atoms. It is desirable to develop a method to measure the local order around an atom that can distinguish between particles in a liquid-like environment and a crystalline environment [10]. The structure measure method described in the following sections allows us to do this.

### 2.4.2 Planar graph ring sequences

A quantitative analysis of ordering in the core of a cluster can be obtained by describing the local environment of each atom using a classification scheme based on planar graphs [10]. This method is topological in nature and is a development of the reduced graph method of Bernal [11]. The local structure around each atom is defined in terms of the bonds between the nearest neighbours of the central atom. Specifically the planar graph formed by the nearest neighbours and the bonds between them is used to characterise this connectivity [10].

A planar graph is a set of vertices (atoms) joined by lines (bonds between neighbours) such that no two lines cross one another. In this method, two atoms are regarded as being bonded if their distance is less than or equal to the first minimum

of the radial distribution function. Hence bonds are defined geometrically rather than chemically [10]. At the simplest level the number of rings of various sizes making up the planar graph can be used to characterize it. A more complete description also characterizes the arrangement of rings about each vertex (nearest neighbour). This is done in this work in order to categorically identify crystalline or well-ordered local environments [10].

As an example, Figure 2.2 represents the local environment surrounding a central atom (which is not shown) in a face-centred cubic lattice; the corresponding planar graph is shown on the right. The planar graph represents disorder through the addition or removal of links or atoms (vertices) relative to the ordered graphs, which represent for example stacking faults or dislocations (see Figure 2.3 and caption).

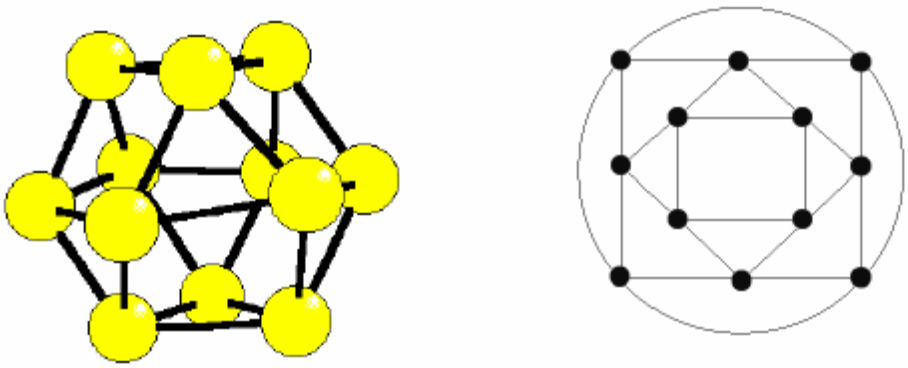

**Figure 2.2** The local environment about an atom in a face-centred cubic lattice (LEFT) and the planar graph indicating the network of bonds between the twelve neighbours of the central particle (which is not shown) (RIGHT).

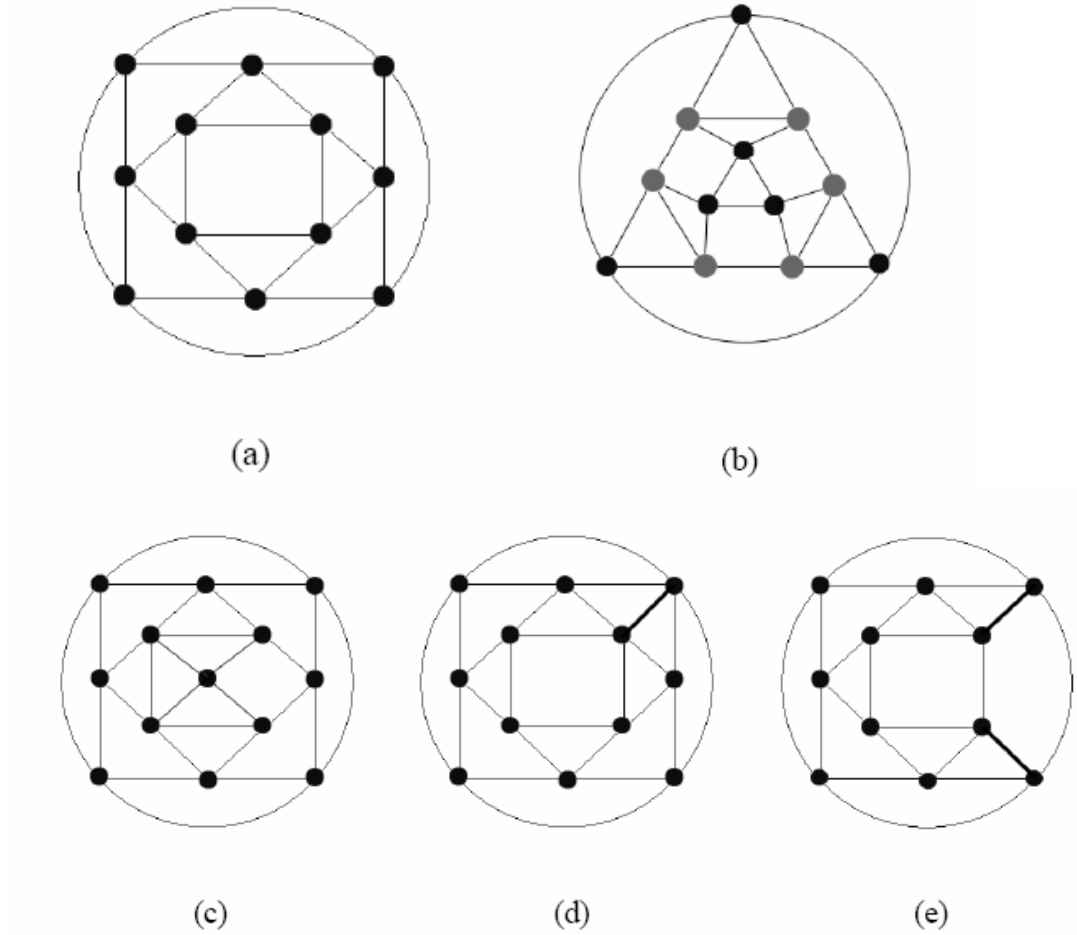


**Figure 2.3** (a) The planar graph of particles in a face-centred cubic arrangement (b) The planar graph of atoms in a hexagonal close packed arrangement (c) Planar graphs of atoms in perturbed face centred cubic arrangements: face-centred + extra nearest neighbour and minus a related bond (d) face-centred with a single extra bond between neighbours and (e) face-centred less one neighbour and plus two related additional bonds.

### 2.4.3 Shortest-path (SP) ring analysis

Another measure of structure is given by ring statistics, in this project, the SP ring structure criterion due to Franzblau [12] is used, which defines that a ring as the SP ring if the number of bonds passed through in moving from one atom of the ring to another is equal to the shortest path, considering all possible paths through the network of bonds from one atom to another. The 'distance' between two atoms is

defined as: the minimum number of bonds that would have to be traversed in order to move from one atom to another. The 'distance' which is not the physical bond length is; 1 for nearest neighbours, 2 for next nearest neighbours and so on. Using the SP ring criterion the simplest quantities obtainable from ring analysis are the ring statistics, that is, the prevalence of the ring types observed. The term 'ring size' refers to the number of atoms in the ring and not the physical dimension [12]. The SP ring structures evaluated here range in *'ring size*' from 3 to 6.

In an SP ring antipodal pairs are pairs of atoms of a ring that are 'opposite' each other (Figure 2.4)**.** For odd numbered rings there are two such antipodal pairs for each atoms of the ring (Figure 2.5). Thus there are three antipodal pairs in a shortest path six-membered ring and the 'distance' between these antipodal pairs is three.

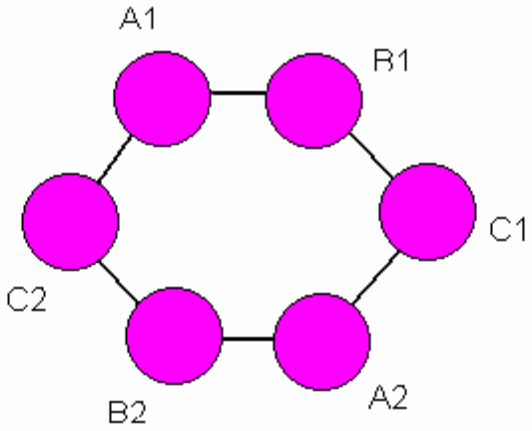


**Figure 2.4** An SP six-membered ring containing three antipodal pairs.
Particles A1 and A2 are antipodal pairs, as are B1 and B2 and C1 and C2.
The shortest path distance between A1 and A2 is through the particles B1 and C1, involving three bonds.

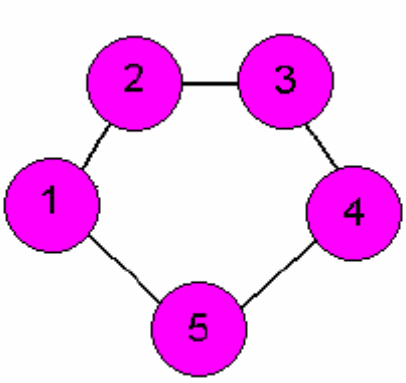


**Figure 2.5** An SP five-membered ring containing six antipodal pairs. The antipodal pairs are (1,3), (1,4), (2,4), (2,5), (3,5) and (3,1). The shortest path distance between 1 and 3 is through the particle 2 and involves two bonds 1-2 and 2-3.

The simplest case, the 3-membered ring occurs the most often, for instance, in the (111) face of the FCC lattice as shown in Figure 2.6(a) or in the close packed two-dimensional networks of an adsorbed monolayer. The (100) ring is associated with a 4-membered ring as shown in Figure 2.6 (b).

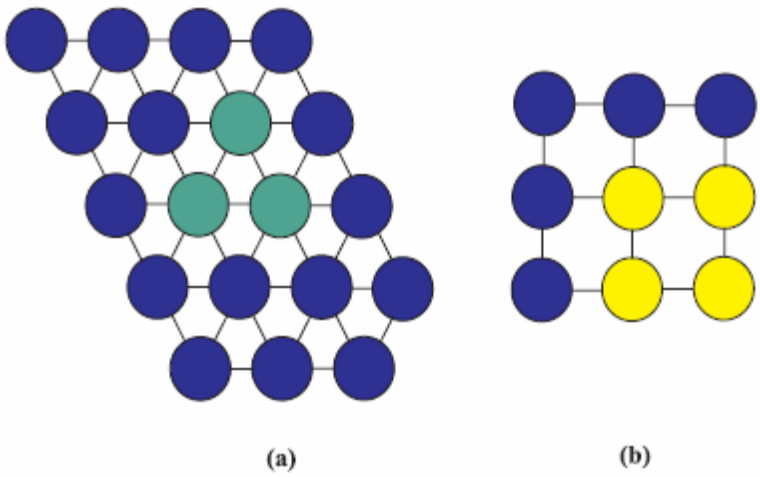


**Figure 2.6 (a)** The (111) plane and associated 3-membered rings and **(b)** the (100) plane and associated 4-membered rings.

The criteria for the 4-membered and 5-membered shortest path ring structures are represented schematically in Figure 2.7. In addition to its simple SP ring definition a modified 6-membered SP ring type was used here which was given by the following criteria [13]:

1. Every atoms of the 6-membered ring is bonded to the same one and only one central atoms.

2. The distance between antipodal pairs is 2 obtained by traversing a path through the central atom.

3. For antipodal pairs there are no other paths between two atoms that have a distance of 2. That is, only one nearest neighbour is shared between the two atoms and this is the central atom.

4. The six outer particles of the ring have the same shortest path relations as for the normal shortest path, if the central particle is ignored.

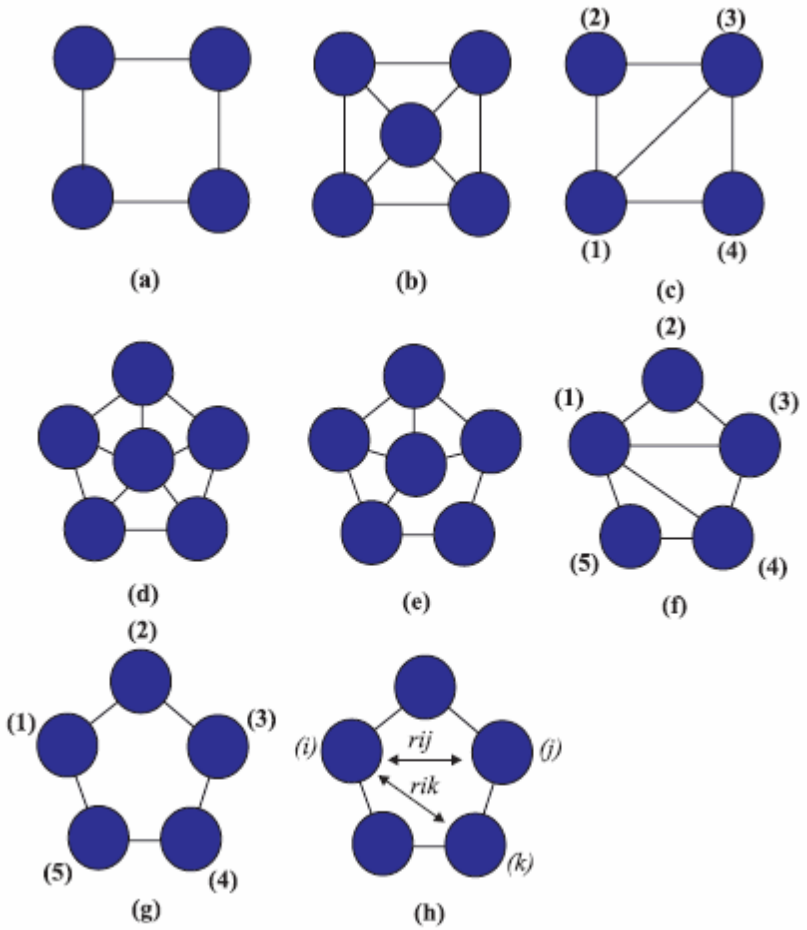


**Figure 2.7** Characterisation of the 4 and 5-membered SP rings: **(a)** and **(b)** are 4-membered SP rings whilst **(c)** is not, due the path **(1-3)**, **(d)** and **(e)** are 5-membered SP rings whilst **(f)** is not since the single 'bonds' between **(1-3)** or **(1-4)** provide a 'shorter' path than either **(1)-(2)-(3)** or **(1)-(5)-(4)**, respectively, **(g)** the six antipodal pairs of the 5-membered ring **(1,3),(1,4),(2,4),(2,5),(3,5),(3,1)**. The SP 'distance' between **(1)** and **(3)** through atom **(2)** traverses the two bonds **(1-2)** and **(2-3)** and **(h)** the distances $r_{ij}$ and $r_{ik}$ which contribute to the 5-membered ring component of the $g(r)$.

The motivation for the modified 6-membered ring type [13] was the characterization of a three-dimensional closed packed hard sphere crystalline structure [10], however, it also represents structural features common to adsorbed films [13]. Now we use this to characterize the internal structures of nanoclusters. Figure 2.8 represents the modified 6-membered rings.

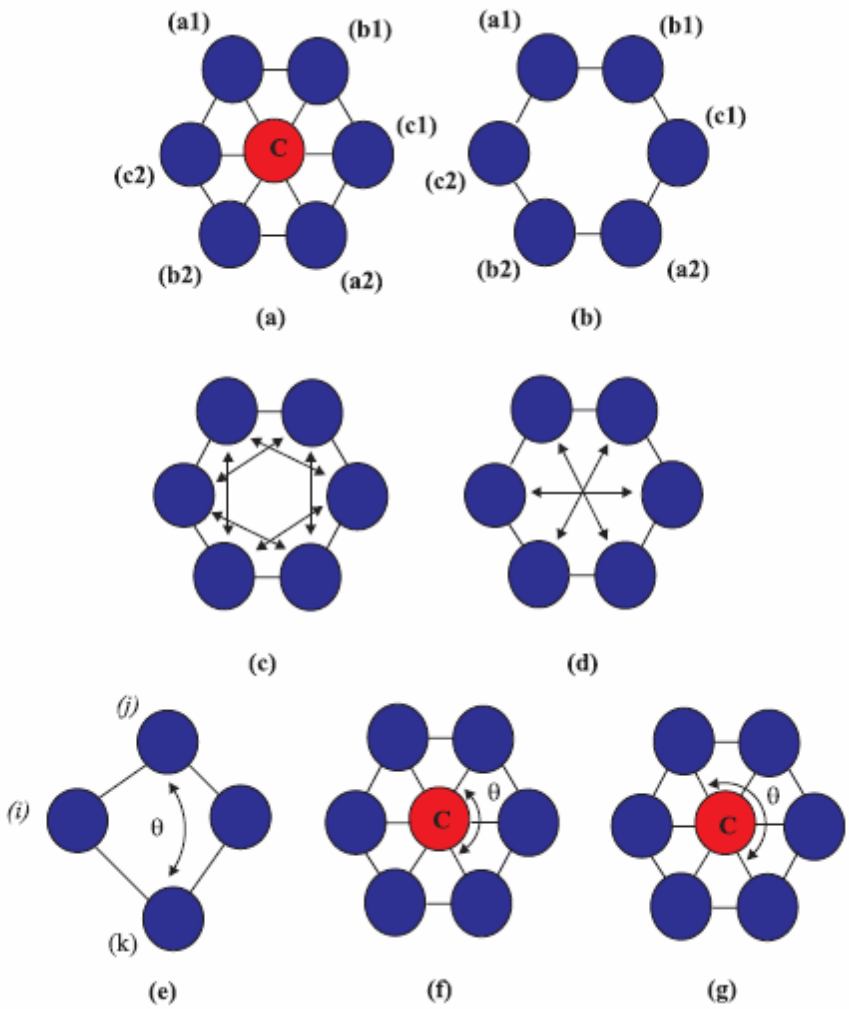


**Figure 2.8** Characterisation of the 6-membered SP rings: **(a)** the modified 6-membered ring where '**C**' is the central atom, **(b)** an SP 6-membered ring containing three antipodal pairs **(a1,a2),(b1,b2),(c1,c2)** the 'shortest' paths of equal 'distance' between **(a1)** and **(a2)** are through **(b1)** and **(c1)** or through **(c2)** and **(b2)**. Pairs of atoms in the 6-membered SP ring which contribute to the 'split' second-peak of the g(r) **(c)** the Type A component and **(d)** the Type B component. **(e)** The bond angle formed between the triplet of atoms *(i,j,k)*. This is calculated for all 'size' SP rings and contributes to the Type 1 of the 6-membered SP ring bond angle distribution. **(f)** The criterion for the Type 2 modified 6-membered ring bond angle distribution. **(g)** The criterion for the Type 3 modified 6-membered ring bond angle distribution.

### 2.4.4 Geometrical analysis of ring structure

In computer simulation the information contained in the g(r) is too averaged to provide the more detailed information that we would like to know and also does not sufficiently exploit the available data. Obviously it is of particular benefit if the structural measures that are developed can be related back to the pair correlation function [10]. Another commonly used measure of the structure of a system is the distribution of bond angles formed by triplets of neighbours [10]. This can be viewed as a reduced three-body distribution function and hence provides qualitatively different information than g(r).

In order to extract further useful information from these two distribution functions they are decomposed into contributions from different shortest path rings that are formed by the bonds between nearest neighbours in the system [10, 12]. By doing this it is hoped that more quantitative details about the changes in morphology occur during melting and crystallization can be obtained.

#### 2.4.4.1 Decomposition of radial distribution function

In a typical calculation of the radial distribution function of an atomic system one loops over every pair of atoms in the system, summing the number of pairs of atoms separated by distances between r and r+dr. In the ring analysis program this procedure is modified [10]. During the ring analysis for every ring found, a list is stored of all antipodal pairs of atoms that are part of the same ring. In calculating the radial distribution function for the atomic system one first performs a loop over all pairs of atoms found in this way starting from the smallest rings. Individual distributions are stored for each ring size. The remaining contributions to g(r) of pairs of atoms, which are not both part of the same ring, are then calculated.

The spatial averaging used in accumulating the radial pair distribution function $g(r)$ results in the loss of information relating to the angular distribution of atom about

any particular atom and the separation distance between any particular pair of atoms [13]. However, by decomposing $g(r)$ using the unique association of contributing pairs with the SP ring structure types, the information on the pair separation distance can be regained [12]. The so-called SP ring decomposition of the total $g(r)$ given by

$$g(r) = g_3(r) + g_4(r) + g_5(r) + g_6(r)A + g_6(r)B + g_{rem}(r), \qquad (2.6)$$

where $g_{rem}(r)$ represents the uncounted or remaining ring types, for example, mixed types or ring sizes larger than 6. The labels for the *typeA* and *typeB* $g_6(r)$, represent the contributions to the standard SP 6-membered rings from pairs separated by 2 bonds and 3 bonds (the antipodal pairs), respectively, these are depicted in Figure 2.8. We use an example of hard sphere system [10] to demonstrate the decomposition of radial distribution function. Figure 2.9 shows the decomposition of the radial distribution function into contributions from various sized rings for a hard sphere crystal at a reduced density of 1.05. In figure 2.10, we compare the g(r) with sum of ring contributions for a hard sphere crystal at a reduced density of 1.05. The distribution is resolved into contribution from different rings beyond r = 2.48.

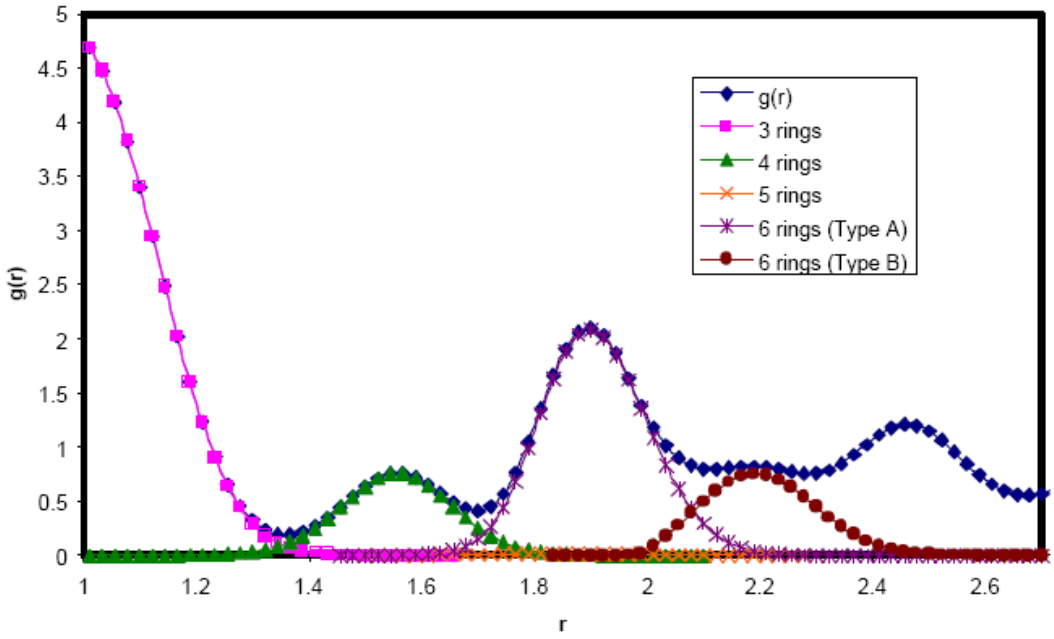


**Figure 2.9** Decomposition of the radial distribution function into contributions from various sized rings for a hard sphere crystal at a reduced density of 1.05 (B. O'Malley, Ph.D. thesis (RMIT) (2001)).

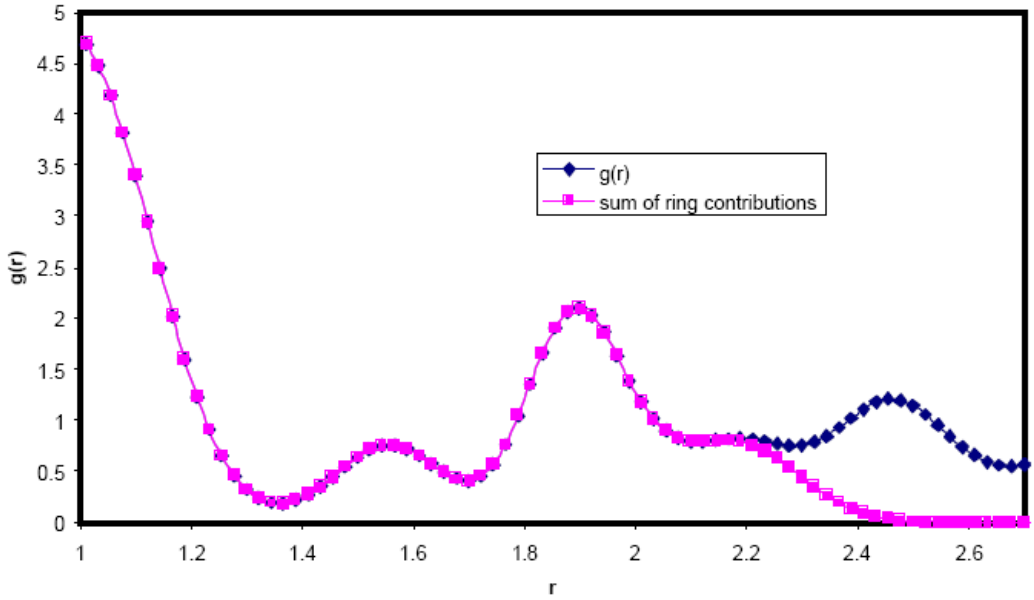


**Figure 2.10** Comparison of g(r) with sum of ring contributions for a hard sphere crystal at a reduced density of 1.05 (B. O'Malley, Ph.D. thesis (RMIT) (2001)).

### 2.4.4.2 Bond angle distribution

The distribution of bond angles formed by adjacent triplets of atoms in a ring can also be calculated (Figure 2.11), and hence the total bond angle distribution for an atomic structure can be decomposed into contributions from rings of various sizes [10], which is shown in Figure 2.12. The bond angle distribution quantifies the short to medium range orientational order in the atomic system.

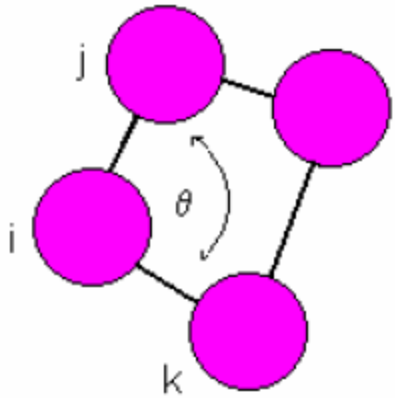


**Figure 2.11** Bond Angle formed by the triplet of particles (i,j,k).

The bond angle $\theta$ within the standard SP rings was defined as the angle formed between the $i^{th}$ atom and two of its neighbours labelled $j$ and $k$ forming a triplet of atoms (Figure 2.11). It is possible that triplets of atoms may be part of more than one ring. In cases where it is desired that the ring contributions be properly normalised a simple rule can be applied to avoid double counting [10]. Bond angles are counted in an ascending hierarchy of ring size, and any repeating triplets in larger rings are ignored. By the definition of shortest path rings there is no overlap between 3 and 4 membered rings.

The bond angle distribution for the six-membered rings is split into three components due to its modified definition [10], namely:

• 6 type 1 where the triplet was part of the standard SP ring and ignores the central atom.

• 6 type 2 which records the bond angle formed by the central atom and the 6 separate pairs of atoms in the ring separated by a shortest path of 2.

• 6 type 3 which records the bond angles formed between the central atom and the 3 antipodal pairs in the ring. To avoid double counting the contributions of type 1 are evaluated before type 2. The 3 modified 6-membered SP ring bond types are depicted in Figure 2.8.

Here, we also use an example of hard sphere system [10] to demonstrate the decomposition of bond angle distribution. The distribution of bond angles for rings of various sizes is shown in Figure 2.12**.** Nearly all bond angles formed between triplets of bonded particles are resolved into contributions from different rings. This is shown in Figure 2.13 where the sum of the ring contributions is compared to the total bond angle distribution.

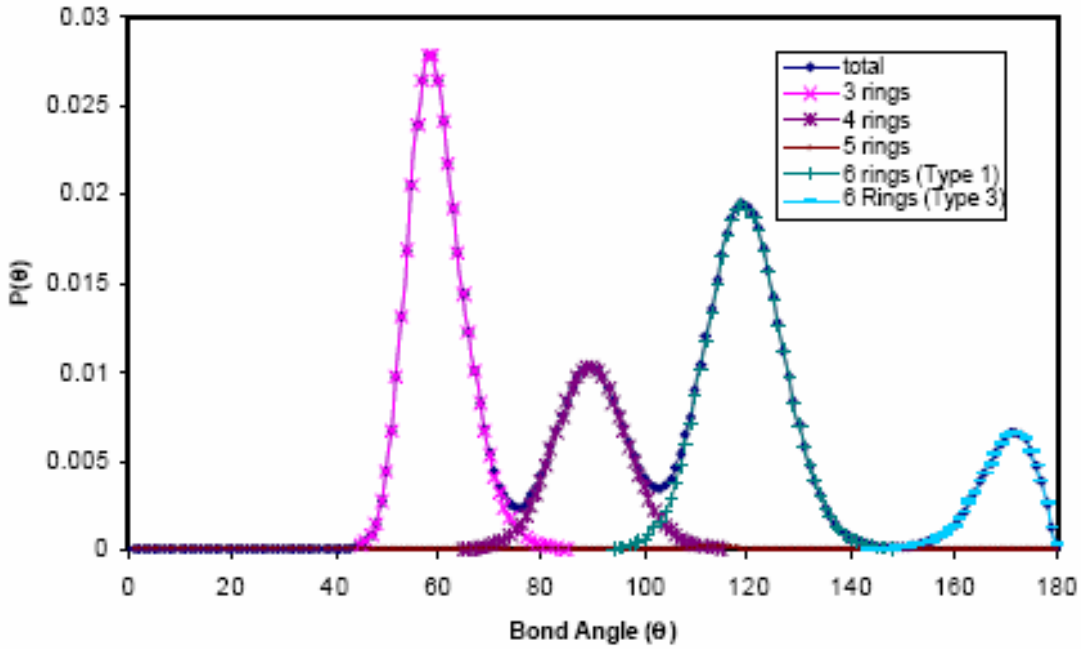


**Figure 2.12** The distribution of bond angles for rings of various sizes for a hard sphere crystal at a reduced density of 1.05 (B. O'Malley, Ph.D. thesis (RMIT) (2001)).

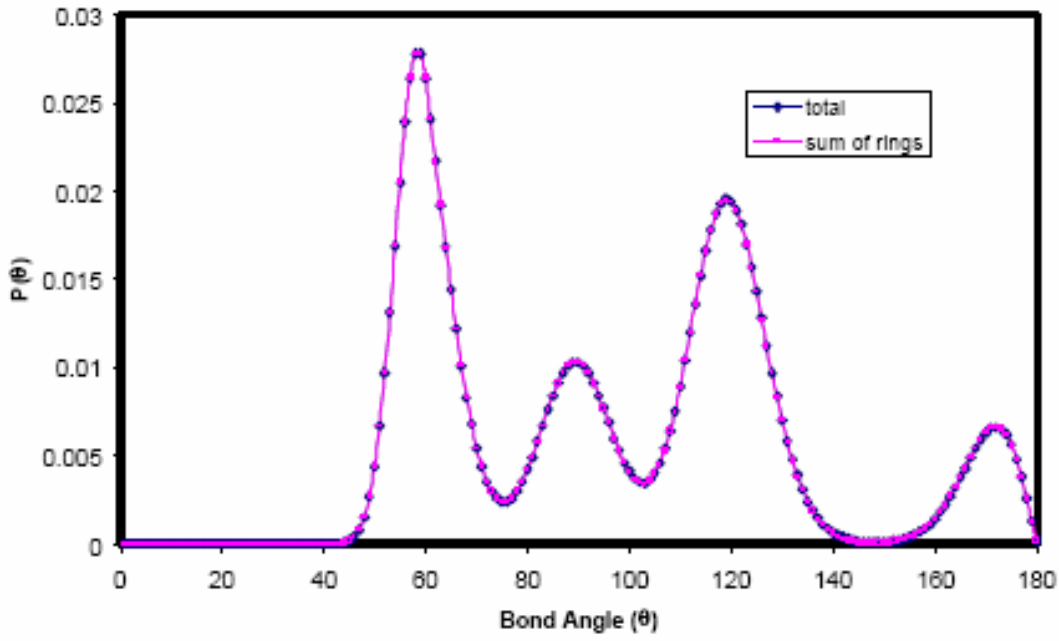


**Figure 2.13** Comparison of total bond angle distribution and sum of ring contributions for a hard sphere crystal at a reduced density of 1.05 (B. O'Malley, Ph.D. thesis (RMIT) (2001)).

### 2.4.5 Spherical harmonic order parameter

A geometric measure of the orientational order of an atomic system is the spherical harmonic bond order parameter. A set of spherical harmonics is associated with each geometric bond, **r**, joining an atom to one of its neighbours [14] (Equation 2.7):

$$Q_{lm}(r) = Y_{lm}(\theta(r), \phi(r)) \quad , \tag{2.7}$$

where $Y_{lm}(\theta(r), \phi(r))$, are spherical harmonics and $\theta(r)$ and $\phi(r)$ are the polar angles of the bond measured relative to a reference coordinate system, typically that defined by the simulation cell. The overall orientational order is determined by taking appropriate averages over all bonds in the system (Equation 2.8):

$$\bar{Q}_{lm} = \frac{1}{N_b} \sum Q_{lm}(r) \quad . \tag{2.8}$$

where $N_b$ is the number of bonds.

As both $\theta$ and $\phi$ depend on the reference coordinate system used, rotationally invariant combinations of the $\bar{Q}_{lm}$ are often defined, such as

$$Q_l = \left( \frac{4\pi}{2l+1} \sum_{m=-1}^{l} | \bar{Q}_{lm} | \right)^{1/2} \quad . \tag{2.9}$$

If both orientations of a bond between two atoms are counted in the above average then the odd harmonics will vanish and hence attention is usually focused on the even $l$ spherical harmonics, as these are invariant under inversion.

Steinhardt et al [15] originally introduced the even $l$ spherical harmonics in order to study orientational order in liquids and glasses. They have also been used by a number of authors to provide an order parameter for a crystallizing system. In such studies $l = 6$ spherical harmonic $Q_6$ is often used to monitor the evolution of crystalline order. This

order parameter is large for a number of different crystalline and icosahedral structures, and hence gives an overall measure of the crystallinity of the system that is insensitive to the actual underlying crystal lattice. Although the above spherical harmonics are in principle zero for an isotropic system they can locally be large and hence if the above average is taken over the bonds between an atom i and its $N_b(i)$ neighbours they can be used to characterize local orientational order by defining a set of invariants for each atom (Equation 2.10 and 2.11):

$$\bar{q}_{lm}(i) = \frac{1}{N_b(i)} \sum_{j=1}^{N_b(i)} Y_{lm}(\hat{r}_{ij}) \qquad (2.10)$$

and

$$q_l(i) = \left( \frac{4\pi}{2l+1} \sum_{m=-1}^{l} | q_{lm}(i) |^2 \right)^{3/2}, \qquad (2.11)$$

In a liquid the even *l* spherical harmonics are zero when averaged over all bonds in the system, as the spherical harmonics of neighbouring atoms are not in phase and hence do not add up coherently, as they do in a crystal. This has led van Duijneveldt et al [16] to suggest a local measure of the crystallinity or solid-like nature of the environment of an atom in terms of the coherence of the spherical harmonics of an atom with that of its neighbours. They define for each atom a normalized 2l + 1 vector (l = 6) as equation 2.12:

$$\tilde{Q}_{6m}(i) = \frac{\bar{q}_{6m}(i)}{\left( \sum_{m=-6}^{6} | q_{6m}(i) |^2 \right)^{1/2}} \qquad (2.12)$$

and

$$q_6(i) \cdot q_6(j) = \sum_{m=-6}^{6} \tilde{q}_{6m}(i) \tilde{q}_{6m}(j)^* \quad , \qquad (2.13)$$

with $$q_6(i) \cdot q_6(i) = 1 \quad . \qquad (2.14)$$

The dot product (Equations 2.13 and 2.14) is then taken between each atom and its neighbours. If this dot product is greater than some preset value (0.5 in their work) the two atoms are regarded as being connected (their spherical harmonics are in phase). A particle is regarded as being solid- like if it has at least 7 such connections with its neighbours.

## 2.5 Velocity autocorrelation function (VACF), vibrational entropy and total free energy calculations

Frozen phonon calculations assuming the harmonic approximation is a common method of determining the vibrational modes of solid. Alternatively one can calculate the vibrational density of states (VDOS) of gold nanoclusters by taking the Fourier transform of velocity autocorrelation function (VACF), where the VACF is defined as

$$Z(t) = \sum_{\tau}^{\tau_m} \frac{< v_n(t+\tau) \cdot v_n(\tau) >}{< v_n(\tau) \cdot v_n(\tau) >} \quad , \qquad (2.15)$$

where the brackets represents the average over the total number of atoms in the system. We performed Fourier transform of the VACF by using the Filon's method [17], which was developed to approximate the numerical integration of the form (Equation 2.16):

$$F(T) = \int_0^T f(x)\cos pxdx \quad . \qquad (2.16)$$

The vibrational density of state (VDOS) of gold nanoclusters is obtained for different motifs and sizes. The VDOS of metal nanoclusters has been widely investigated theoretically and experimentally [18 -20]. For gold nanoclusters with decahedral structures, the VDOS and its variation in different zones have been analyzed [21].

In considering the stability of the various nanoclusters we estimated the Gibbs free energy of the clusters. If we assume that the vibrational entropy forms the largest contribution to the entropy of the nanocluster then the Gibbs free energy is given by

$$G = U - TS_{vib} + PV, \qquad (2.17)$$

where U is the internal energy, S is the entropy, V is the volume. For a nanocluster at equilibrium in an isolated vacuum environment, the pressure is close to zero and the PV term is negligible.

Within the harmonic approximation (Equation 2.18), the vibrational entropy $S_{vib}(V)$ of a cluster is related to the vibrational density of states *g(V,ω)* by [22].

$$S_{vib}(V) = -\frac{\partial F_{vib}(V)}{\partial T} = 3Nk_b \int_0^\infty \left[ \frac{\eta\omega}{2k_bT} \coth \frac{\eta\omega}{2k_bT} - \ln\left( 2\sinh \frac{\eta\omega}{2k_bT} \right) \right] g(V,\omega) d\omega$$

, (2.18)

where N is equal to number of atoms in a nanoclusters; $k_b$ is equal to the Boltzmann constant with units of eV-$K^{-1}$; T is the absolute temperature with units of K; g(V,ω) is the total vibrational density of states (VDOS) for the structure at volume V, and

gives the number of modes with frequency lying in the interval (ω, ω + *d* ω). The VDOS of the gold nanoclusters is obtained from the Fourier transform of velocity autocorrelation function Z(t) (Equation 2.19) (which is obtained routinely from MD simulations [23],

$$g(\omega) = \int_0^\infty dt \cos(\omega t) Z(t) \quad . \qquad (2.19)$$

We evaluate equation 2.19 using Filon's method (equation 2.16) as mentioned above.

# References


[1] B.M. Axilrod, and E. Teller, J. Chem. Phys., **11**, 299 (1943).

[2] Verlet, L., Phy. Rev., **159**, 98 (1967).

[3] Woodcock, L. V., Chem. Phys. Letts., **10**, 257 (1971).

[4] M. S. Daw and M. I. Baskes, Phys. Rev. B **29**, 6443 (1984);

M. S. Daw and M. I. Baskes, Phys. Rev. Lett. **50**, 1285 (1983).

[5] M. I. Bakes, Phys. Rev. B **46**, 2727 (1998);

B. Lee, M. I. Baskes, H. Kim, and Y. K. Cho, Phys. Rev. B **64**, 184102 (2001).

[6] F. Ercolessi, E. Tosatti and M. Parrinello, Phys. Rev. Lett. **57** 719 (1986).

[7] F. Ercolessi, W. Andreoni and E. Tosatti, Phys. Rev. Lett. **66**, 911 (1991);

F. Ercolessi, M. Parrinello and E. Tosatti, Philos. Mag. A **58**, 213 (1988).

[8] G. Grochola, S. P. Russo and I. K. Snook, J. Chem. Phys. **123**, 204719 (2005).

[9] http://web1.pas.rochester.edu/~wangyt/algorithms/index.html

[10] B. O'Malley, Ph.D. thesis (RMIT) (2001)

(Available at http://mams.rmit.edu.au/6g0wr8cwl4b1.pdf); B. O'Malley and I. Snook, J. Chem. Phys.**123**, 5, 054511 (2005).

[11] J. D. Bernal, Nature **183**, 141 (1959).

[12] D. S. Fransblau, Phys. Rev. B **44,** 4925 (1991).

[13] R. J. Rees, Ph.D. thesis (RMIT) (2004).

[14] Ian N. Sneddon, Special Functions of Mathematical Physics and Chemistry, Oliver and Boyd, Edinburgh and London (New York: Interscience publishers Inc.) (1961); H. Eyring, The late John Walter and G. E. Kimball, Quantum Chemistry, John Wiley and Sons, Inc. (1965).

[15] F. H. Stillinger and T. A. Weber, Phys. Rev. A **25**, 978 (1982).

[16] J. D. van Duijneveldt and D. Frenkel, J. Chem. Phys. **96**, 4655 (1992).

[17] L. N. G.. Filon, Proc. Roy. Soc. Eden. **9**, 38 (1928).

[18] H. Frase, B. Fultz and J. L. Robertson, Phys. Rev. B **57**, 898 (1998).

[19] A. Kara and T. S. Rahman, Phys. Rev. Lett. **81**, 1453 (1998).

[20] A. B. Papandrew, A. F. Yue, B. Fultz, I. Halevy, W. Sturhahn, T. S. Tollner, E. E. Alp and H. K. Mao, Phys. Rev. B **69**, 144301 (2004).

[21] D. X. Sun, X. G. Gong and X. Q. Wang, Phys. Rev. B **63**, 193412 (2001).

[22] PhD Thesis, E. J. Wu, Massachusetts Institute of Technology (2002)
Available at http://burgaz.mit.edu/PUBLICATIONS/theses.php

[23] M.P. Allen and D. Tildesley, Computer Simulation of Liquids, Clarendon Press Oxford (1987).

# Chapter 3

# Structural Characterization of Gold nanostructures quenched from the melt

It has been shown that gold nanoclusters quenched from the melt can exist in a variety of diverse structural forms, including spherical with an internal crystalline (FCC) core [1], icosahedral (ICO) [2], decahedral (DEC) [3] and FCC cubic [4]. Recently, more interesting shapes of gold nanoclusters have been produced, such as rods [5], prisms [6], rings [7], boxes [8] and even "tadpole" shaped particles [9]. A number theoretical and computational studies have discussed the crystallization thermodynamics, kinetics and relative stability of the gold nanoclusters formed by simulated annealing or quenching from the melt [10-14]. For the smaller nanoclusters (< 100 atoms) Garzon et al [10] found that the difference in binding energy per atom between the amorphous and high symmetry structures was less then 0.01 eV/atom. This suggests a rich diversity of structures may be formed by quenching from the melt as particles are free to thermally rearrange themselves relative to their 'local' neighbor particle configurations.

## 3.1 Simulation procedure

In this study we use molecular dynamics (MD) to compare the structure and stability of 923, 1415, 3871 and 10179 atom gold nanoclusters of three different morphologies (i) perfect icosahedrons; (ii) icosahedron-like nanoclusters (also called thermally annealed nanoclusters in this thesis) and (iii) amorphous nanoclusters, both quenched from the melt. All structures were generated by an

icosahedron generation program [8]. Using MD, clusters quenched from the melt were initially heated to 1400 K until liquid-state equilibrium was achieved (~1.5 ns). To obtain the icosahedron-like nanoclusters we quenched to 298 K using 3 different cooling rates (Q1 = $2x10^{-11}$s/K, Q2 = $4x10^{-11}$s/K and Q3 = $6x10^{-11}$s/K) while the amorphous nanoclusters were formed by a one step quench to 298 K. The perfect icosahedral clusters were held at 298 K throughout the MD simulations. Once at 298 K, structures were equilibrated for 1 ns before analyzing their properties. All MD simulations were performed using the EAM 'glue' potential [3, 5-7] with a time step of 5 fs.

## 3.2 Visual examination of nanostructures and radial distribution function analysis

For the structures of gold nanoclusters crystallized from quenching as described above, we present images and radial distribution function (RDF) plots for the different motifs and sizes. Figure 3.1 shows 923 atom gold nanoclusters with different motifs at 298K. For the icosahedral-like gold nanoclusters, we found the atoms dislocated from the ideal positions of icosahedral symmetry. Compared to icosahedral nanoclusters, amorphous nanoclusters have no definite surface structure.

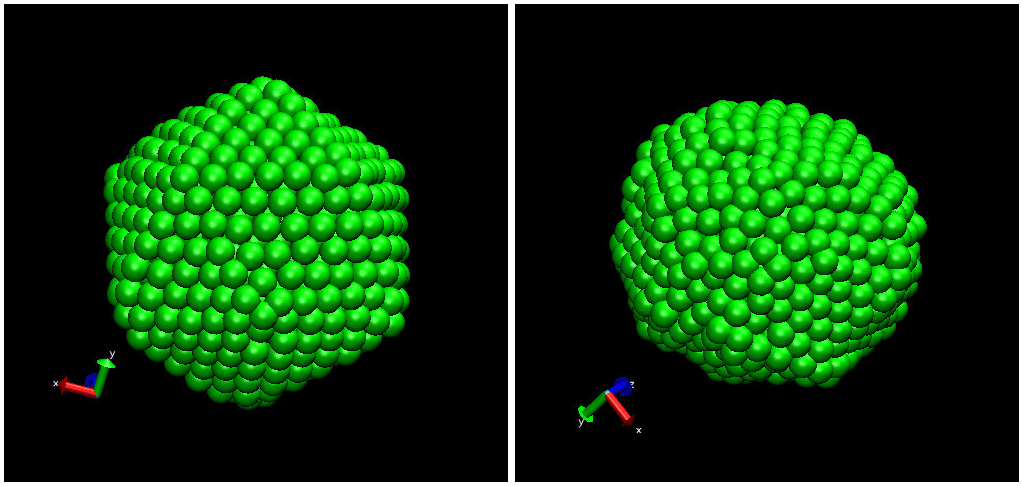

(A) (B)

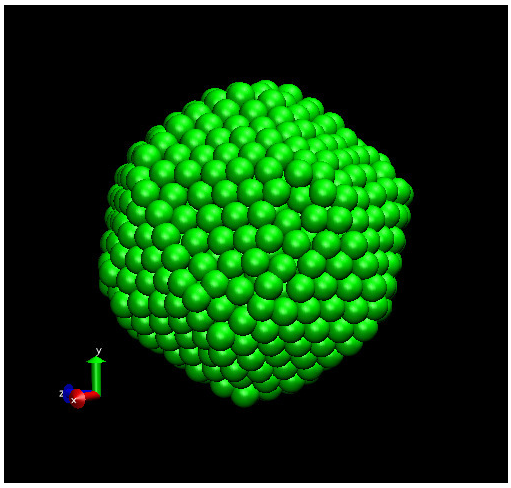

(C)

**Figure 3.1** Images of 923 atoms gold nanoclusters: (a) An icosahedral cluster (b) An amorphous cluster and (c) A thermally annealed (Q1) cluster.

Besides direct observation, the radial distribution function provides information about the internal structure of nanoclusters, which is shown in Figure 3.2. Figure 3.2 shows that the RDF of the icosahedral and thermally annealed nanoclusters are very close, while that of the amorphous structure is distinctly different. The broad but split second peak of the amorphous structure is a typical characteristic of glassy structures [15]. Also, the radial distance of the first peaks of the three motifs increase in the following order: amorphous cluster < thermally annealed cluster < icosahedral cluster. The position of the first peak of the RDF directly reflects the spacing of the internal structure of the particular motif. The average spacing in the amorphous structure is the smallest as the freedom of packing in amorphous structure is the largest among the three motifs. The atoms in the amorphous structure can pack with each other more randomly and as close as possible, in order to maximize the cohesive energy. In an ideal icosahedral cluster, the atoms should attain certain positions within the cluster, due to the high symmetry. Therefore the freedom of packing is much smaller than that of amorphous structure. The thermally annealed nanoclusters are in between these two extremes. The thermal

annealing process allow the atoms in a nanostructure to rearrange themselves in order to maximize the cohesive energy of the whole nanostructure. The atoms in an annealed gold nanocluster are not packed in a very high structural order as the atoms in an icosahedral nnaocluster do. As a result, the atomic spacing in an annealed nanocluster is a little smaller than that in an icosahedral nanocluster.

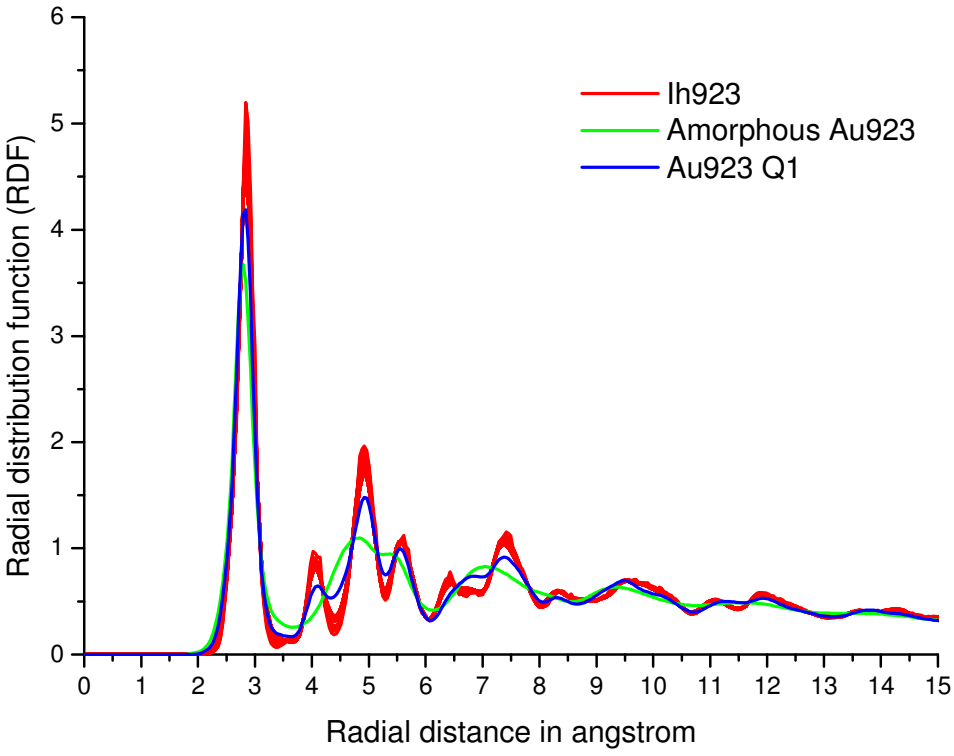


**Figure 3.2** The radial distribution function (RDF) of gold nanoclusters shown in Figure 3.1.

Compared to small gold nanoclusters, the large gold nanoclusters in this study show richer surface reconstructions after thermal annealing. Figure 3.3 shows the images of 10179 atom gold nanoclusters. Again, no definite surface structure can be seen in the amorphous nanocluster. For the thermally annealed nanoclusters, significant surface reconstruction can be seen. The edges and vertices of the nanoclusters are reconstructed, compared to the ideal icosahedral nanocluster. Although large (111)

surface planes are also present in the annealed nanoclusters, steps and defects are also found on the surface.

Interestingly, we discovered that thermally annealed Au10179 nanoparticles exhibit the concave structure reminiscent of the re-entrant angles along <110> edges of the Marks decahedron, in between (111) surface planes. Also, it was found that the lower the quenching rate, the larger the surface concave structure in the nanoparticle is. This type of truncated icosahedron is different from those considered by Rogrígues-Lopez and colleagues [16]. Currently, we are not able to analyze such truncated and rough surface in nanoparticle. Careful investigation should be done for this kind of surface structure in the future.

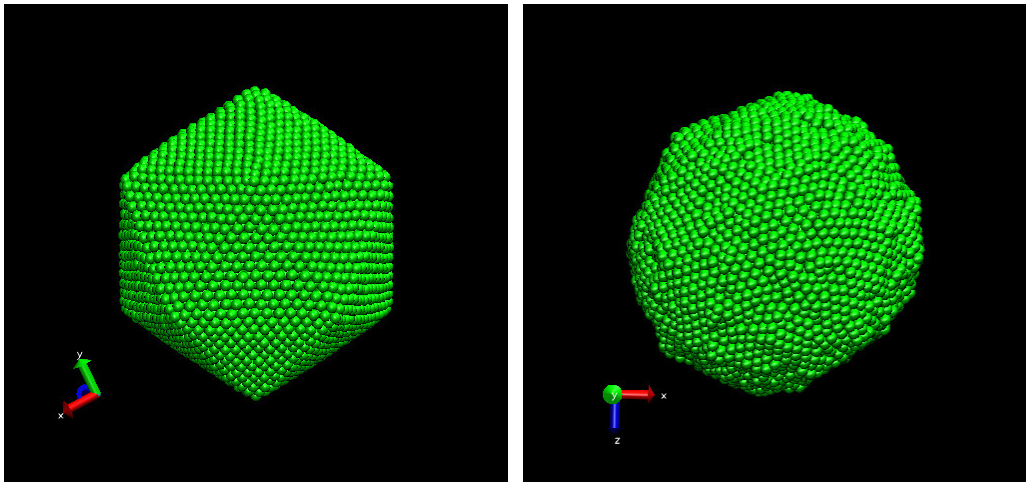

(A) (B)

**Figure 3.3 is continued on the next page.**

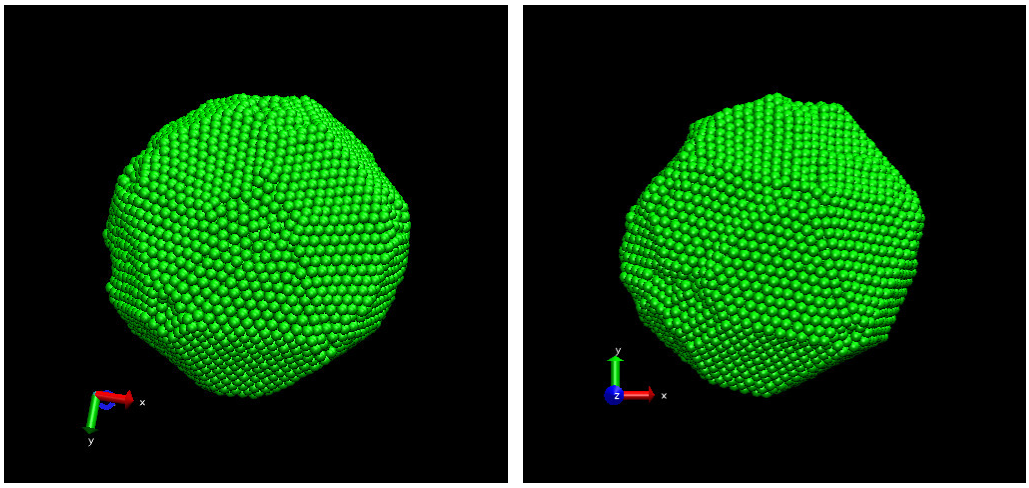

(C) (D)

**Figure 3.3** Images of 10179 atom gold nanoclusters: (a) An icosahedral cluster (b) An amorphous cluster (c) A thermally annealed (Q1) cluster (d) A thermally annealed (Q2) cluster.

Figure 3.4 shows the RDF of the 10179 atom gold nanostructures. RDF analysis of the larger Au10179 nanocluster shows that the amorphous structure has a similar pattern to that of Au923 nanocluster. But the differences between icosahedral and thermally annealed nanoclusters are relatively smaller, compared to that in the Au923 nanoclusters. We believe this small difference is caused by the ratio of internal surface atoms. In Au923 nanoclusters, the proportion of internal (core) atoms is relatively lower, compared to that in large nanoclusters. During the cooling process in thermal annealing, surface crystallization is a very important kinetic process in determining the overall structure, due to the high percentage of surface atoms and the crystallization of the surface restricts the packing process of the internal atoms of nanocluster. As a result, the internal structure cannot be well ordered.

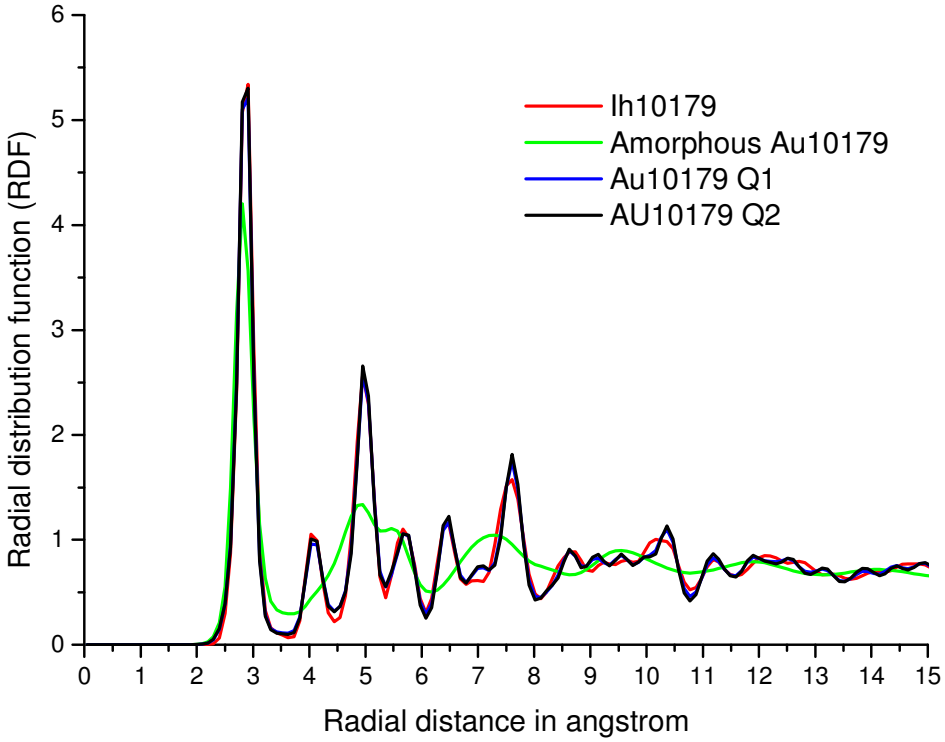


**Figure 3.4** The radial distribution function (RDF) of gold nanoclusters shown in Figure 3.3.

For the large nanocluster, due to the high percentage of internal atoms, internal crystallization would be a relatively important mechanism in determining the overall cohesive energy of nanocluster, compared to the surface crystallization, and therefore we expect the ordered internal organization of a nanocluster would exert more influence than surface reordering, in the determination of the final cluster configuration.

Finally, we use the Q2 quenched nanoclusters to compare the structure of thermal annealed nanoclusters with all the sizes we considered in this project. Figure 3.5 shows the images of thermally annealed nanoclusters (Q2) with four different sizes (ranging from 923 to 10179 atoms). From the images, we find that increasing surface reconstruction is present in the nanoclusters, as the nanocluster size increases. In a latter section of this thesis, we will show that the surface-reconstructed icosahedral nanoclusters are energetically favorable over an ideal one.

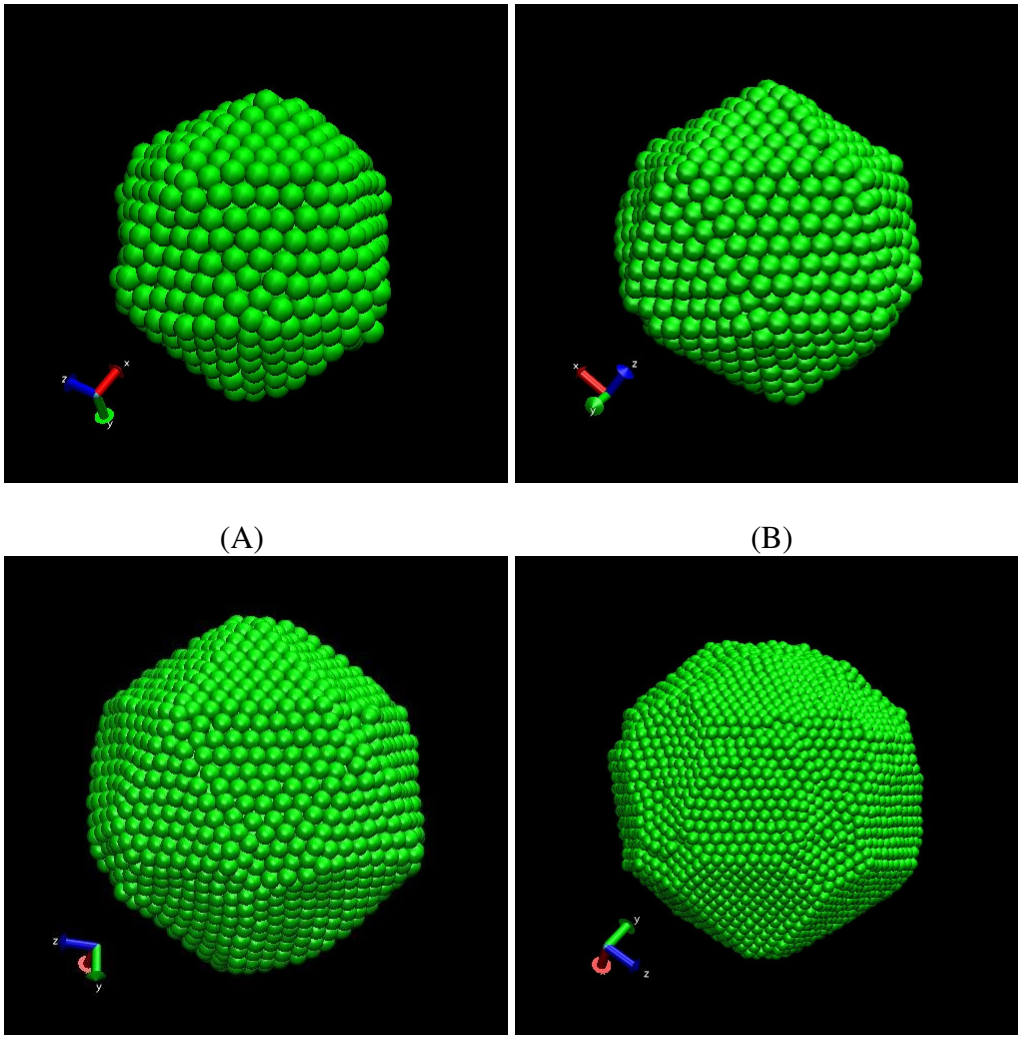

(A) (B)

(C) (D)

**Figure 3.5** Images of gold nanoclusters with different sizes: (a) An Au923 (Q2) cluster (b) An Au1415 (Q2) cluster (c) An Au3871 (Q2) cluster (d) An Au10179 (Q2) cluster.

As we would like to compare our results with the recent experimental observation of gold nanoclusters produced in helium gas [17, 18], we constructed the crystalline patterns of our Q2 thermally annealed nanoclusters as shown in Figure 3.6. Five-fold symmetry can be clearly observed in the 3871 atom cluster (of diameter of approximately 5nm) and the 10179 atom cluster (diameter of approximately 8nm), but not in the smaller nanoclusters. The crystalline patterns of the large nanocluster are found to be a good match to the high resolution electronic microscope (HREM)

images in reference 16 and 17. As we mentioned above, the internal structure of small thermally annealed nanoclusters appear less organized, compared to that in large nanoclusters.

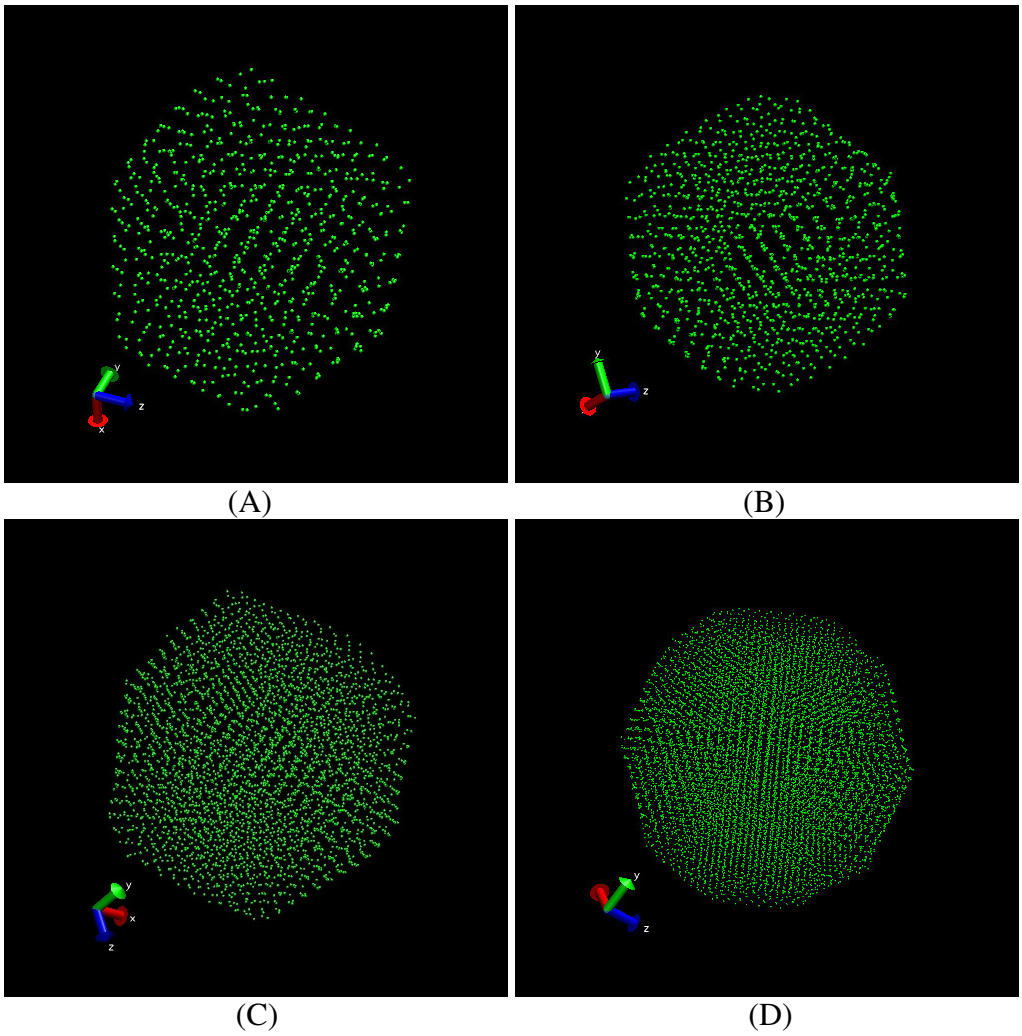

(A) (B)

(C) (D)

**Figure 3.6 is continued on the next page.**

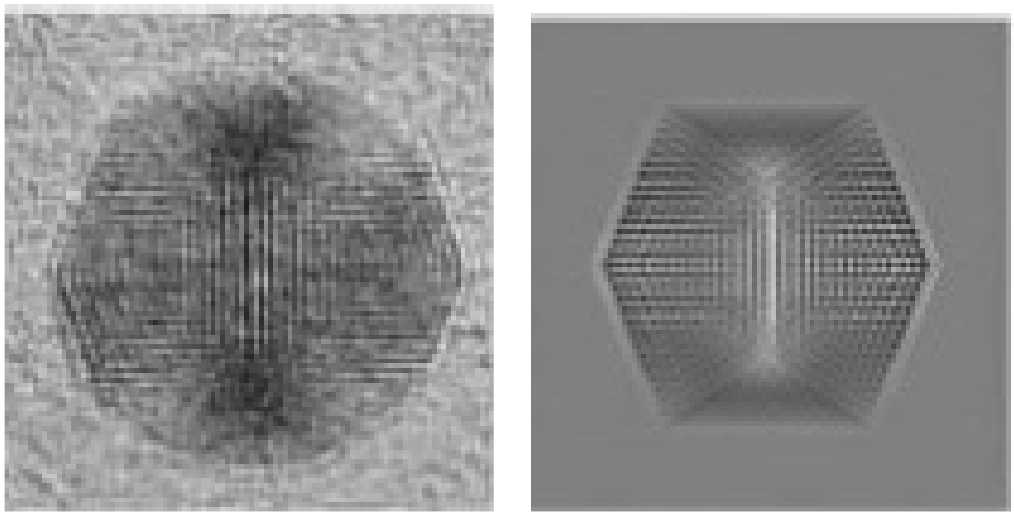

(D) (F)

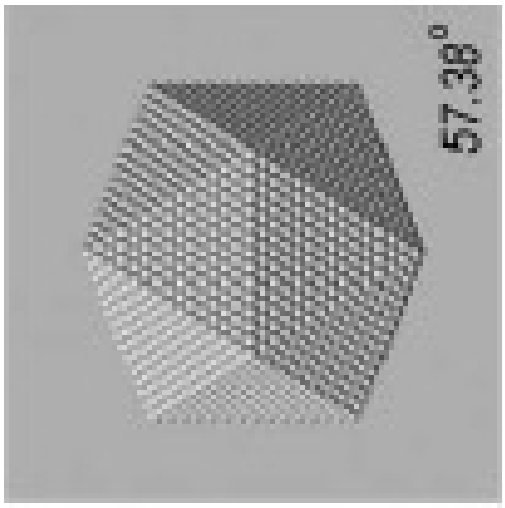


(G)

**Figure 3.6** Crystalline pattern images of gold nanoclusters with different sizes: (a) An Au923 (Q2) cluster (b) An Au1415 (Q2) cluster (c) An Au3871 (Q2) cluster (d) An Au10179 (Q2) cluster. The experimental HREM images of gold nanoparticle under vacuum (Reference 16): (E) Experimental HREM images of an Ih particle (~8nm) (F) simulated images calculated from a 14 shelled Ih model (G) The corresponding hard-sphere model.

Figure 3.7 shows the RDF of the clusters shown in Figure 3.6. The RDF graph shows the peaks becoming more well-defined, as the nanocluster size increases.

Although the positions of the peaks are a little shifted, the patterns of the RDF for the different sizes of nanoclusters are very similar. This means that the nanoclusters within the size range we considered largely retained an icosahedral-like structure after the thermal annealing process, which is in good agreement with experimental findings [17,18]. In these experimental studies, the icosahedral motif is the dominated one within the size range in our study (diameter = 3.5 - 8 nm), while the other common motifs, such as fcc and decahedral structures, are nearly absent.

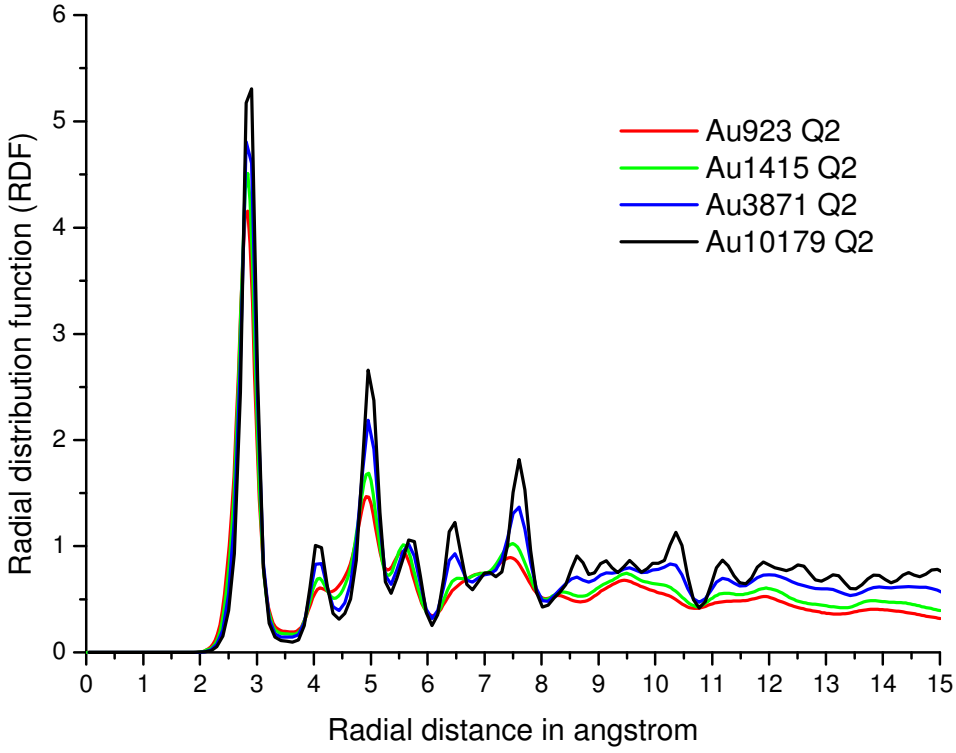


**Figure 3.7** Radial distribution function (RDF) of gold nanoclusters shown in Figure 3.6.

Before this study, gold nanoclusters had been theoretically studied for over a decade. As ab-initio calculations are still not possible for gold nanoclusters larger than approximately 200 atoms, studies of gold nanoclusters have proceeded using semi-empirical and empirical atomic potentials. For gold nanoclusters, although different structures of the same size range have been predicted by using different atomic

potentials, the lack of experimental result for “naked” clusters (without surfactant or ligand protection) make the comparison to experiment difficult. The presence of surfactant molecules may drastically change the structural morphology of gold nanocluster under the same physical conditions of temperature and pressure. Recently an experimental study giving a detailed statistical population analysis of gold nanoclusters grown in helium gas has been presented [17, 18], therefore we can now make a more direct comparison between our theoretical results and experiment. As Helium is inert, the interaction between the gold surface and helium occurs only via a weak intermolecular force. As a result, the structural morphology would at most, only be slightly affected by its chemical environment.

For the structure of the annealed gold nanoclusters, surface reconstructions, such as atomic relaxation near to a vertex, absence of an atom at a vertex position and the presence of steps, are believed to be the main factors for their higher stability, compared to ideal icosahderal nanoclusters. Unfortunately, such reconstruction is hard to observe in HRTEM or AFM, as the size of nanoclusters are very small. Therefore a major aim of this project was to determine structural morphology of gold nanoclusters using a more quantitative method than the RDF. The method we used is based on Planar graph ring sequences and is discussed in section 2.4.2. In the next section we discuss our results using this method.

## 3.3 Planar graph ring sequences

### 3.3.1 Small nanoclusters

The crystallization and geometrical rearrangement of the core atoms upon freezing can be clearly shown using Planar Graphs of the clusters at various temperatures. Figure 3.8 shows the results from the Q1 923 atom quenched cluster at various temperatures. Classification of the core particles at 800 K, 700 K, 500 K and 298 K

are shown in figures 3.8(a), 3.8(c), 3.8(e) and 3.8(g) respectively.

The colors of the **core** particles correspond to their local structural geometric arrangement based on the planar graphs and are as follows:

FCC - **GREEN**

HCP - **BLUE**

Defective FCC - **BLACK**

Defective HCP - **GREY**

Icosahedral and twisted icosahedral – **RED**

Stacking fault – **VIOLET**

Other types of defect rearrangement – **NOT CLASSIFIED AND ATOMS NOT SHOWN**

The colors of the **surface** are shown as followings:

Surface atoms – **YELLOW**

Surface atoms showing five-fold symmetry - **BLACK**

In figures 3.8(a), 3.8(c), 3.8(e), and 3.8(g) the surface atoms are labeled by the smaller radii yellow particles, so that the core atoms can be clearly observed. In figures 3.8(b), 3.8(d), 3.8(f) and 3.8(g) the surface atoms corresponding to the clusters on the left are observed, fivefold symmetry is indicated by the black shaded surface atoms. Figure 3.8 clearly shows that at 800 K the cluster core is disordered and that from 700 K crystallization of the nanocluster proceeds from the surface toward the core region which is in agreement with the observations of Nam [11] in their study of the freezing of 561 atom gold nanoclusters.

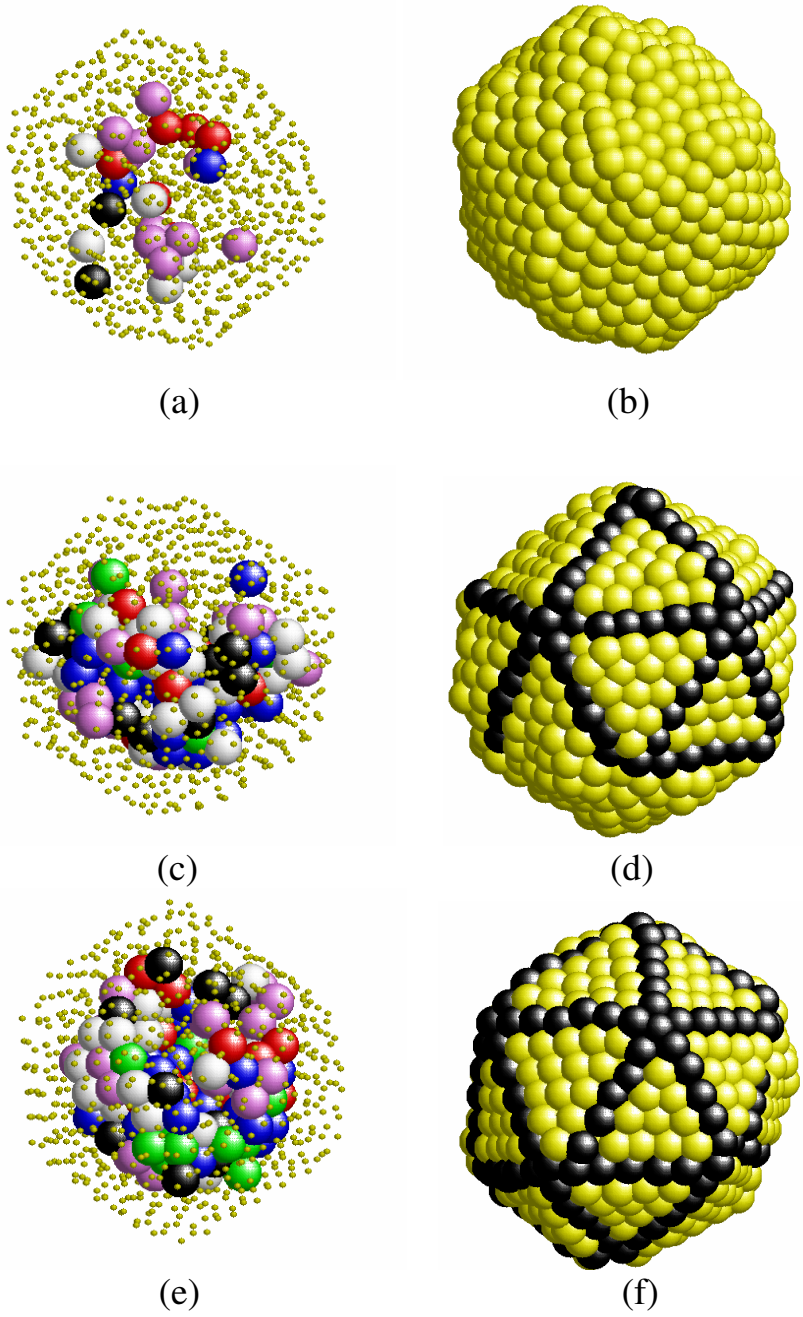

(a) (b)

(c) (d)

(e) (f)

**Figure 3.8 is continued on the next page.**

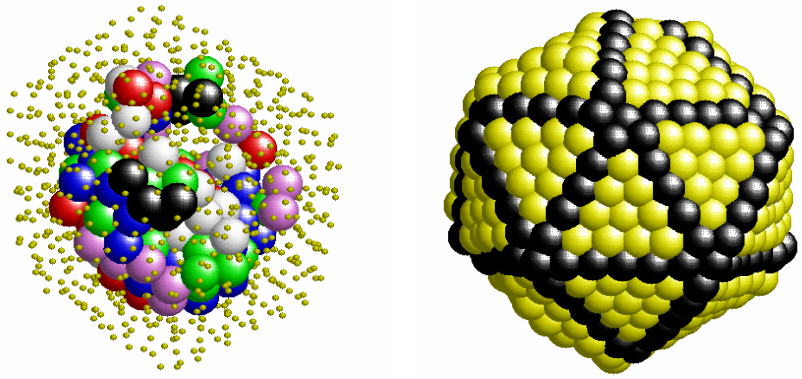

(g) (h)

**Figure 3.8** (LEFT) Classification of the core particles at (a) 800 K (c) 700 K (e) 500 K (g) 298 K. The colours of the core particles correspond to their topological classification based on Planar Graphs, green-FCC, blue-HCP, black-defected FCC, grey- defected HCP, red- Ih and twisted Ih, violet-stacking fault. (RIGHT) Surface atoms corresponding to figures on the left. The black shaded atoms indicated regions of five-fold symmetry.

The possible causes of the surface crystallization preceding that of the core include the added atomic freedom of the surface atoms, lower relocation energy on the surface and the formation of stable (111) planes. At 298K the core is dominated by FCC/defected FCC and HCP/defected HCP packing. Ideally, an icosahedral structure consists of 20 slightly distorted FCC tetrahedra with four (111) facets each meeting at the center. The internal facets of the FCC tetrahedra meet at twin planes with a local HCP structure. Figure 3.9 gives the relative percentages of (i) FCC/ defected FCC, (ii) HCP/ defected HCP, (iii) Icosahedral/ twisted icosahedral and (iv) Stacking fault coordination, in the Q1 quenched structure as a function of quenching temperature. We also show the relative percentages corresponding to a perfect Ih at 298K.

The figure indicates a large difference between the core structure of a Q1 quenched and perfect Ih nanocluster, in that, the relative percentages of FCC/ defected FCC

and HCP/ defected HCP sites in the Q1 quenched structure is only half of that of a perfect icosahedral cluster.

The effect of kinetics on the formation of the Ih structure can be seen from figure 3.10. Figure 3.10 (a), (c) and (e) gives the Planar Graph characterization of the core particles, at thermal equilibrium at 298K, for the quench Q1, Q2 and perfect Ih nanoclusters respectively. The colours of the core particles correspond to the same geometric classification as in figure 3.8. The Ih structure (Figure 3.10e) shows the internal facets of the FCC tetrahedra meeting at twin planes with HCP structure. The core of the Q2 quenched cluster (figure 3.10c), which was three times slower than the Q1 cluster (figure 3.10a) is much closer to that of the idealized Ih core strongly indicating that kinetics does play an important role in the formation of Ih structures as suggested by Shim et al. [13]. The result indicates that slower cooling (Q2) provides sufficient time for core atoms in the gold nanocluster to form a more crystalline structure after surface freezing. Therefore the morphology of structures grown in an inert atmosphere may be controlled by controlling the cooling rate. The Figures 3.10(b), 3.10(d) and 3.10(f) show the surface atoms corresponding to the Q1, Q2 and Ih clusters. Figure 3.10 (a) and 3.10 (b) in particular shows that the ordering of the surface occurs before that of the core 298 K.

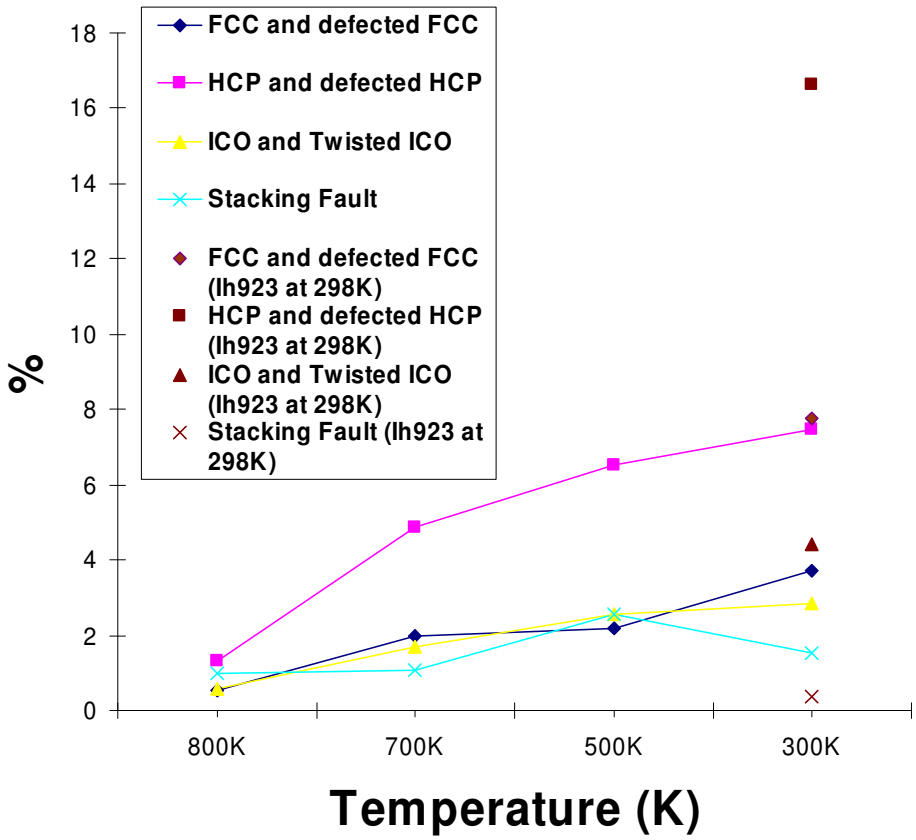


**Figure 3.9** The relative percentages of (i) FCC/ defected FCC, (ii) HCP/ defected HCP, (iii) Icosahedral/ twisted icosahedral and (iv) Stacking fault coordination in the Q1 quenched structure as a function of quenching temperature. The relative percentages corresponding to a perfect Ih at 298K is also shown.

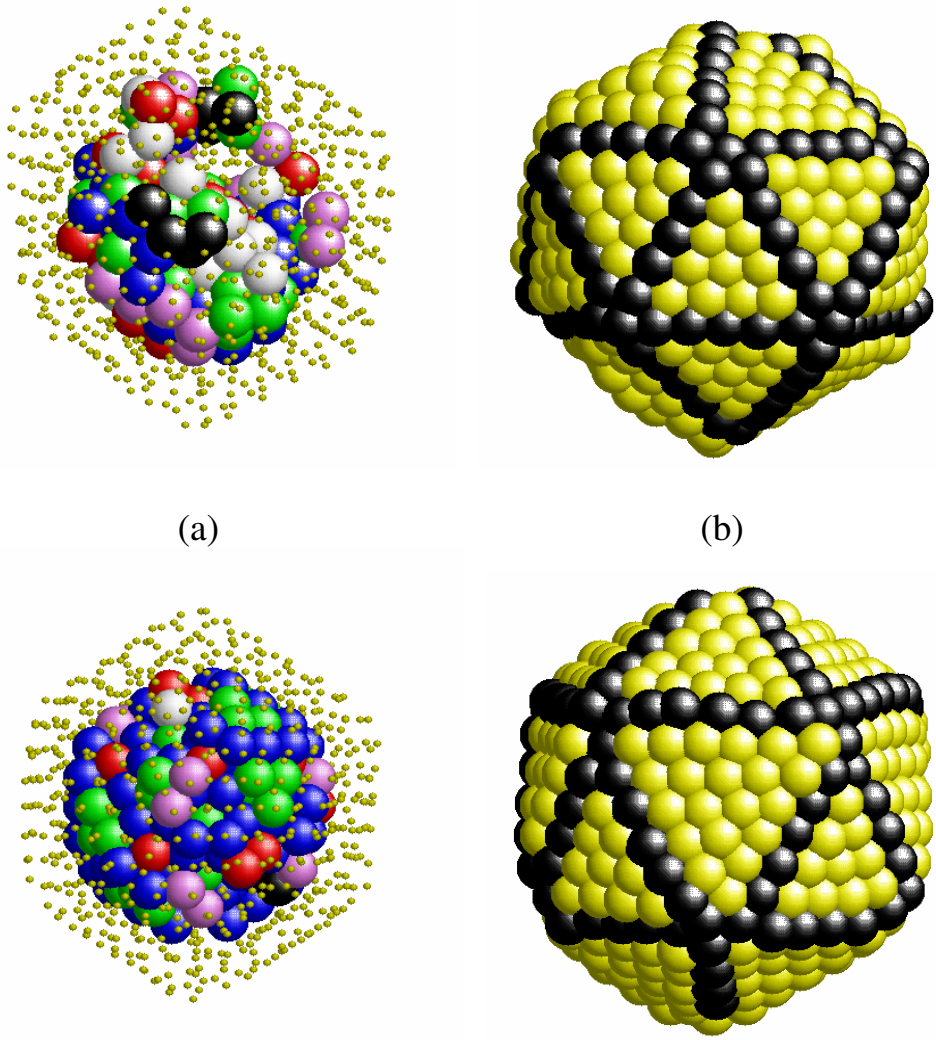

(a) (b)

(c) (d)

**Figure 3.10 is continued on the next page.**

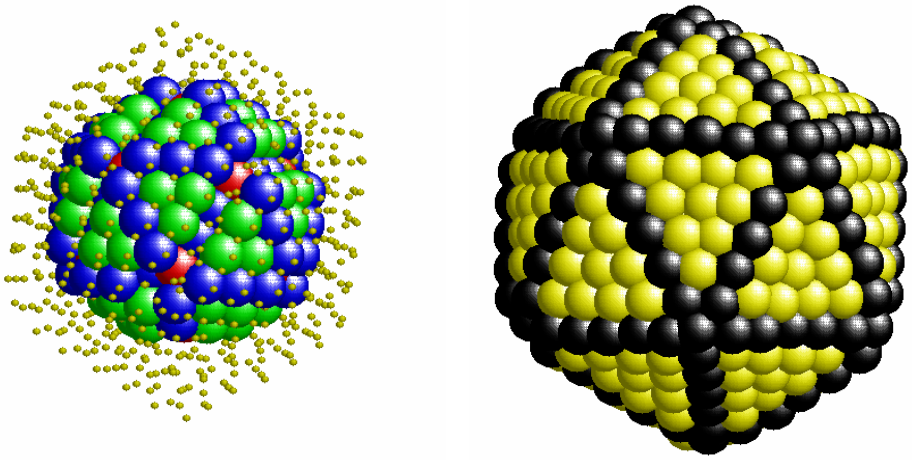

(e) (f)

**Figure 3.10** (LEFT) Classification of the core particles at 298K, (a) Q1 (c) Q2 (e) Ih for the Au923 atom clusters. The colours of the core particles correspond to their topological classification based on Planar Graphs, green-FCC, blue-HCP, black-defected FCC, grey- defected HCP, red- Ih and twisted Ih, violet-stacking fault. The surface atoms are labelled in yellow with small radii. (RIGHT) Surface atoms of clusters (b) Q1 (d) Q2 (f) Ih at 298 K corresponding to the core atoms on the LEFT. Fivefold symmetry is indicated by the black shaded surface atoms.

### 3.3.2 Large Nanoclusters

Using our planar graph classification scheme we have also analyzed the ordering of the cluster cores as a function of cluster size. Figures 3.11 and 3.12 show the classification of the core particles in the fastest (Q1, figure 3.11) and slowest (Q3, figure 3.12) quenched nanoclusters at 298K. From the figures, we found that the hexagonal close packed (HCP) planes and face centered cubic (FCC) fragments in five-fold symmetry are clearly observed in the Au3871 and Au10179 nanoclusters. In contrast, only small and disordered FCC and HCP local structures are found in the Au923 and Au1415 nanoclusters. Figures 3.11 and 3.12 show that the quench rate also affects the disorder in the larger nanocluster cores. For the Au3871 and

Au10179 nanoclusters, more well-ordered planes and fragments are formed in slowly quenched (Q3) nanoclusters (Figure 3.12). The effect of quench rate on structure is not significant in smaller nanoclusters. Five-fold symmetry can be clearly observed in 3871 and 10179 atom nanoclusters, and this result is supported by the recent high resolution Transmission Electron Microscopy (HRTEM) work of gold nanoclusters in helium gas by Koga et.al. [17,18]. In their studies Koga found that the icosahedral motif was the dominant one within the size range of our larger clusters (3.5 - 8 nm), while the other common motifs, such as fcc and decahedral structures, were nearly absent.

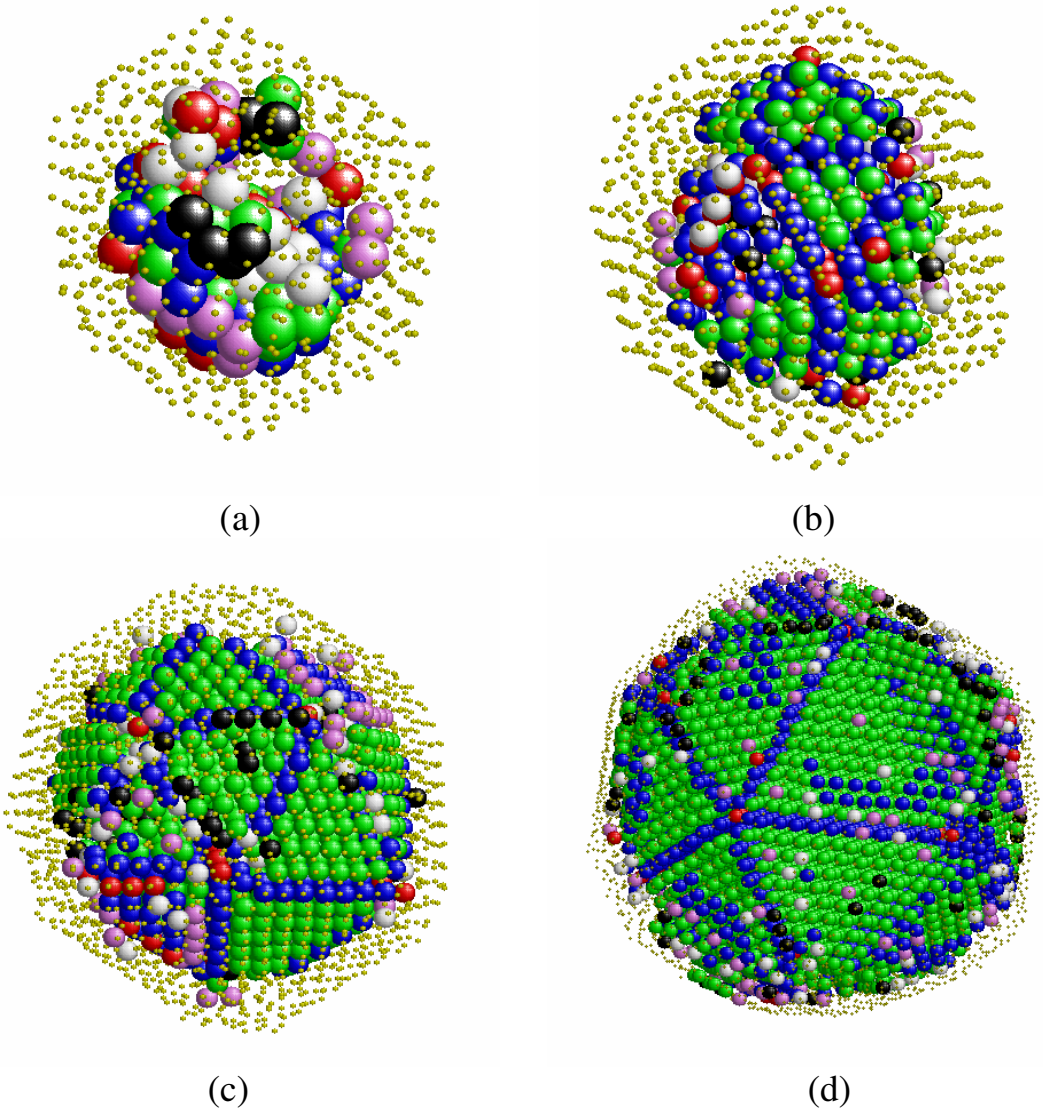


**Figure 3.11** Classification of the core particles at 298K (i) Q1 Au923 (ii) Q1 Au1415 (iii) Q1 Au3871 (iv) Q1 Au10179. The colours of the core particles correspond to their topological classification based on Planar Graphs, green-FCC, blue-HCP, black-defected FCC, grey- defected HCP, red- Ih and twisted Ih, violet-stacking fault. The surface atoms are labelled in yellow with smaller radii.

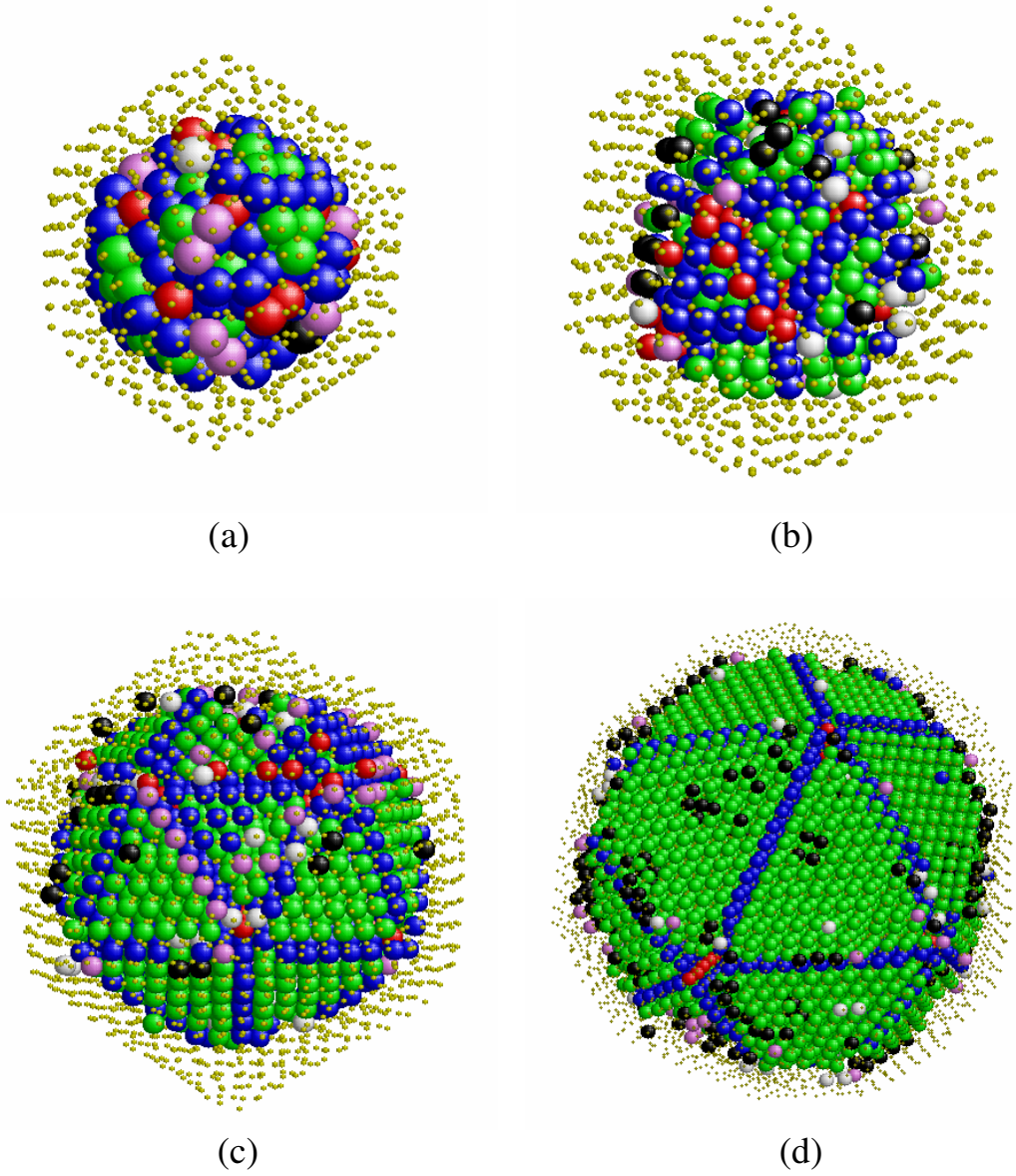


**Figure 3.12** Classification of the core particles at 298K (i) Q3 Au923 (ii) Q3 Au1415 (iii) Q3 Au3871 (iv) Q3 Au10179. The colours of the core particles correspond to their topological classification based on Planar Graphs, green-FCC, blue-HCP, black-defected FCC, grey- defected HCP, red- Ih and twisted Ih, violet-stacking fault. The surface atoms are labelled in yellow with smaller radii.

Comparison of the experimental results of Koga et al. with our findings suggests that EAM glue potential provides a good unified description of the bulk, defect and surface of gold [19]. This potential can correctly predict the most possible structures from molecular dynamics simulations within the nanocluster size range we

considered. In contrast to the glue potential, the original EAM potential predicted the decahedral and even octahedral structures are the most stable for nanocluster of less than 500 atoms [20].

In addition to the graphical representation of the cluster core atoms, the statistics of local ring sequencing also give clear indication for the structural characteristics of gold nanoclusters. In table 3.1 and 3.2, the percentages of types of all local ring sequencing are very low or even zero for amorphous and liquid nanoclusters. Compared to the percentages for icosahedral nanoclusters at 298K, the slowest quenching rate (Q3) gives the closest crystalline structure to the icosahedral nanoclusters. Although Q1 is a faster cooling rate than Q2, it gives slightly more ordered structures than Q2 does. In section 3.2.1 we suggested, based on analysis of the Au923 atom clusters, that for growth in an inert atmosphere, quench-rate may be a controlling parameter for controlling morphology and crystallinity. The Q1 and Q2 results in table 3.1 also suggest that if this is the case, it is only true once the quench-rate is sufficiently slow.

Overall, this technique of planar graphs has enabled us to quantitatively explore the detailed structural coordination of the nanocluster core particles as a function of growth conditions in our molecular dynamics simulation which is currently difficult to do experimentally.

| **AMOR Au923** | **Local Rings** | **Percentage** | **Au923 q1** | **Local Rings** | **Percentage** |
|---|---|---|---|---|---|
| | (8 6) fcc | 0 | | (8 6) fcc | 3.466956 |
| | (8 6) hcp | 0 | | (8 6) hcp | 8.775731 |
| | (20 0) icosahedra | 0.325027 | | (20 0) icosahedra | 0.108342 |
| | (10 5) twisted icosahedra | 0 | | (10 5) twisted icosahedra | 3.358613 |
| | (10 5) fcc | 0 | | (10 5) fcc | 1.191766 |
| | (10 5) hcp | 0.108342 | | (10 5) hcp | 1.733478 |
| **Liquid Au923 at 1400K** | **Local Rings** | **Percentage** | **Au923 q2** | **Local Rings** | **Percentage** |
| | (8 6) fcc | 0 | | (8 6) fcc | 3.358613 |
| | (8 6) hcp | 0 | | (8 6) hcp | 6.933911 |
| | (20 0) icosahedra | 0 | | (20 0) icosahedra | 0 |
| | (10 5) twisted icosahedra | 0 | | (10 5) twisted icosahedra | 2.383532 |
| | (10 5) fcc | 0 | | (10 5) fcc | 0.541712 |
| | (10 5) hcp | 0 | | (10 5) hcp | 2.383532 |
| **Ih 923** | **Local Rings** | **Percentage** | **Au 923 q3** | **Local Rings** | **Percentage** |
| | (8 6) fcc | 7.908992 | | (8 6) fcc | 3.791983 |
| | (8 6) hcp | 15.059588 | | (8 6) hcp | 9.209101 |
| | (20 0) icosahedra | 0 | | (20 0) icosahedra | 0.108342 |
| | (10 5) twisted icosahedra | 2.491874 | | (10 5) twisted icosahedra | 3.033586 |
| | (10 5) fcc | 0.541712 | | (10 5) fcc | 0.866739 |
| | (10 5) hcp | 0.975081 | | (10 5) hcp | 2.166847 |

**Table 3.1** Statistics of planar graph local ring sequencing of Au923 nanoclusters of different morphologies.

| **AMOR Au10179** | **Local Rings** | **Percentage** | **Au10179 q1** | **Local Rings** | **Percentage** |
|---|---|---|---|---|---|
| | (8 6) fcc | 0.461735 | | (8 6) fcc | 33.20562 |
| | (8 6) hcp | 0.540328 | | (8 6) hcp | 12.840161 |
| | (20 0) icosahedra | 0.275076 | | (20 0) icosahedra | 0 |
| | (10 5) twisted icosahedra | 0.157186 | | (10 5) twisted icosahedra | 0.618921 |
| | (10 5) fcc | 0.844877 | | (10 5) fcc | 2.858827 |
| | (10 5) hcp | 1.178898 | | (10 5) hcp | 2.004126 |
| **Liquid Au10179 at 1400K** | **Local Rings** | **Percentage** | **Au10179 q2** | **Local Rings** | **Percentage** |
| | (8 6) fcc | 0 | | (8 6) fcc | 32.90107 |
| | (8 6) hcp | 0 | | (8 6) hcp | 15.296198 |
| | (20 0) icosahedra | 0.039297 | | (20 0) icosahedra | 0 |
| | (10 5) twisted icosahedra | 0.009824 | | (10 5) twisted icosahedra | 0.795756 |
| | (10 5) fcc | 0.019648 | | (10 5) fcc | 2.966893 |
| | (10 5) hcp | 0.019648 | | (10 5) hcp | 1.532567 |
| **Ih 10179** | **Local Rings** | **Percentage** | **Au 10179 q3** | **Local Rings** | **Percentage** |
| | (8 6) fcc | 38.235584 | | (8 6) fcc | 37.577366 |
| | (8 6) hcp | 17.359268 | | (8 6) hcp | 11.523726 |
| | (20 0) icosahedra | 0 | | (20 0) icosahedra | 0 |
| | (10 5) twisted icosahedra | 1.20837 | | (10 5) twisted icosahedra | 0.510856 |
| | (10 5) fcc | 1.738874 | | (10 5) fcc | 3.919835 |
| | (10 5) hcp | 1.532567 | | (10 5) hcp | 1.778171 |

**Table 3.2** Statistics of planar graph local ring sequencing of Au10179 nanoclusters of different morphologies.

## 3.4 Bond angle distribution analysis

In this section, we compare the bond angle distribution between the Q1 quenched Au 923 and Au3871 nanoclusters at 298K, with the distribution of bulk gold at 298K using the glue potential. Figures 3.13-3.19 show the combined contribution to the bond angle distribution from shortest-path (SP) ring sequences of different sizes making up the nanoclusters, and also the contribution from each individual ring size. Tables 3.3-3.6 show the peak width, height, area and position in bond angle distribution. In the bond angle distribution from the combined contribution (Figure 3.13), narrower and well defined peaks can be found in the distribution of bulk gold. Generally the Au3871 nanocluster gives sharper (narrower and higher) peaks than Au923 does. It is due to larger fcc fragments in the Au3871 nanocluster, and the better statistics in the bond angle distribution.

Although the width and height of the peaks of Au923, Au3871 and bulk gold are different, the agreement in peak positions is good. For the 3-membered rings (Figure 3.14), the nanoclusters peaks are more diffuse, compared to that of bulk gold. The peaks from 4-membered rings (Figure 3.15) show very good agreement, with the exception of their height. As the 4-membered ring peak is associated with the (100) planes of the fcc crystal [21], good agreement in 4-membered ring contribution may indicate that the fcc structure is dominant in the gold nanoclusters. In the plot of 5-membered ring contribution (Figure 3.16), board peaks for Au923 and Au3871 nanoclusters are observed, while showing a very small contribution of 5-membered ring for bulk gold at 298K. The presence of 5-membered ring indicates the disorder in a crystal structure, as there should be no 5-membered ring content in the ring statistics of an ideal fcc crystal. The small 5-membered ring contribution in bulk gold at 298K is due to the restricted movement of gold atoms in the crystal structure at finite temperature. The boarder peak for Au923 nanoclusters indicates

the degree of disorder inside Au923 is higher, compared to Au3871.

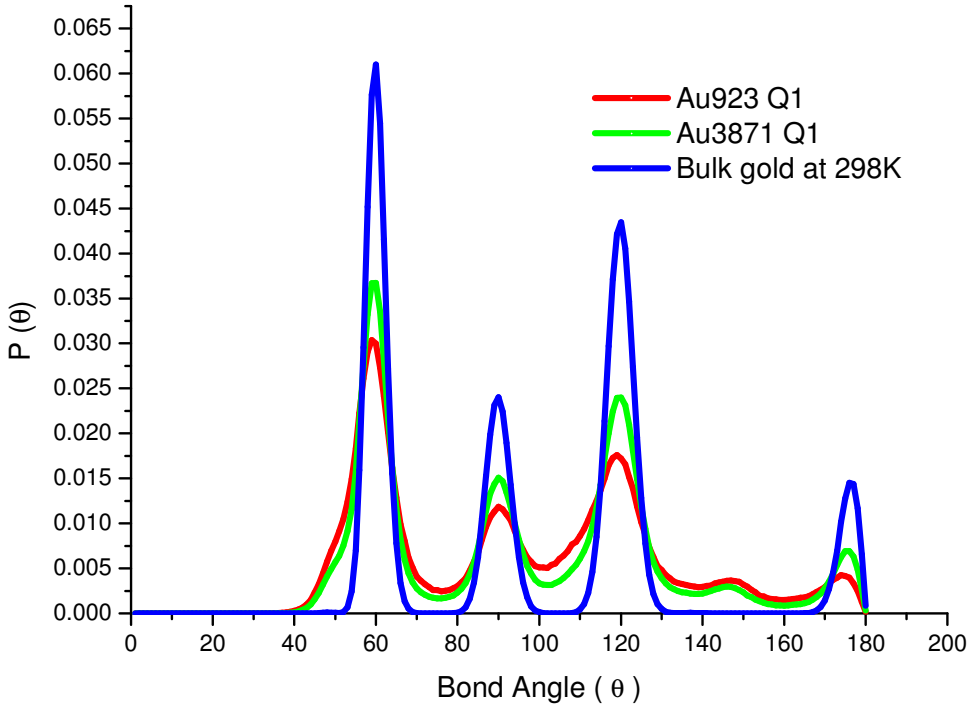


**Figure 3.13** Combined contribution of the bond angle distribution from shortest-path (SP) ring sequences of different sizes at 298K, for the Au923 (red), Au3871 (green) nanoclusters and bulk gold (blue).

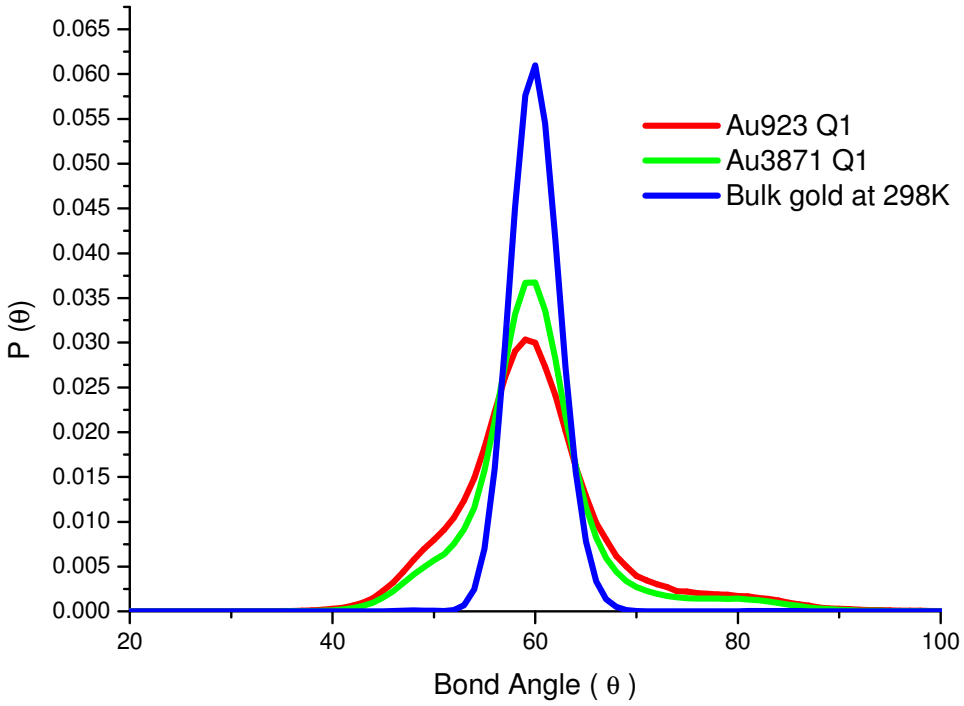


**Figure 3.14** The 3-membered ring contribution to the bond angle distribution of the Au923 nanocluster, Au3871 nanocluster and bulk gold at 298K.

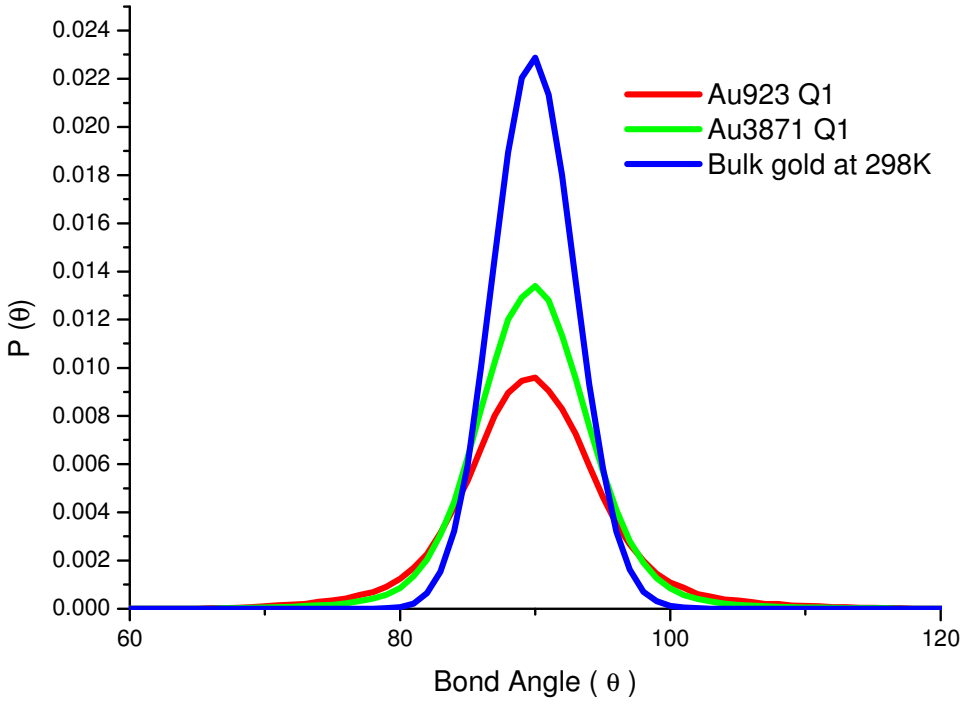


**Figure 3.15** The 4-membered ring contribution to the bond angle distribution of the Au923 nanocluster, Au3871 nanocluster and bulk gold at 298K.

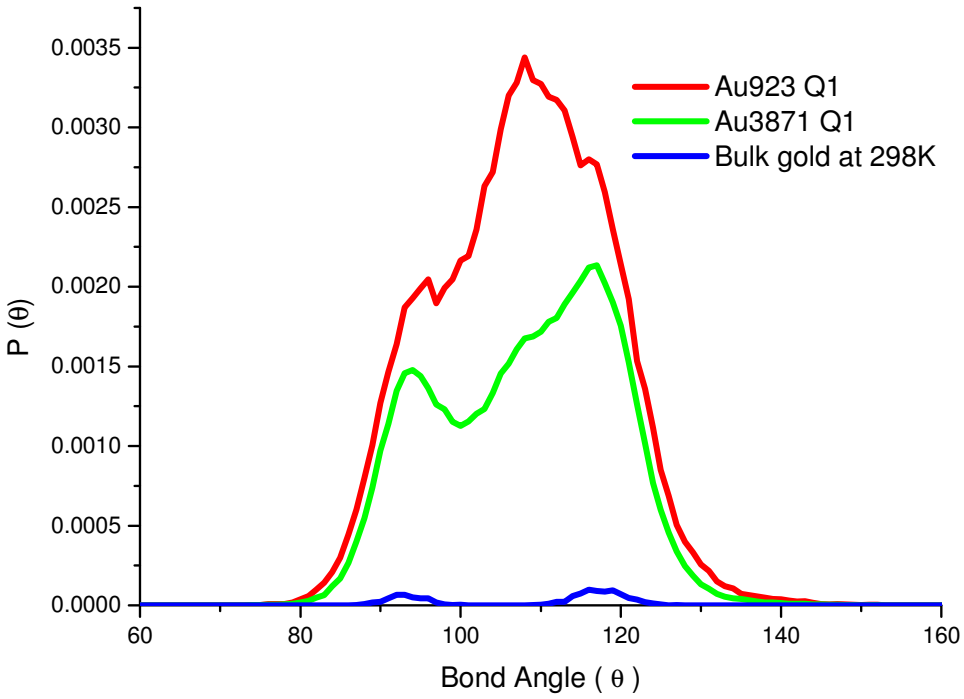


**Figure 3.16** The 5-membered ring contribution to the bond angle distribution of the Au923 nanocluster, Au3871 nanocluster and bulk gold at 298K.

| Ring size | System | Peak width | Peak height | Peak area |
|---|---|---|---|---|
| 3 | Amorphous Au923 | 13.71 | 0.022238 | 0.3821 |
| | Ih923 | 9.153 | 0.030303 | 0.34762 |
| | Au923 q1 | 10.265 | 0.027924 | 0.35925 |
| | Bulk gold at 298K | 4.9637 | 0.059607 | 0.37082 |
| **Ring size** | **System** | **Peak width** | **Peak height** | **Peak area** |
| 4 | Amorphous Au923 | 14.835 | 0.0040008 | 0.074384 |
| | Ih923 | 7.1442 | 0.016737 | 0.14986 |
| | Au923 q1 | 7.6121 | 0.014976 | 0.14287 |
| | Bulk gold at 298K | 6.145 | 0.022605 | 0.17409 |
| **Ring size** | **System** | **Peak width** | **Peak height** | **Peak area** |
| 5 | Amorphous Au923 | 20.427 | 0.0068157 | 0.17449 |
| | Ih923 | 8.178,14.493 | 0.0015759,0.0033973 | 0.016152,0.061711 |
| | Au923 q1 | 8.2798,18.686 | 0.0012021,0.0033774 | 0.012474,0.079098 |
| | Bulk gold at 298K | 5.168,6.3561 | 7.0899E-5,1.0765E-4 | 4.5922E-4,8.5754E-4 |
| **Ring size** | **System** | **Peak width** | **Peak height** | **Peak area** |
| 6 type 1 | Amorphous Au923 | 20.905 | 0.0036834 | 0.096509 |
| | Ih923 | 9.6341 | 0.014977 | 0.18084 |
| | Au923 q1 | 11.353 | 0.011394 | 0.16212 |
| | Bulk gold at 298K | 6.6783 | 0.036129 | 0.3024 |
| **Ring size** | **System** | **Peak width** | **Peak height** | **Peak area** |
| 6 type 2 | Amorphous Au923 | 22.829 | 0.0017875 | 0.051143 |
| | Ih923 | 16.469 | 0.001708 | 0.035254 |
| | Au923 q1 | 17.395 | 0.0020493 | 0.044679 |
| | Bulk gold at 298K | 6.6913 | 0.004434 | 0.037185 |
| **Ring size** | **System** | **Peak width** | **Peak height** | **Peak area** |
| 6 type 3 | Amorphous Au923 | 28.109 | 0.0021076 | 0.074251 |
| | Ih923 | 9.5418,9.7712 | 0.0029603,0.0040582 | 0.035402,0.049698 |
| | Au923 q1 | 14.378,9.5541 | 0.0023657,0.0036639 | 0.042631,0.043873 |
| | Bulk gold at 298K | 4.8742 | 0.013103 | 0.080043 |

**Table 3.3** Peak width, height and area of the bond angle distribution of Au923 nanoclusters of morphologies from different sizes of rings at 298K.

| Ring size | System | Bond angle | Ideal Planar value |
|---|---|---|---|
| 3 | Amorphous Au923 | 58.356 | 60 |
| | Ih923 | 59.213 | |
| | Au923 q1 | 59.05 | |
| | Bulk gold at 298K | 59.911 | |
| **Ring size** | **System** | **Bond angle** | **Ideal Planar value** |
| 4 | Amorphous Au923 | 88.889 | 90 |
| | Ih923 | 89.894 | |
| | Au923 q1 | 89.862 | |
| | Bulk gold at 298K | 89.916 | |
| **Ring size** | **System** | **Bond angle** | **Ideal Planar value** |
| 5 | Amorphous Au923 | 107.15 | 108 |
| | Ih923 | 92.893,110.75 | |
| | Au923 q1 | 92.889,110.18 | |
| | Bulk gold at 298K | 93.260,117.35 | |
| **Ring size** | **System** | **Bond angle** | **Ideal Planar value** |
| 6 type 1 | Amorphous Au923 | 118.06 | 120 |
| | Ih923 | 119.12 | |
| | Au923 q1 | 119.1 | |
| | Bulk gold at 298K | 119.88 | |
| **Ring size** | **System** | **Bond angle** | **Ideal Planar value** |
| 6 type 2 | Amorphous Au923 | 121.07 | 120 |
| | Ih923 | 122.66 | |
| | Au923 q1 | 120.74 | |
| | Bulk gold at 298K | 119.8 | |
| **Ring size** | **System** | **Bond angle** | **Ideal Planar value** |
| 6 type 3 | Amorphous Au923 | 159.74 | 180 |
| | Ih923 | 147.80,173.55 | |
| | Au923 q1 | 148.08,173.15 | |
| | Bulk gold at 298K | 175.86 | |

**Table 3.4** Peak positions of the bond angle distribution of Au923 nanoclusters of morphologies from different sizes of rings at 298K.

| Ring size | System | Peak width | Peak height | Peak area |
|---|---|---|---|---|
| 3 | Amorphous Au3871 | 12.477 | 0.023408 | 0.36604 |
| | Ih3871 | 7.3312 | 0.036925 | 0.33928 |
| | Au3871 q1 | 7.8177 | 0.035002 | 0.34295 |
| | Bulk gold at 298K | 4.9637 | 0.059607 | 0.37082 |
| **Ring size** | **System** | **Peak width** | **Peak height** | **Peak area** |
| 4 | Amorphous Au3871 | 13.128 | 0.0054144 | 0.089083 |
| | Ih3871 | 7.1128 | 0.016259 | 0.14494 |
| | Au3871 q1 | 8.0762 | 0.013176 | 0.13337 |
| | Bulk gold at 298K | 6.145 | 0.022605 | 0.17409 |
| **Ring size** | **System** | **Peak width** | **Peak height** | **Peak area** |
| 5 | Amorphous Au3871 | 21.745 | 0.005998 | 0.16347 |
| | Ih3871 | 7.8951,15.135 | 9.7424E-4, 0.0016032 | 0.0096402,0.030412 |
| | Au3871 q1 | 10.827,15.044 | 0.0013455,0.0021159 | 0.018257,0.039895 |
| | Bulk gold at 298K | 5.168,6.3561 | 7.0899E-5,1.0765E-4 | 4.5922E-4,8.5754E-4 |
| **Ring size** | **System** | **Peak width** | **Peak height** | **Peak area** |
| 6 type 1 | Amorphous Au3871 | 17.339 | 0.0055904 | 0.12148 |
| | Ih3871 | 8.6473 | 0.023403 | 0.25364 |
| | Au3871 q1 | 9.0695 | 0.019333 | 0.21976 |
| | Bulk gold at 298K | 6.6783 | 0.036129 | 0.3024 |
| **Ring size** | **System** | **Peak width** | **Peak height** | **Peak area** |
| 6 type 2 | Amorphous Au3871 | 22.055 | 0.001814 | 0.050142 |
| | Ih3871 | 15.949 | 0.0011526 | 0.023039 |
| | Au3871 q1 | 15.756 | 0.0016027 | 0.031648 |
| | Bulk gold at 298K | 6.6913 | 0.004434 | 0.037185 |
| **Ring size** | **System** | **Peak width** | **Peak height** | **Peak area** |
| 6 type 3 | Amorphous Au3871 | 32.488 | 0.002223 | 0.090518 |
| | Ih3871 | 8.2762, 6.2948 | 0.0025985,0.0077231 | 0.026953,0.060931 |
| | Au3871 q1 | 12.790, 6.7705 | 0.0019818,0.0065754 | 0.031767,0.055796 |
| | Bulk gold at 298K | 4.8742 | 0.013103 | 0.080043 |

**Table 3.5** Peak width, height and area of the bond angle distribution of Au3871 nanoclusters of morphologies from different sizes of rings at 298K.

| Ring size | System | Bond angle | Ideal Planar value |
|---|---|---|---|
| 3 | Amorphous Au3871 | 58.499 | 60 |
| | Ih3871 | 59.554 | |
| | Au3871 q1 | 59.48 | |
| | Bulk gold at 298K | 59.911 | |
| **Ring size** | **System** | **Bond angle** | **Ideal Planar value** |
| 4 | Amorphous Au3871 | 89.176 | 90 |
| | Ih3871 | 89.892 | |
| | Au3871 q1 | 89.85 | |
| | Bulk gold at 298K | 89.916 | |
| **Ring size** | **System** | **Bond angle** | **Ideal Planar value** |
| 5 | Amorphous Au3871 | 107.69 | 108 |
| | Ih3871 | 93.717,113.06 | |
| | Au3871 q1 | 94.796,114.04 | |
| | Bulk gold at 298K | 93.260,117.35 | |
| **Ring size** | **System** | **Bond angle** | **Ideal Planar value** |
| 6 type 1 | Amorphous Au3871 | 118.7 | 120 |
| | Ih3871 | 119.51 | |
| | Au3871 q1 | 119.67 | |
| | Bulk gold at 298K | 119.88 | |
| **Ring size** | **System** | **Bond angle** | **Ideal Planar value** |
| 6 type 2 | Amorphous Au3871 | 121.75 | 120 |
| | Ih3871 | 123.69 | |
| | Au3871 q1 | 121.21 | |
| | Bulk gold at 298K | 119.8 | |
| **Ring size** | **System** | **Bond angle** | **Ideal Planar value** |
| 6 type 3 | Amorphous Au3871 | 162.41 | 180 |
| | Ih3871 | 147.43, 175.06 | |
| | Au3871 q1 | 147.61,174.74 | |
| | Bulk gold at 298K | 175.86 | |

**Table 3.6** Peak positions of the bond angle distribution of Au3871 nanoclusters of morphologies from different sizes of rings at 298K.

In these clusters, the 6-membered rings are the basic structural components of the close packed planes of the fcc or hcp crystal. A close packed plane can be considered as being an overlapping tiling of the 6-membered rings. Figure 3.17 and 3.18 show the 6-membered ring (type 1) and (type 2) contribution to the bond angle

distribution of the Au923 nanocluster, the Au3871 nanocluster and bulk gold at 298K respectively. They show the clear difference between gold nanoclusters and bulk gold. The extended bulk gold crystal structure gives higher and narrower peaks of the 6-membered ring type 1 and 2, compared to that of gold nanoclusters. For the 6-membered ring type 3 (Figure 3.19), there is splitting into two peaks at 148° and 177° respectively, compared to the one single sharp peak of bulk gold at 177°. In an ideal FCC crystal the angle for 6-membered ring type 3 is 180° while for the stable fcc hard sphere crystal at a density of 1.05 the mean angle is equal to 170° [21]. The observation here may be due to the buckling and bending of close packed plane in fcc structure of gold nanocluster. Also, for the Au3871 nanocluster a higher peak at 177° and a lower peak at 148° are observed, compared to that of the Au923 nanocluster. This may indicate that a more regular fcc structure is formed in the larger Au3871 nanocluster.

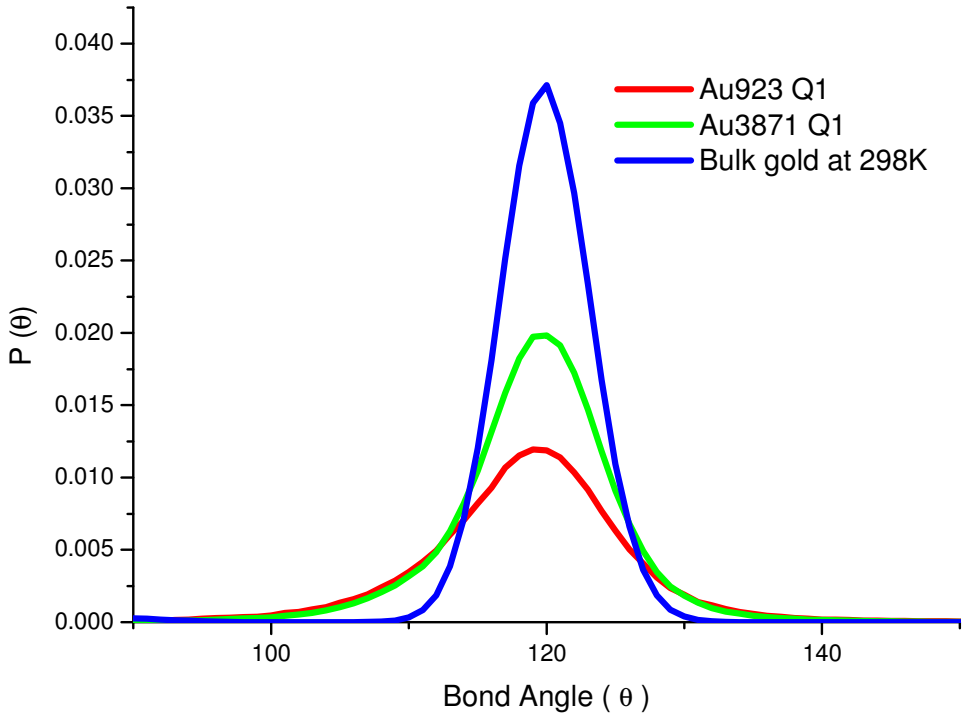


**Figure 3.17** The 6-membered ring (type 1) contribution to the bond angle distribution of the Au923 nanocluster, Au3871 nanocluster and bulk gold at 298K.

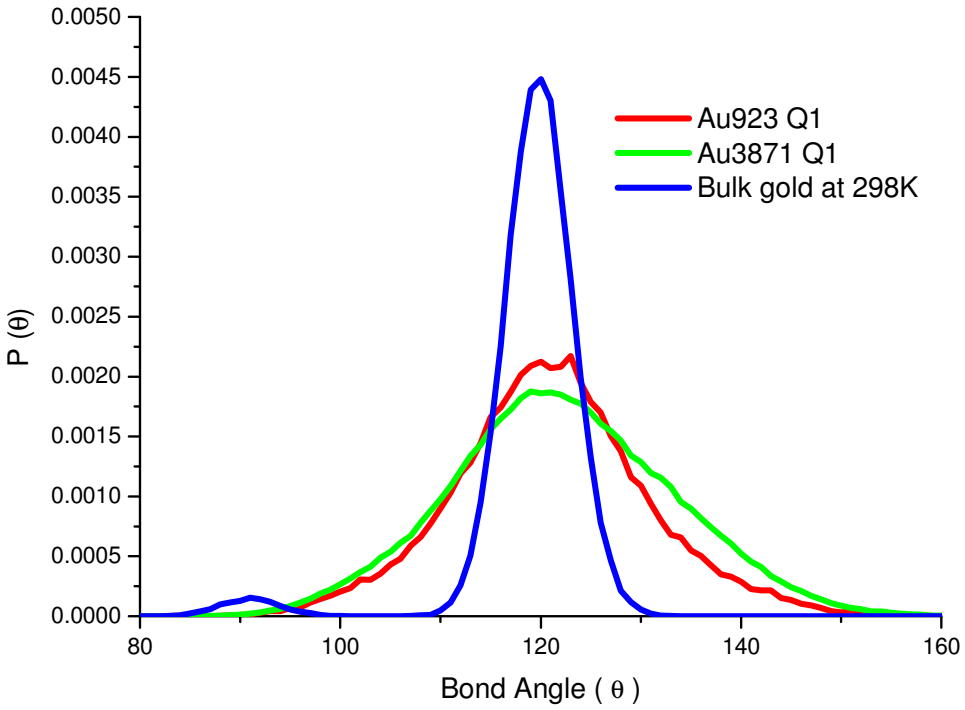


**Figure 3.18** The 6-membered ring (type 2) contribution for to the bond angle distribution of the Au923 nanocluster, Au3871 nanocluster and bulk gold at 298K.

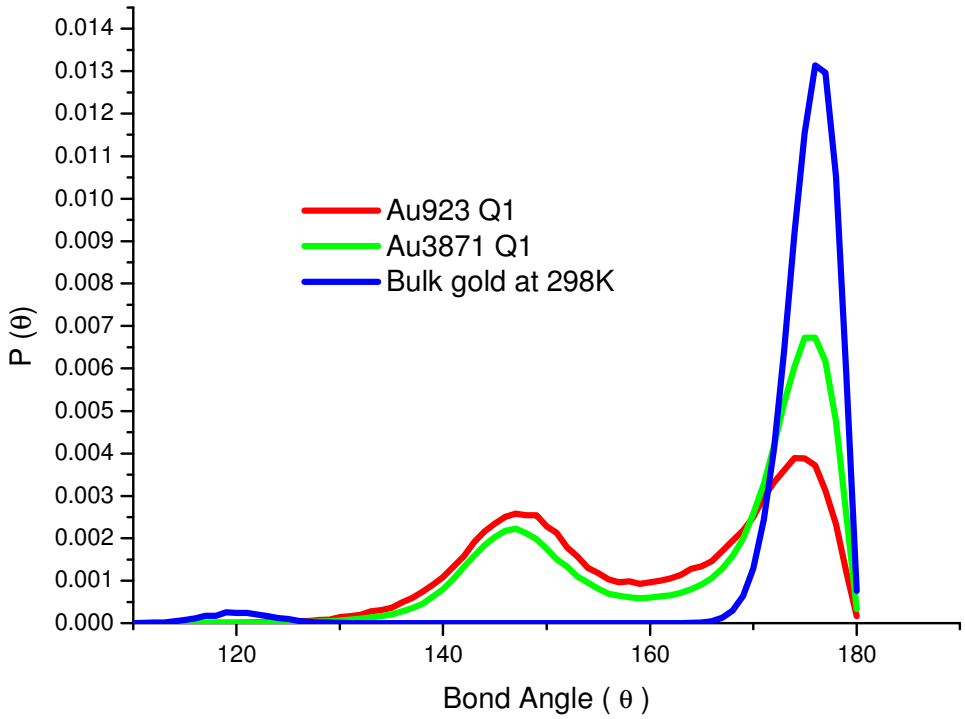


**Figure 3.19** The 6-membered ring (type 3) contribution to the bond angle distribution of the Au923 nanocluster, Au3871 nanocluster and bulk gold at 298K.

Figures 3.20-3.26 show the SP ring sequences contributions to the bond angle distribution for the various types of Au923 atom clusters (i.e. icosahedral, Q1 quenched, amorphous) compared to bulk gold, with all structures at 298K. Figure 3.27-3.33 give the corresponding contributions for the Au3871 atom nanoclusters, again compared to bulk gold. In Figure 3.20 and Figure 3.27, there is a good agreement in the bond angle distribution between the perfect icosahedral and thermally annealed nanoclusters at finite temperature. For the amorphous nanocluster, the position of the 3-membered ring peak (Figure 3.21 and 3.28) in the bond angle distribution is close to that of the ordered nanoclusters. There are no sharp and well defined 4-membered ring (Figure 3.22 and 3.29) peaks in the amorphous nanocluster. While in the contribution of the 5-membered ring (Figure 3.23 and 3.30) to the amorphous nanocluster, a large and broad peak which is from 80 to 140 degrees is observed. These show that the bond angle analysis is very

sensitive to the ordered and disordered crystal structures, which is important to the study of nucleation and melting of nano-crystalline system. The contribution from 6-membered rings of type 1, 2 and 3 are shown in Figures 3.24-3.26 and Figure 3.31-3.33 for the Au923 and Au3871 nanoclusters respectively. The peaks of 6-membered ring type 1 of amorphous Au923 and Au3871 nanoclusters are obviously lower than the others, while the peaks of 6-membered ring type 2 of all nanoclusters of the same sizes are closer. For type 3, the amorphous nanoclusters give low and broad peaks from 140° to180°. These figures show that for both the Au923 and Au3871 clusters, the peak heights for the 3,4 and 6 membered rings in the amorphous structure is lower than that in the Ih and thermally annealed nanoclusters, indicating that there is a few close-packed planes in the amorphous structured nanoclusters.

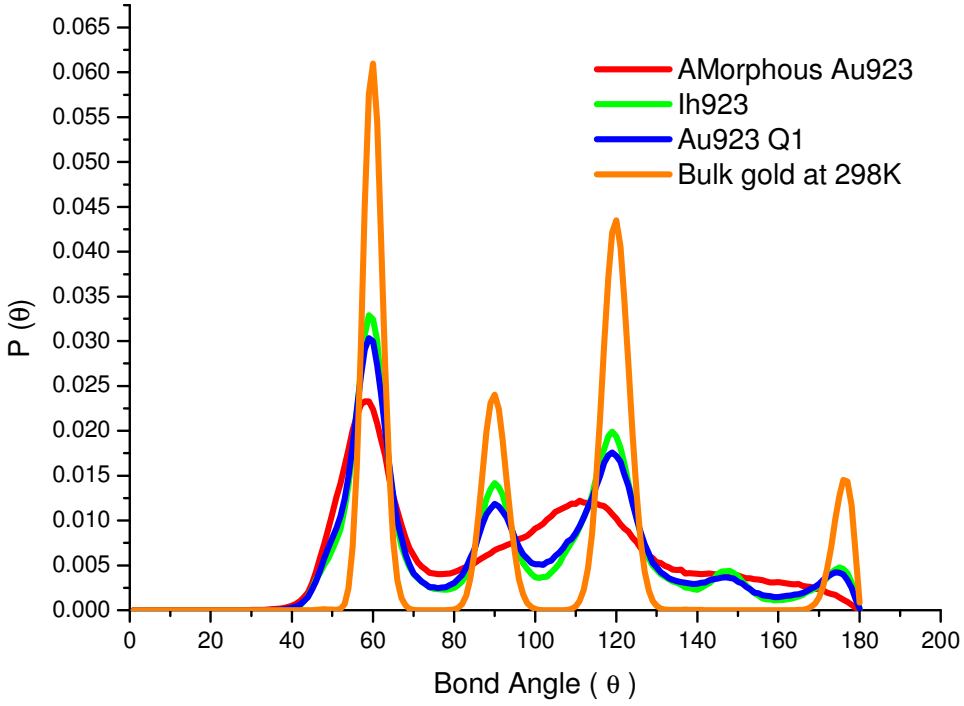


**Figure 3.20** The combined contribution to the bond angle distribution of Au923 nanoclusters of different morphologies from different sizes of rings at 298K.

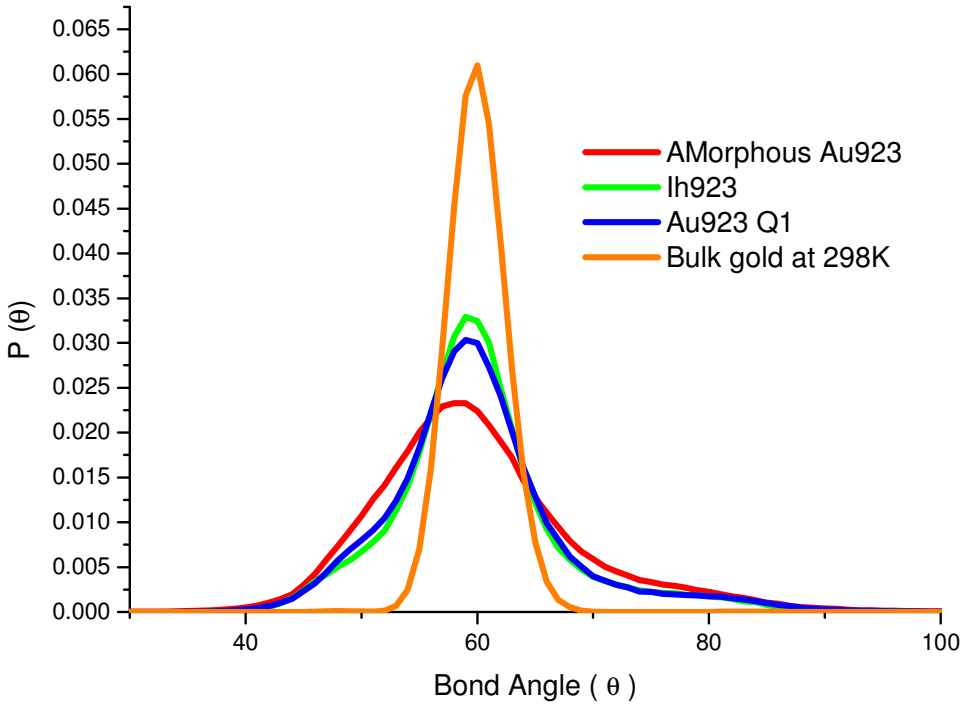


**Figure 3.21** The 3-membered ring contribution to the bond angle distribution of Au923 nanoclusters of different morphologies at 298K.

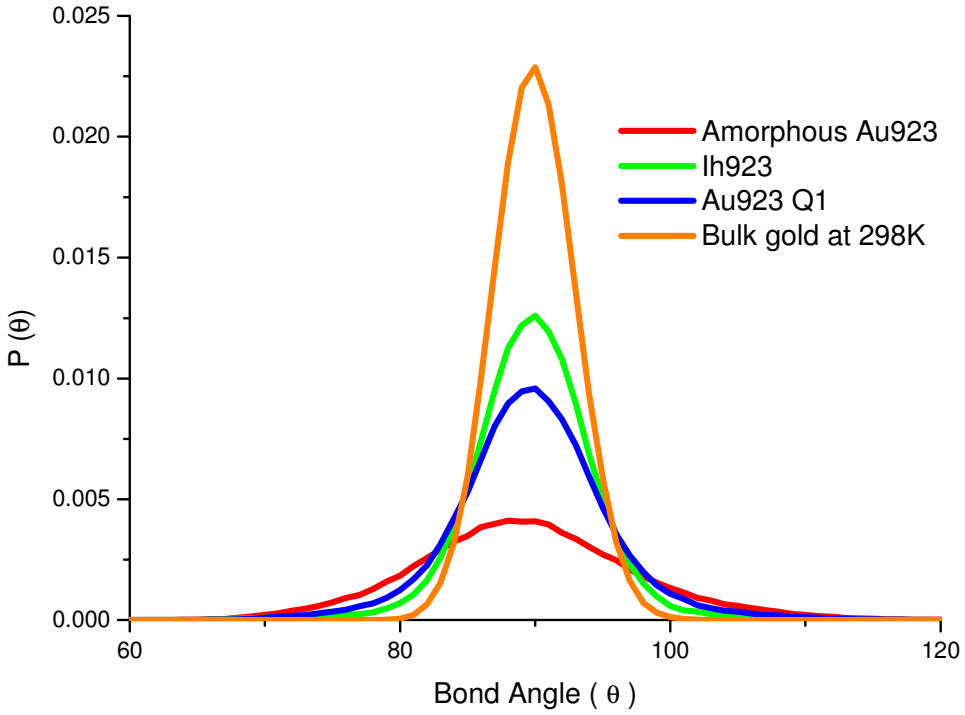


**Figure 3.22** The 4-membered ring contribution to the bond angle distribution of Au923 nanoclusters of different morphologies at 298K.

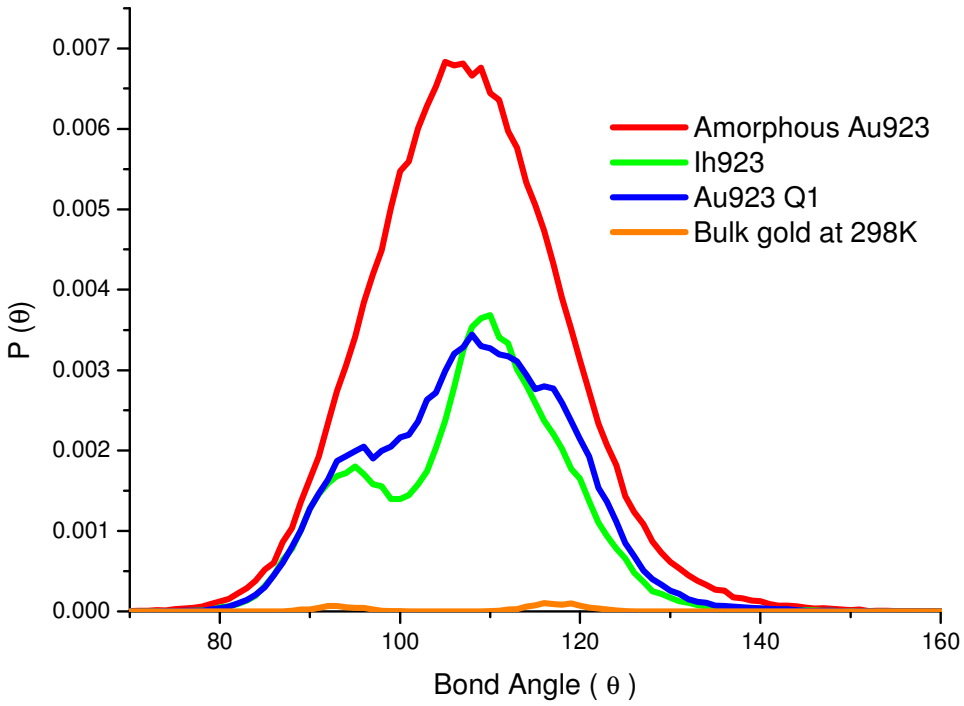


**Figure 3.23** The 5-membered ring contribution to the bond angle distribution of Au923 nanoclusters of different morphologies at 298K.

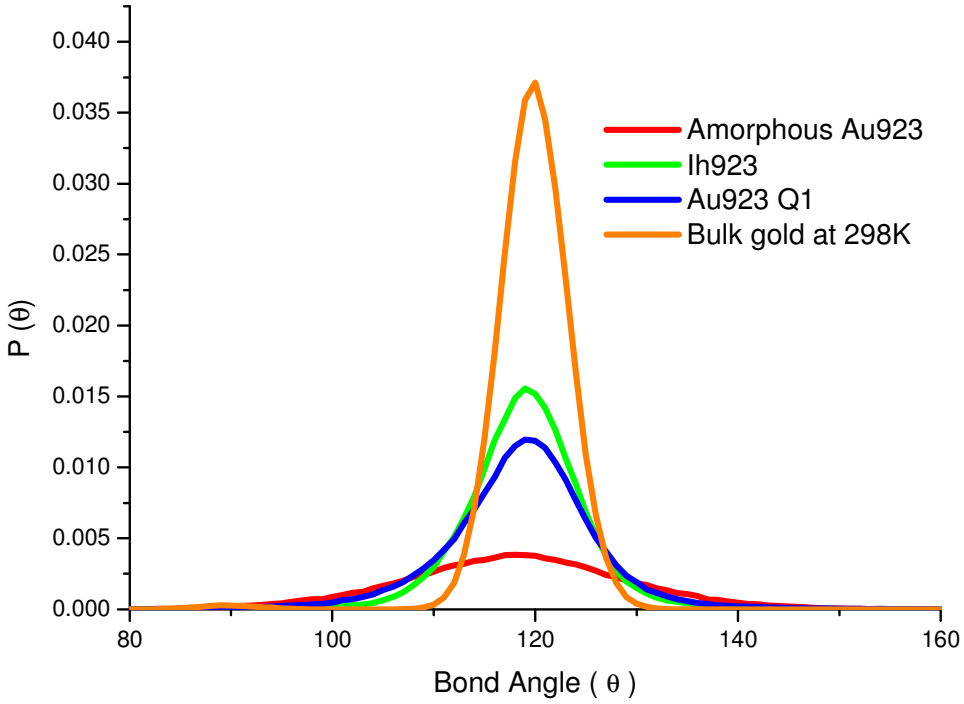


**Figure 3.24** The 6-membered ring (type 1) contribution to the bond angle distribution of Au923 nanoclusters of different morphologies at 298K.

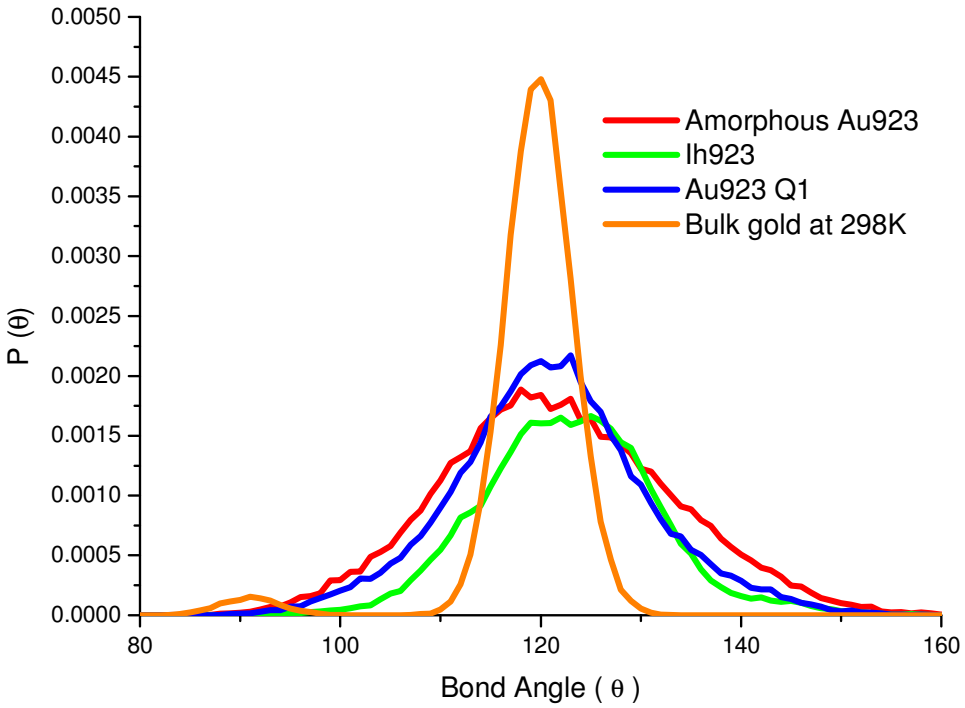


**Figure 3.25** The 6-membered ring (type 2) contribution to the bond angle distribution of Au923 nanoclusters of different morphologies at 298K.

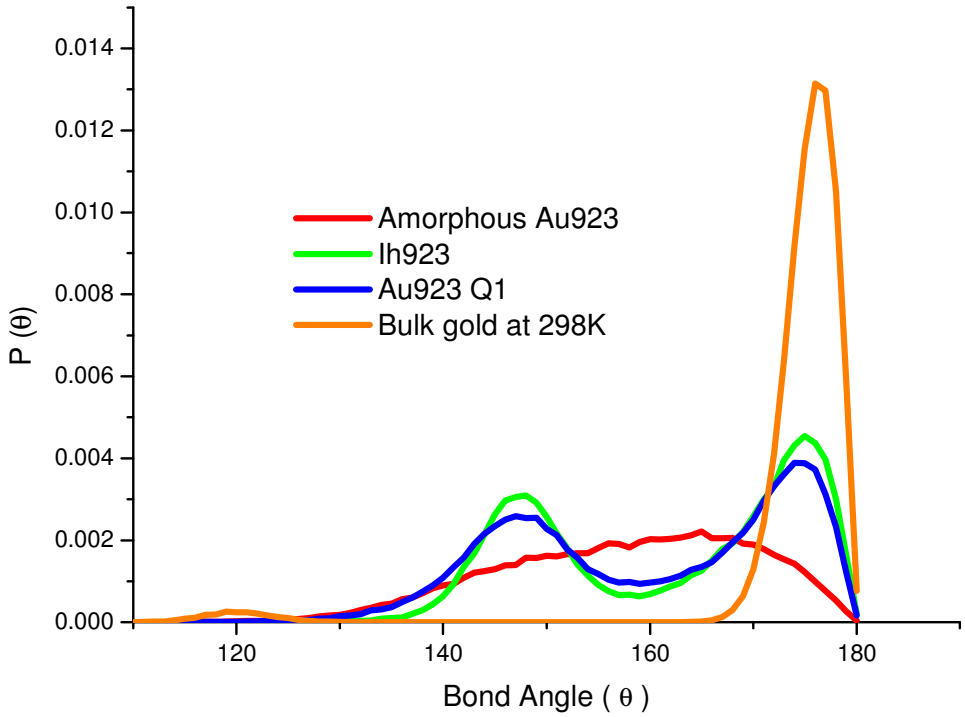


**Figure 3.26** The 6-membered ring (type 3) contribution to the bond angle distribution of Au923 nanoclusters of different morphologies at 298K.

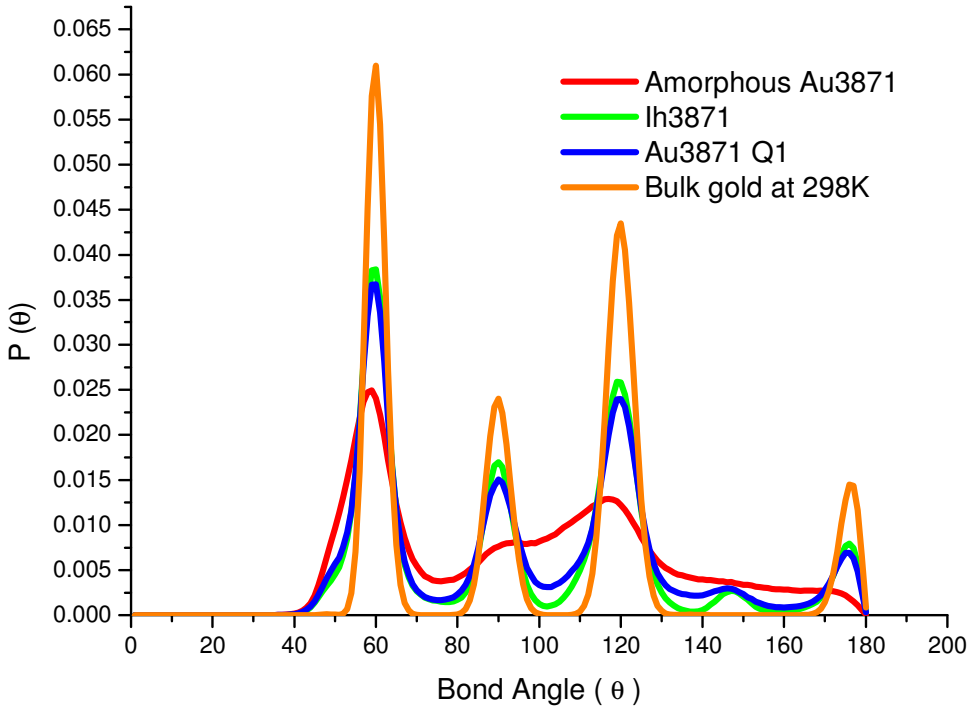


**Figure 3.27** The combined contribution to the bond angle distribution of Au3871 nanoclusters of different morphologies from different sizes of rings at 298K.

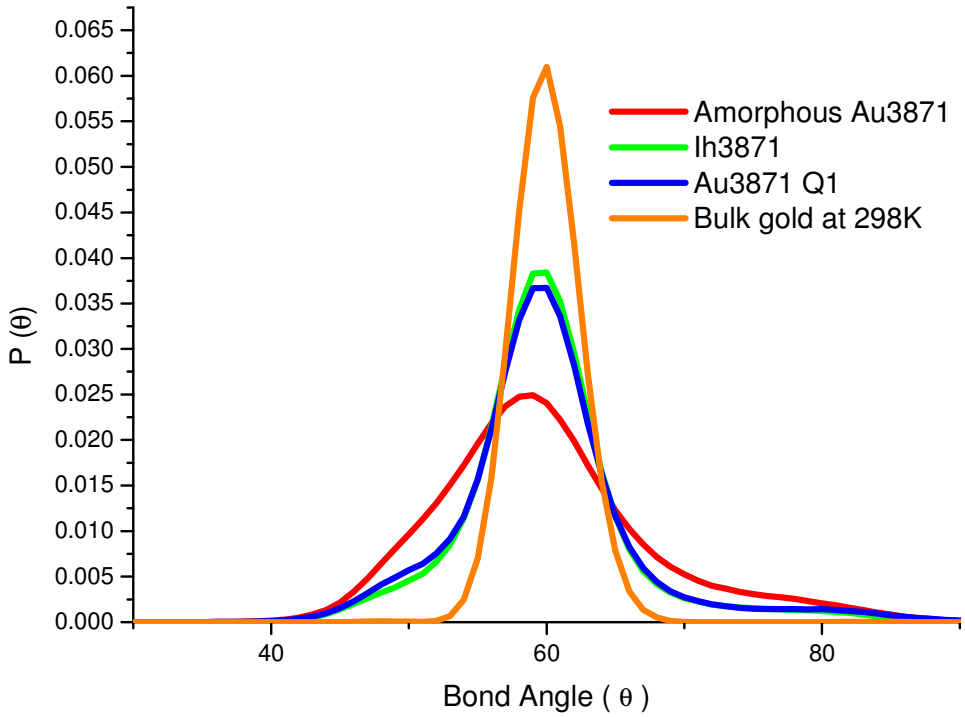


**Figure 3.28** The 3-membered ring contribution to the bond angle distribution of Au3871 nanoclusters of different morphologies at 298K.

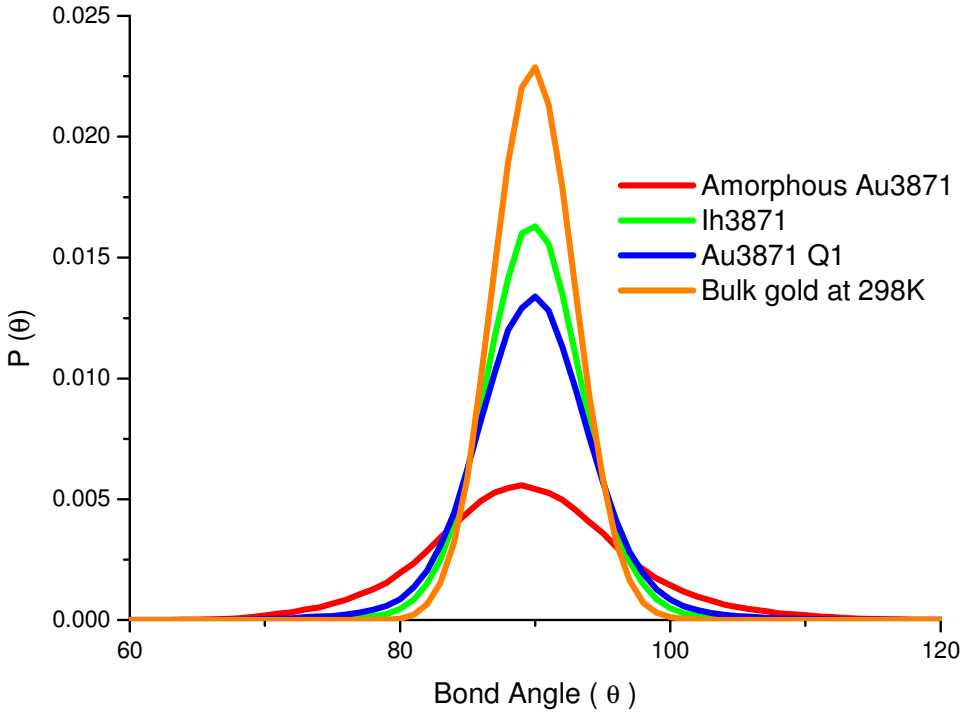


**Figure 3.29** The 4-membered ring contribution to the bond angle distribution of Au3871 nanoclusters of different morphologies at 298K.

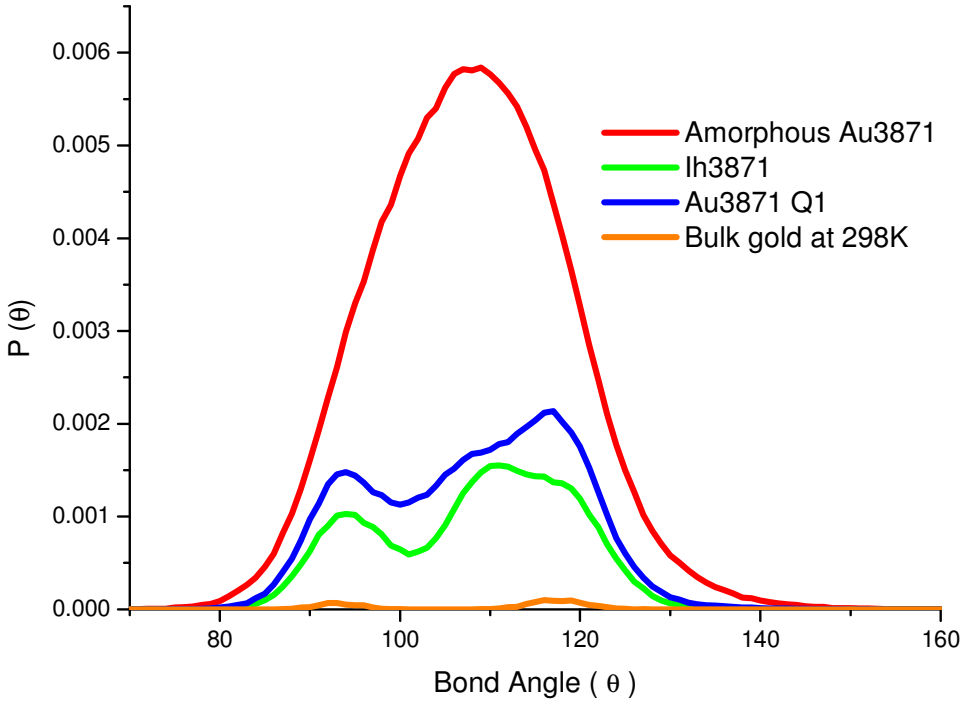


**Figure 3.30** The 5-membered ring contribution to the bond angle distribution of Au3871 nanoclusters of different morphologies at 298K.

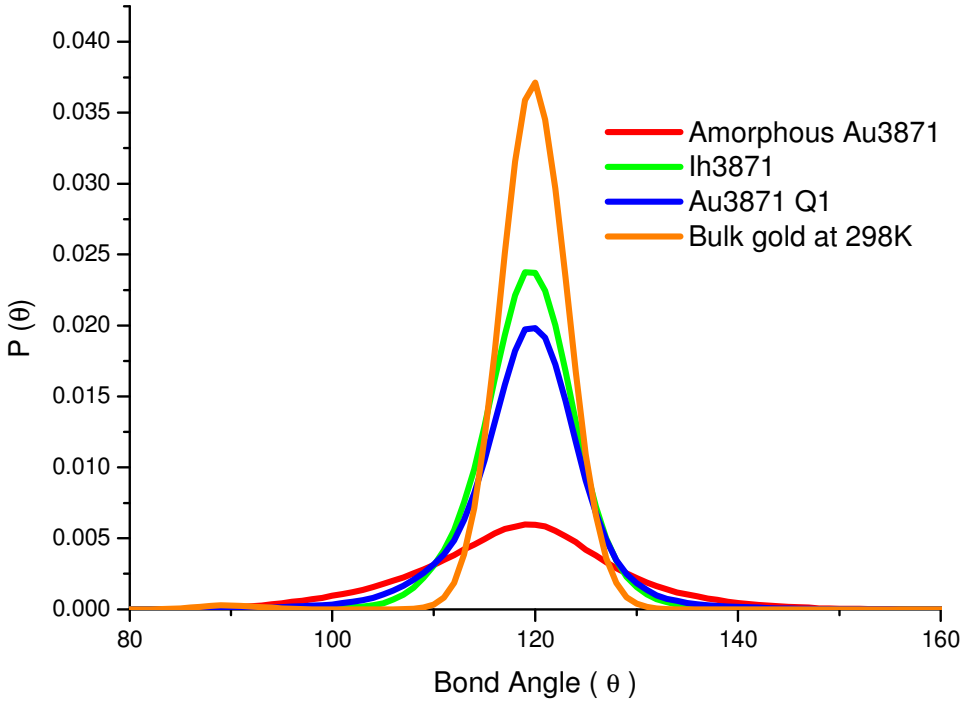


**Figure 3.31** The 6-membered ring (type 1) contribution to the bond angle distribution of Au3871 nanoclusters of different morphologies at 298K.

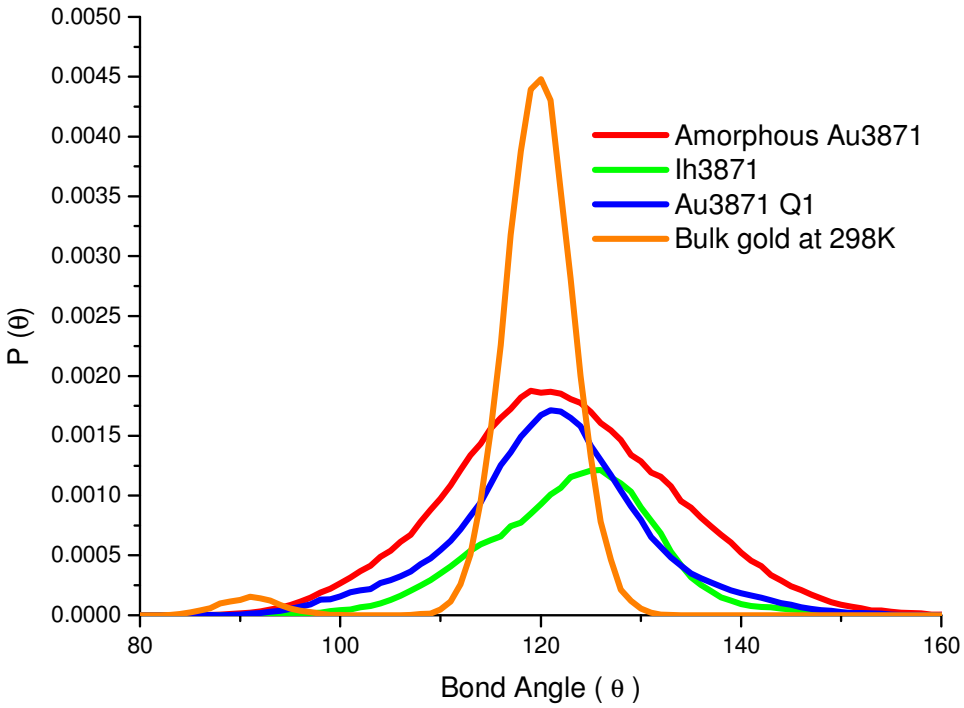


**Figure 3.32** The 6-membered ring (type 2) contribution to the bond angle distribution of Au3871 nanoclusters of different morphologies at 298K.

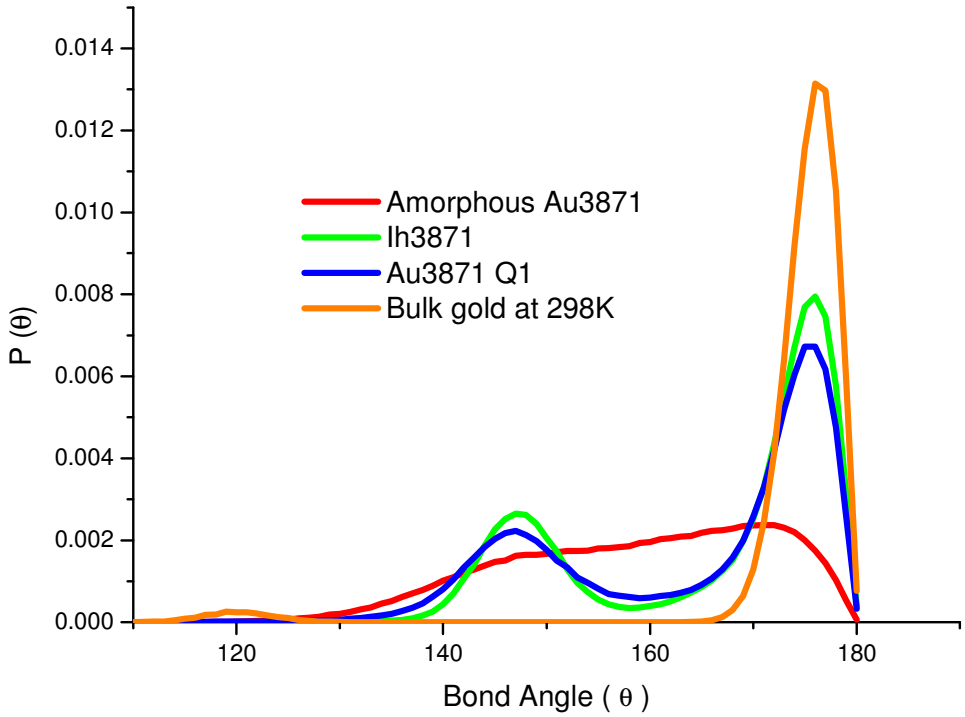


**Figure 3.33** The 6-membered ring (type 3) contribution to the bond angle distribution of Au3871 nanoclusters of different morphologies at 298K.

## 3.5 Shortest-path (SP) ring analysis

The SP-ring statistics of the Au923 and Au3871 nanoclusters of different morphologies and comparison of different sizes of gold nanoclusters are shown in Figures 3.34-3.36. First, in Figure 3.34 and 3.35 we can see that the pattern of SP-ring statistics of Au923 and Au3871 nanoclusters are similar. There is a good agreement in the populations of different SP rings between perfect icosahedral and thermally annealed nanoclusters. For the amorphous nanocluster, the populations of SP rings are also close to that of icosahedral and thermally annealed nanoclusters, except for the 5-membered rings. The population of 5-membered rings in the amorphous nanocluster is significantly higher than that in the other two morphologies. Obviously, the formation of 5-membered rings in a nanocluster

relates to the structural disorder. Compared to the nanocluster, the perfect bulk FCC crystal has no population of 5-membered rings. On the other hand, in Figure 3.36 the comparison between the gold nanoclusters of different sizes shows a smooth trend in the populations of different SP member rings. The populations of 3-, 4- and 6-membered rings increase with the nanocluster sizes, while the population of 5-membered rings decreases. The trends indicate that the nanoclusters become more and more crystalline when the size increases.

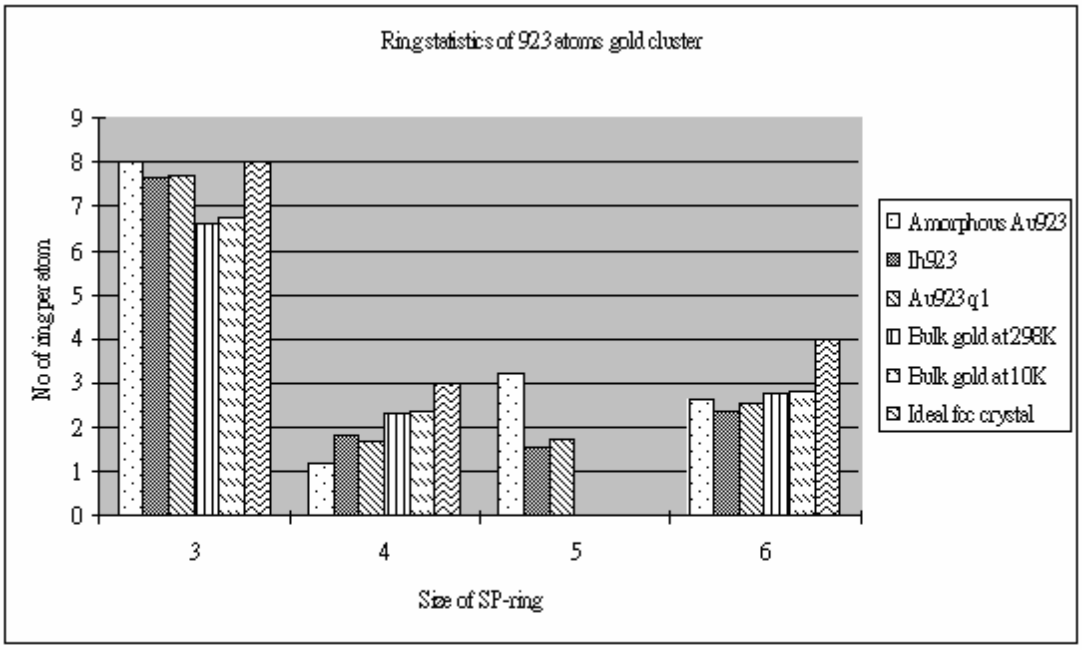


**Figure 3.34** A comparison of ring statistics of Au923 nanocluster of different morphologies with that of bulk gold at finite temperatures and ideal bulk fcc crystal.

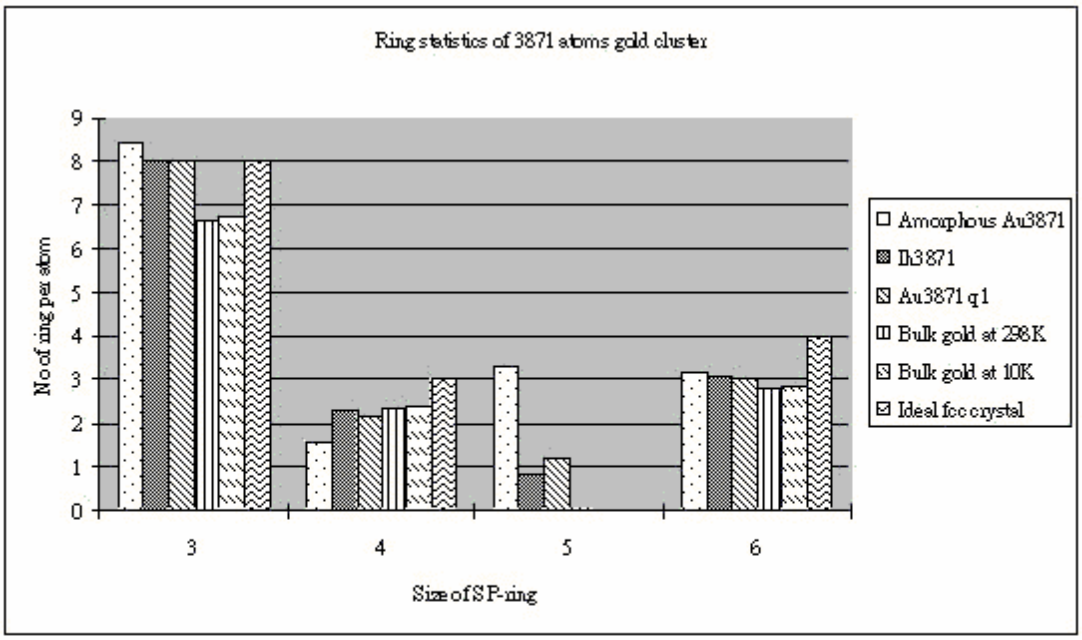


**Figure 3.35** A comparison of ring statistics of Au3871nanocluster of different morphologies with that of bulk gold at finite temperatures and ideal bulk fcc crystal.

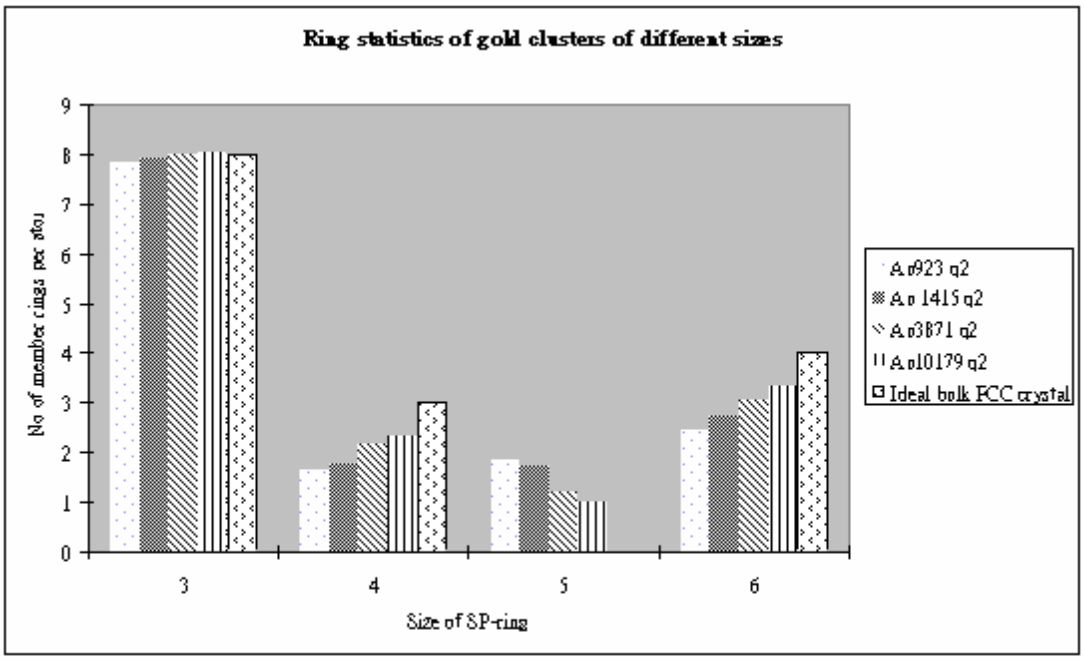


**Figure 3.36** A comparison of ring statistics of thermally annealed (Q2) gold nanocluster of different sizes with that of ideal bulk fcc crystal.

# References

[1] W. H. Li, S. Y. Wu, C. C. Yang, S. K. Lai, K. C. Lee, H. L. Huang and H. D. Yang, Phys. Rev. Lett. **89**, 135504 (2002).

[2] W. Vogel, J. Bradley, O. Vollmer and I. Abraham, J. Phys. Chem. B **102**, 10853 (1998).

[3] A. Pinto, A. R. Pennisi, G. Faraci, G.. D'Agostino, S. Mobilio and F. Boscherini, Phys. Rev. B **51**, 5315 (1995).

[4] R. Jin, S. Egusa and N. F. Scherer, J. Am. Chem. Soc. **126**, 9900 (2004).

[5] Y. Y. Yu, S. S. Chang. C. L. Lee and C. R. Wang, J. Phys. Chem. B **101**, 6661 (1997).

[6] S. S. Shankar, A. Rai, B. Ankamwar, A. Singh, A. Ahmad and M. Sastry, Nat. Mater. 482 (2004).

[7] Y. Sun and Y. Xia, Adv. Mater. **15**, 695 (2003).

[8] Y. Sun and Y. Xia, Science **298**, 2176 (2002).

[9] J. Hu, Y. Zhang, B. Liu, J. Liu, H. Zhou, Y. Xu, Y. Jiang, Z. Yang and Z-Q Tian, J. Am. Chem. Soc. **126**, 9470 (2004).

[10] I.L. Garzon et.al. Phys. Rev. Lett. **81**, 1600 (1998).

[11] Nam, H.S., Hwang, N. M., Yu, B. D. & Yoon, J. –K., Phys. Rev. Lett., 89, 275502 (2002).

[12] Y. G. Chushak and L. S. Bartell, J. Phys. Chem. B **105**, 11605 (2001).

[13] J.-H. Shim, S. C. Lee, B.-J. Lee, Jin-Yoo Suh and Y. W. Cho, J. Cryst. Growth **250**, 558 (2003).

[14] W. Krakow, M. J. Yacaman and L. Aragon, Phys. Rev. B **49** 10591 (1994).

[15] Y. Qi, T. Cagin, Y. Kimura and W. A. Goddard III, Phys. Rev. B **59**, 3527 (1999).

[16] J. L. Rodríguez-López, J. M. Montejano-Carrizales and M. José-Yacamán, Mod. Phys. Lett. B **20**, 725-751 (2006).

[17] K. Koga and K.Sugawara, Surf. Sci. **529**, 23 (2003).

[18] K. Koga, T. Ikeshoji and K.Sugawara, Phys. Rev. Lett. **92**, 115507 (2004).

[19] F. Ercolessi, M. Parrinello and E. Tosatti, Philos. Mag. A **58**, 213 (1988).

[20] C. L. Cleveland, W. D. Luedtke and U. Landman, Phys. Rev. Lett. **81** 2036 (1998).

[21] B. O'Malley, Ph.D. thesis (RMIT) (2001)

(Available at http://mams.rmit.edu.au/6g0wr8cwl4b1.pdf); B. O'Malley and I. Snook,

J. Chem. Phys.**123**, 5, 054511 (2005).

# Chapter 4

# Thermodynamics of Gold Nanostructures

Since multiple shape synthesis of gold nanoclusters is possible [1, 2], an important question regarding these nanoclusters is: does the higher stability of a gold nanocluster with particular shape and structure cause a higher possibility of occurrence? Recently, experimental population statistics of gold nanoclusters with different structural morphologies and sizes was conducted to investigate this point [3, 4]. These studies showed that the FCC crystalline structure, which has a higher energetic stability in many theoretical and experimental studies, is almost absent in a population of gold nanoparticles smaller than 10 nm in diameter. Instead, icosahedral clusters were dominant in the population, until the cluster size is larger than 12 nm in diameter. Such studies give new insight into the understanding of gold nanoparticle formation and stability.

Many of the theoretical studies of gold nanoclusters have focused on calculating the total internal (or configurational) energy of the cluster as a means of assessing relative stability. In this study we compare the configurational energy with an estimate of the cluster free energy as a means of predicting thermodynamic stability. In this chapter, we present the results of a molecular dynamics (MD) study of gold nanoclusters of different sizes and structural morphologies modeled by the Glue potential. As outlined in section 3.1, the clusters were cooled from the melt, and then structurally relaxed at room temperature. Once equilibrated, the internal energy, vibrational entropy and free energy of each cluster was calculated.

## 4.1 Velocity autocorrelation function (VACF) and vibrational density of state (VDOS)

In order to estimate the entropies and free energies of gold nanoclusters, we calculate the velocity autocorrelation function (VACF) and then vibrational density of states (VDOS), as described in section 2.5. Figure 4.1 shows a comparison of the VACFs for the icosahedral, amorphous and thermally annealed 3871 atoms gold nanoclusters at 298K. In the VACF plot, it is clearly shown that the correlation of the particle velocity decays faster for the amorphous cluster, compared to the others. The VACFs of icosahedral and thermally annealed nanoclusters are very similar. This is probably due to the fact that these clusters have a similar internal structure at 298K.

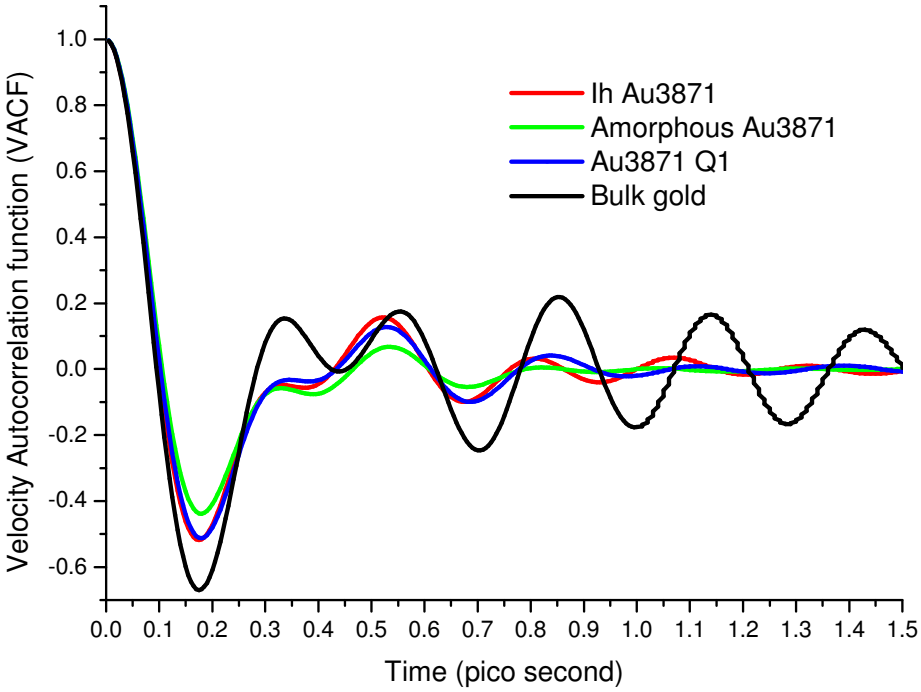


**Figure 4.1** The velocity autocorrelation function (VACF) of the icosahedral Au3871 cluster, the amorphous Au3871 cluster, the thermally annealed Au3871 (Q1) cluster and bulk gold.

Compared to bulk gold, the amplitudes and peak positions of oscillations of the gold nanoclusters are significantly different in Figure 4.1. This indicates that all the nanoclusters still have internal cores which are far from being 'bulk like' in structure. For example, at 0.3 ps in the peak in the VACF of bulk gold is damped in the gold nanoclusters. The atom velocities in the bulk are also correlated out to much longer times than for the nanoclusters.

In order to assess the effect of morphology on the VDOS, we also calculated the VDOS for the icosahedral, Q1 and Q2 thermally annealed and amorphous nanoclusters for our largest cluster size, 10179 atoms. This is shown in Figure 4.2 along with VDOS of bulk gold. In the VDOS, we find that the density of states distribution of the icosahedral and Q1 and Q2 thermally annealed nanoclusters are similar in the low frequency region (< 3 THz). The peak in the VDOS for the thermally annealed nanoclusters is slightly shifted to a lower frequency compared to the icosahedral nanocluster above 3 THz. This shift is probably due to the difference in internal structure between the icosahedral and thermally annealed nanoclusters. For the VDOS of the amorphous nanocluster, the whole density of states distribution is more diffuse compared to that of the icosahedral and thermally annealed nanoclusters. Moreover, the amplitude of the peaks is relatively lower and less well defined than that for the other two motifs. The shift is probably caused by the lack of symmetry in the amorphous nanocluster, therefore correlation of vibrational motion is much less than that in the icosahedral and thermally annealed nanoclusters. As the difference between the vibrational motion of the internal and surface atoms is smaller due to the largely amorphous environment, the peaks in the low and high frequency region would be less well defined and lower in amplitude.

Finally we note that for bulk gold the VDOS distribution begins just after 1 THz and goes to zero sharply just below 4 THz while the frequency range of the VDOS

for all the nanoclusters is from 0 THz to nearly 5THz. The relative low -(0-1 THz) and high-frequency (4-5 THz) modes in nanoclusters probably originate from the broadening and shifting in the peaks in the radial distribution function [5, 6]. Shorter interatomic distances compared to that in the bulk system give rise to elastic stiffening (or higher phonon frequency), while larger interatomic distances cause elastic (or phonon) softening [5-7].

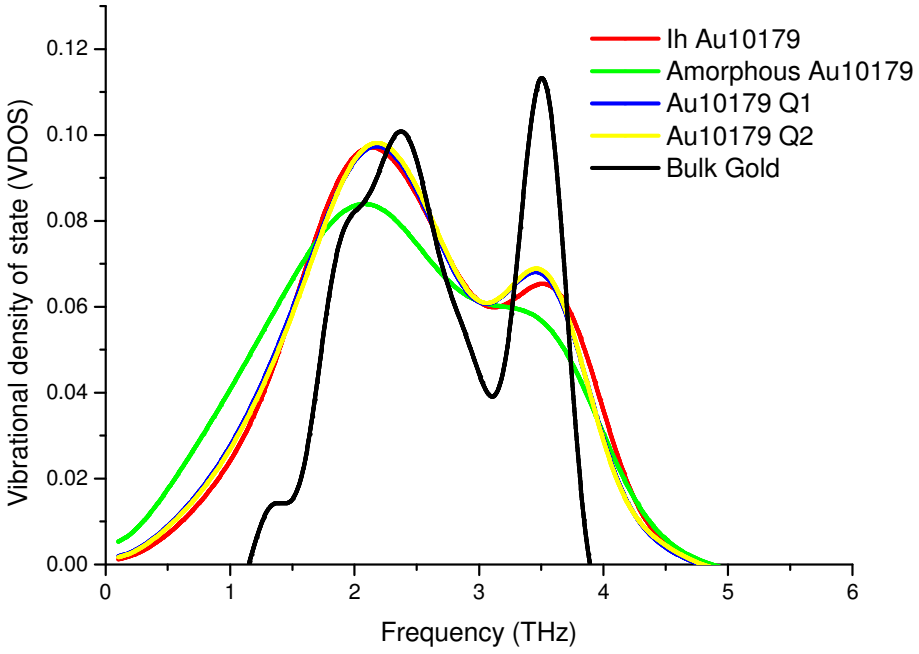


**Figure 4.2** A comparison of VDOS between the 10179 atom gold nanoclusters and bulk gold.

Figure 4.3 shows comparison between the VDOS of icosahedral gold nanoclusters of different sizes. This reveals a number of trends as the nanocluster size increases, namely:

(i) The high frequency peak becomes less diffuse, the amplitude of the peak maxima increases and shifts to a lower frequency closer to that of bulk gold.

(ii) The lower frequency peak maxima also increases in amplitude with the frequency shifting closer to the value for bulk gold.

(iii) The upper bound frequency at which the VDOS goes to zero decreases, shifting towards the cutoff for bulk gold.

These trends obviously indicate the cluster cores becoming more 'bulk' like as the cluster size increases.

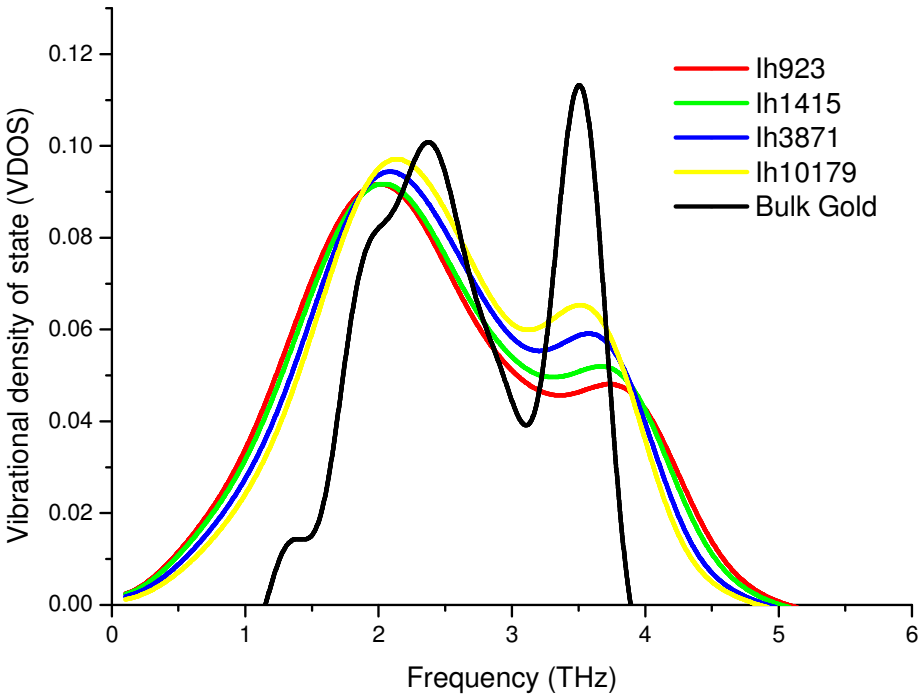


**Figure 4.3** The size dependence on VDOS: Comparison between the icosahedral 923 atom, 1415 atom, 3871 atom and 10179 atom gold nanoclusters.

We compare the VDOS of bulk FCC (111) surface, bulk FCC gold and icosahedral 10179 atoms gold nanoparticle surface, as shown in Fig 4.4. Generally, compared to nanoparticle surface the bulk (111) surface has a similar vibrational frequency distribution. The positions of two lower frequency peaks are very close, while the upper bound frequency of bulk (111) surface at which the VDOS goes to zero decreases, shifting towards the cutoff for bulk FCC gold. Also, the amplitude of the lower frequency peak maxima of the bulk gold surface is higher than that of the nanoparticle surface. Finally, in the higher frequency region of bulk gold, we found there are two small peaks at around 3 and 3.75 THz respectively. This comparison further indicates that the surface gold atoms vibrate at a lower frequency, and the vibrational behaviour of the atoms in nanoparticle surface is similar to that of bulk surface atoms.

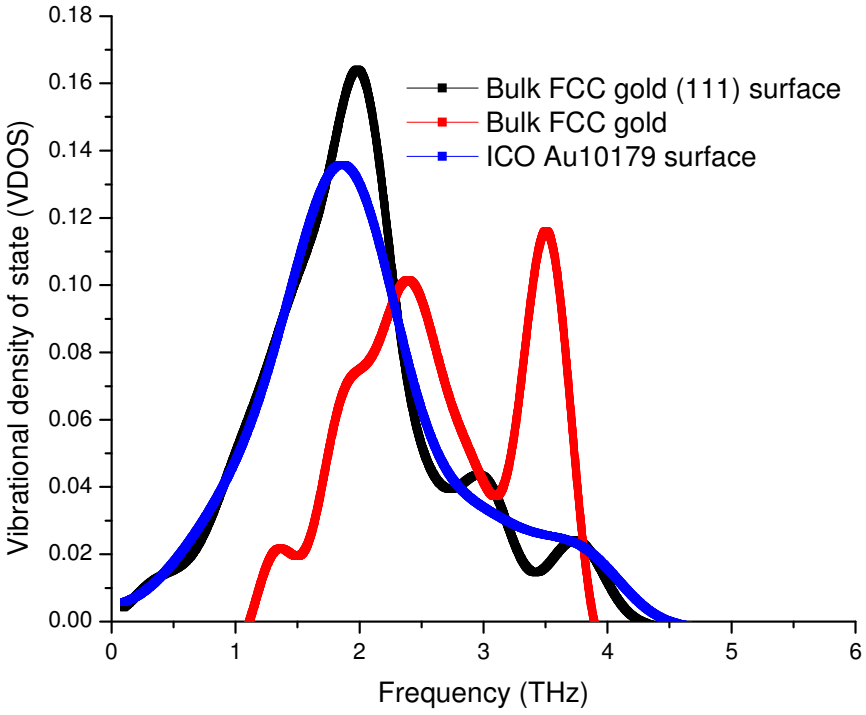


**Figure 4.4** A comparison of VDOS between bulk FCC gold (111) surface, bulk FCC gold and the 10179 atom gold nanocluster surface.

Furthermore, we make a comparison between the VDOS of bulk FCC and HCP, as shown in Fig 4.5. Generally, the bulk HCP has a boarder frequency distribution of VDOS than bulk FCC does. The amplitudes of both lower and higher frequency peak maxima of bulk HCP are higher than that of bulk FCC, and the whole set of peaks and valley between peaks of bulk HCP shifts upwards. On the other hand, the positions of higher frequency peaks of bulk FCC and HCP are close, while the lower frequency peak of bulk HCP is shifted to the left hand side (low frequency region). We believe the difference between the VDOS of bulk HCP and FCC shown here partly explains the difference observed in the VDOS of the icosahedral gold nanoparticles and bulk gold, provided that there is HCP content inside the icosahedral gold nanoparticles.

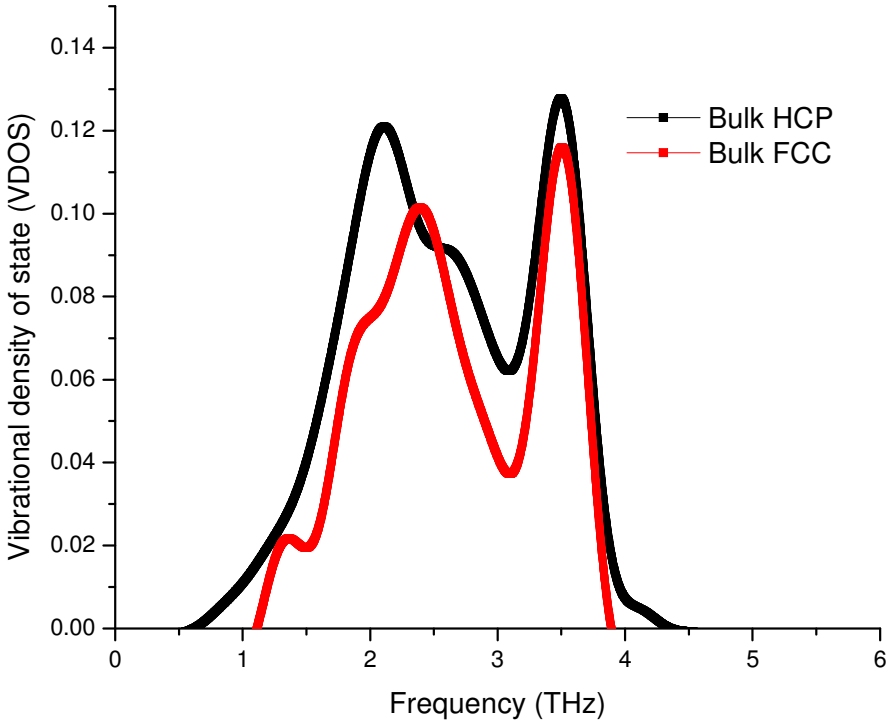


**Figure 4.5** A comparison of VDOS between bulk HCP gold and bulk FCC gold .

## 4.2 Potential energies, vibrational entropies and free energies

In considering the stability of the various nanoclusters we estimated the Gibbs free energy (Section 2.5) of the clusters. Table 4.1 gives the calculated internal energies, vibrational entropies and free energies of the perfect icosahedral, amorphous and quenched (or thermally-annealed) icosahedral-like nanoclusters investigated in this study. From the table, we find several interesting trends: Firstly, for all cluster sizes the amorphous clusters have the highest internal energy, highest vibrational entropy and highest free energy and are uniformly the least thermodynamically stable cluster configuration.

| Cluster | Internal energy(U) (eV/atom) | Entropy (S) ($10^{-4}$eV$^{-}$K/atom) | TS (eV/atom) | Free energy (eV/atom) |
|---|---|---|---|---|
| Ih 923 | -3.385 | 2.502 | 0.0746 | -3.460 |
| AMOR Au923 | -3.374 | 2.558 | 0.0762 | -3.450 |
| Au 923 Q1 | -3.404 | 2.534 | 0.0755 | -3.480 |
| Au 923 Q2 | -3.402 | 2.540 | 0.0757 | -3.478 |
| Au 923 Q3 | -3.404 | 2.530 | 0.0754 | -3.479 |
| Ih 1415 | -3.433 | 2.493 | 0.0743 | -3.508 |
| AMOR Au1415 | -3.415 | 2.555 | 0.0761 | -3.491 |
| Au 1415 Q1 | -3.445 | 2.511 | 0.0748 | -3.520 |
| Au 1415 Q2 | -3.448 | 2.525 | 0.0752 | -3.523 |
| Au 1415 Q3 | -3.446 | 2.527 | 0.0753 | -3.521 |
| Ih 3871 | -3.518 | 2.475 | 0.0738 | -3.592 |
| AMOR Au3871 | -3.482 | 2.549 | 0.0760 | -3.558 |
| Au 3871 Q1 | -3.525 | 2.497 | 0.0744 | -3.600 |
| Au 3871 Q2 | -3.525 | 2.500 | 0.0745 | -3.600 |
| Au 3871 Q3 | -3.526 | 2.496 | 0.0744 | -3.601 |
| Ih 10179 | -3.577 | 2.460 | 0.0733 | -3.650 |
| AMOR Au10179 | -3.534 | 2.540 | 0.0757 | -3.609 |
| Au 10179 Q1 | -3.581 | 2.479 | 0.0739 | -3.655 |
| Au 10179 Q2 | -3.583 | 2.482 | 0.0740 | -3.657 |
| Au 10179 Q3 | -3.584 | 2.468 | 0.0735 | -3.658 |
| Bulk Au (Glue) [11] | -3.741 | 2.357 | 0.0702 | -3.811 |
| Bulk Au (DFT) [12] | - | 2.458 | - | - |

**Table 4.1** The internal energy, entropy and free energy of gold nanoclusters investigated in this study. Values for bulk gold calculated from the glue and ab-initio potentials are also included. AMOR refers to the Amorphous clusters, Q1 : quenched nanocluster with the cooling rate = $2x10^{-11}$s/K, Q2 : quenched nanocluster with the cooling rate = $4x10^{-11}$s/K, Q3 : quenched nanocluster with the cooling rate = $6x10^{-11}$s/K.

Secondly, although the perfect icosahedral clusters have the lowest entropy (of all the cluster morphologies), their free energy is slightly higher than that for the Q1, Q2 and Q3 quenched icosahedral-like clusters, for all cluster sizes, effectively due to the difference in their internal energy contributions. If the growth of gold

nanoclusters is a thermodynamically driven process, at equilibrium the quenched (thermally-annealed) icosahedral-like structures have the highest probability of formation, and these kinds of structures are clearly observed in experimental studies [3, 4].

In order to compare the contribution of vibrational entropy from the surface and non-surface atoms we calculated the percentage of vibrational entropy coming from the surface atoms for one of our cluster morphologies (the Q2 quenched clusters) and the results are given in Table 4.2.

| **Nanocluster** | **Percentage of surface atoms in a nanocluster (%)** | **Percentage of vibrational entropy coming from surface atoms (%)** |
|---|---|---|
| Au923 q2 | 43.77 | 46.06 |
| Au1415 q2 | 38.94 | 41.14 |
| Au3871 q2 | 29.19 | 31.01 |
| Au10179 q2 | 21.75 | 23.27 |

**Table 4.2** The relative percentage of vibrational entropy coming from the surface for the Q2 quenched nanoclusters.

The surface and non-surface contributions to the vibrational entropy were obtained by projecting out their respective contributions to the total vibrational density of states. As an example, Figure 4.4 shows the projected VDOS for the first 5 layers of the (Q1) quenched 10179 gold nanocluster. The figure clearly indicates that the major contribution to the low frequency peak in the VDOS spectrum is due to surface phonon vibrations while the higher frequency peak is mainly due to bulk-like phonons. Our VDOS results are consistent with those of Sun *et al.* [8] who have performed similar analysis on the surface and bulk VDOS for smaller gold nanoclusters. Using the same potential, Sun et al. calculated the vibrational density

of states (VDOS) for the surface shell, transitional shell and core (bulk-like) region of gold nanoclusters with less than 1000 atoms. Due to the different definition for the spatial regions inside the nanocluster analyzed in our study and that of Sun et al., it is difficult to make direct quantitative comparison. But generally we found there is a good agreement between the result by Sun et al. and our VDOS results in Figure 4.4.

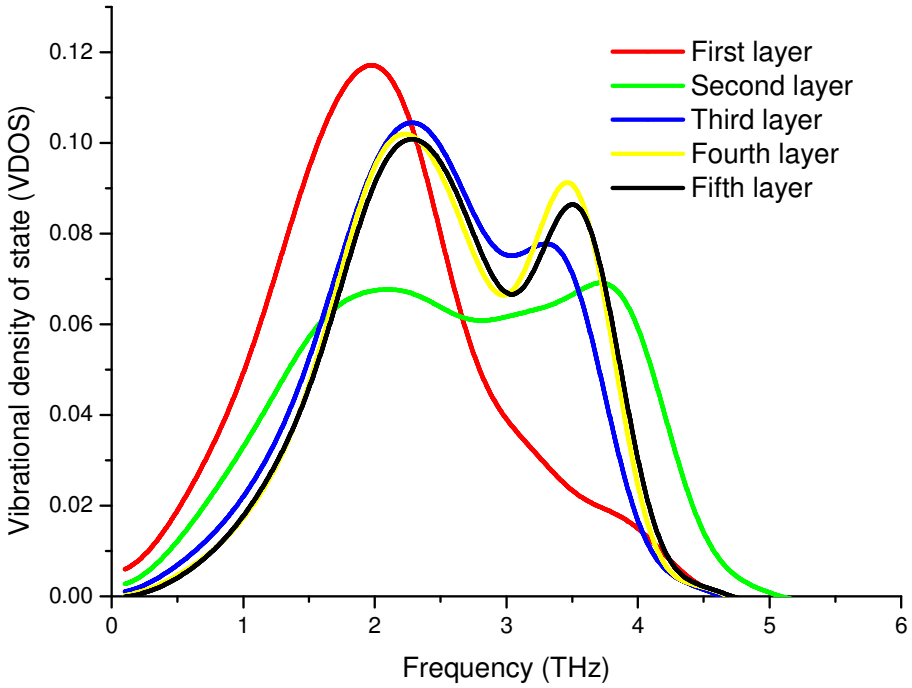


**Figure 4.6** The partial VDOS of different zones in a thermally annealed (Q1) 10179 atoms gold nanocluster.

The distribution and peak positions of VDOS of different regions (surface, interface and core regions) match with each other. The main quantitative difference is the frequency range of the VDOS. In our VDOS of gold nanoclusters, the frequency range of surface shell is narrower and the high frequency tail is shorter compared to that of Sun et al..

On the other hand, there is one qualitative difference between Sun *et al.*'s and our result. For the surface layer, the low frequency mode dominates in the distribution, while both high and low frequencies exist in core (or bulk-like) region. In between the surface and core regions, the second outermost atomic layer exhibits transitional behavior. The peak height and width of the low and high frequency modes are almost identical. It shows that both low and high frequency vibrational behavior co-exists in interfacial layer of the gold nanocluster, without either dominating. The raising of the high frequency peak and depression of the low frequency peak in the interfacial region indicates the significant change of vibrational behavior from surface to core. This novel vibrational behavior in the interfacial layer and also the clear transition from surface to core region of the gold nanocluster were not observed in Sun *et al.*'s result.

In Table 4.3, we compare the vibrational entropy coming from the surface atoms of perfect, and Q2 quenched, icosahedral clusters. We find that the surface disorder in the Q2 quenched nanoclusters results in lower vibrational entropy, compared to that of the perfect Ih nanoclusters. The disorder may help to reduce the surface strain of large icosahedral nanocluster and stabilize the surface. Our findings here also agree with the fact that ideal icosahedral clusters consist of 20 (111) planes and surface reconstruction of (111) gold surfaces has been found to be energetically favorable from both experimental [9] and theoretical studies [10].

| Nanocluster | Entropy coming from the surface atoms in Ih nanocluster ($S_{Ih}$) ($10^{-4}$ eV$^{-}$K/atom) | Entropy coming from the surface atoms in thermally annealed nanoclusters ($S_{Q2}$) ($10^{-4}$ eV$^{-}$K/atom) | Entropy difference ($S_{Q2}$ - $S_{Ih}$) ($10^{-4}$ eV$^{-}$K/atom) |
|---|---|---|---|
| Au923 | 2.68448 | 2.66562 | -0.01886 |
| Au1415 | 2.67522 | 2.66431 | -0.01091 |
| Au3871 | 2.67841 | 2.65535 | -0.02306 |
| Au10179 | 2.66558 | 2.65674 | -0.00884 |

**Table 4.3** A comparison of the vibrational entropy coming from the surface atoms of the perfect icosahedral (Ih) clusters and the Q2 quenched clusters.

In this chapter, we predicted the thermal annealed icosahedral structures as the most thermodynamically stable structure for the gold nanoparticles consisting of 923-10179 atoms. We also found that the contribution from the vibrational entropy to the total free energy is much smaller compared to the potential energy. The thermal annealing process caused a reconstructed (imperfect) icosahedral structure with more negative potential energy. On the other hand, we found the novel vibrational behaviour of transitional atomic layer in the gold nanoparticles, which has not been reported before. The coexistence of low and high frequencies in transitional layer may arise due to the coupling of vibrational modes of surface and core atoms. We believe this is the first step for us to understand the atomic dynamics inside a nanoparticle at finite temperature.

Due to the limitation of the computational time, we did not simulate the gold nanoparticles beyond 10179 atoms, which were observed from the HRTEM experiment by Koga et al. Simulating larger gold nanoparticles will be feasible while using a parallelized MD program in the future. Also, we did not calculate the vibrational entropy and free energy of the gold nanoparticles of the same range of sizes modeled by Force-Matching potential. In the future, the thermodynamics of

gold nanoparticles modeled by Force-Matching potential can be calculated and compared to the results from Glue potential and also experimental observations.

# References

[1] F. Kim, S. Connor, H. Song, T. Kuykendall and P. Yang, Angew. Chem. Int. Ed. **43**, 3673 (2004).

[2] T. K. Sau and C. J. Murphy, J. Am. Chem. Soc.**126**, 8648 (2004).

[3] K. Koga and K.Sugawara, Surf. Sci. **529**, 23 (2003).

[4] K. Koga, T. Ikeshoji and K.Sugawara, Phys. Rev. Lett. **92**, 115507 (2004).

[5] D.Wolf, J. Wang, S. R. Phillpot and H. Gleiter, Phys. Rev. Lett. **74**, 4686 (1995).

[6] D.Wolf and J. Lutsko, Phys. Rev. Lett. **60**, 1170 (1988).

[7] D. Wolf and J. Jaszczak, J. Comp. –Aided Mat. Design **1**, 111 (1993).

[8] D. X. Sun, X. G. Gong and X. Q. Wang, Phys. Rev. B **63**, 193412 (2001).

[9] U. Harten, A. M. Lahee, J. P. Toennies and Ch. Wöll., Phys. Rev. Lett., **54**, 2619 (1985).

[10] A. Bartolini, F. Ercolessi and E. Tosatti, *The Structure of Surfaces II*, edited by J. F. van der Veen and M. A. Van Hove, Springer-Verlag, Berlin (1988), p.132.

[11] F. Ercolessi, M. Parrinello and E. Tosatti, *Philos. Mag. A* **58**, 213 (1988).

[12] Ph.D. Thesis, E. J. Wu, Massachusetts Institute of Technology (2002). Available at http://burgaz.mit.edu/PUBLICATIONS/theses.php

# Chapter 5

# Crystallization of Gold Nanostructures

Theoretical studies of the crystallization of small gold nanoparticles (<1000 atoms) have revealed two important points regarding their growth (1) the Ih morphology constitute a local minima in the cluster free energy [1] and (2) crystallization appears to initiate from the surface and proceed into the cluster core [2,3].

However the crystallization dynamics of large gold nanoparticles (> 3nm) is still unknown. Koga et.al. [4] comment "the large abundance of big Ih over several nanometers cannot be understood by the energetics." Therefore here, we study the kinetics of the crystallization process of a 10179 atom (~8nm in diameter) icosahedral gold nanoparticle which is quenched from the melt by a combination of MD simulation and analysis of the local structure using our new topological method based on planar graphs [3,5,6]. Using this topological analysis method we can determine whether the local packing of the nanocluster core is face centered cubic (FCC), hexagonal cubic packed (HCP), defected FCC or defected HCP and follow the growth or rearrangement of FCC fragments and HCP planes in the core as a function of temperature.

## 5.1 Analyzing crystallization of the nanostructure: the case of Au10179 nanocluster modeled by the Glue potential

As discussed earlier in this thesis, the Embedded atom "glue" potential was used to model the atomic interactions, as this potential has been shown to effectively reproduce the bulk, surface and defect properties of gold [7]. The quenched icosahedral clusters were produced by melting the perfect icosahedral clusters (to 1400K) which were generated by an icosahedron generation program [8]. Once in the liquid state; the liquid gold clusters were quenched from 1400K to 1000K using a cooling rate of $2x10^{-11}$ Sec/Kelvin (s/K) and from 1000K to 298K with a cooling rate of $1x10^{-10}$ Sec/Kelvin (s/K). At each temperature structures were evolved as a function of time out to 0.4ns. The MD time step was 5fs.

An often used geometric measure for crystallization is the Q6 order parameter (Section 2.4.6) which measures the orientational order of an atomic system [5]. Figure 5.1 gives a plot of the Q6 order parameter with temperature for the gold nanoparticles quenched during the MD simulations from 1100 K to 298 K. The order parameter was calculated after running for 0.4ns at that particular temperature. The plot indicates a significant structural ordering occurring between 952 K and 940 K. In Figure 5.2 we give the results of other structural measures of crystallization over the temperature range 952K-298K.

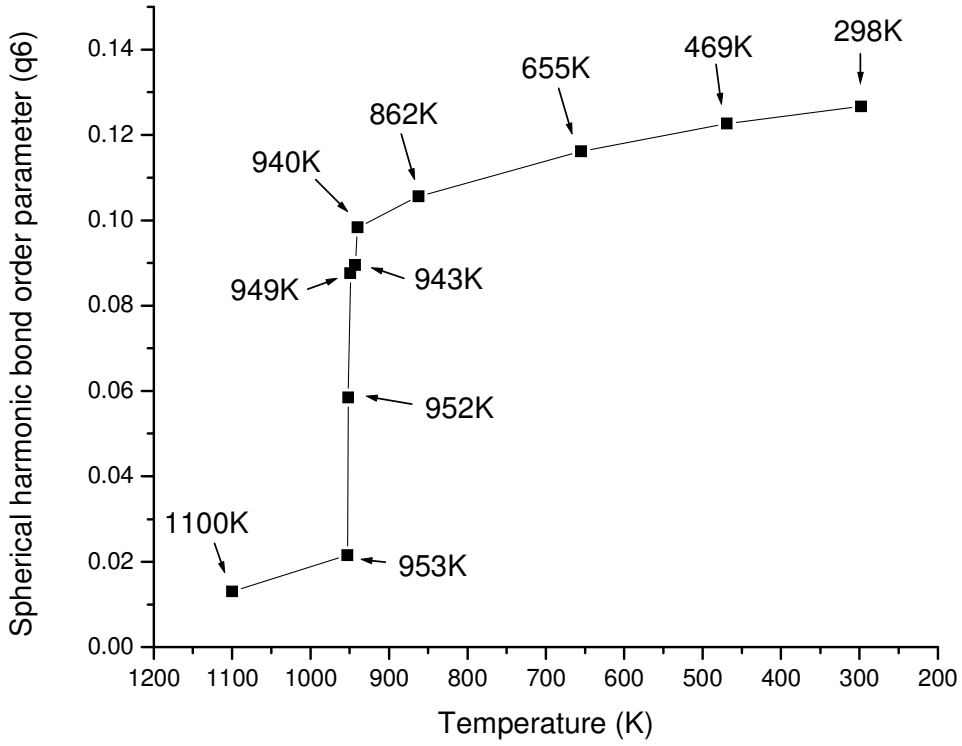


**Figure 5.1** (a) The variation of bond order parameter (Q6) during the quenching of an Au 10179 nanoparticle. The sharp rise of Q6 indicates the rapid crystallization occurs between 952K and 940K.

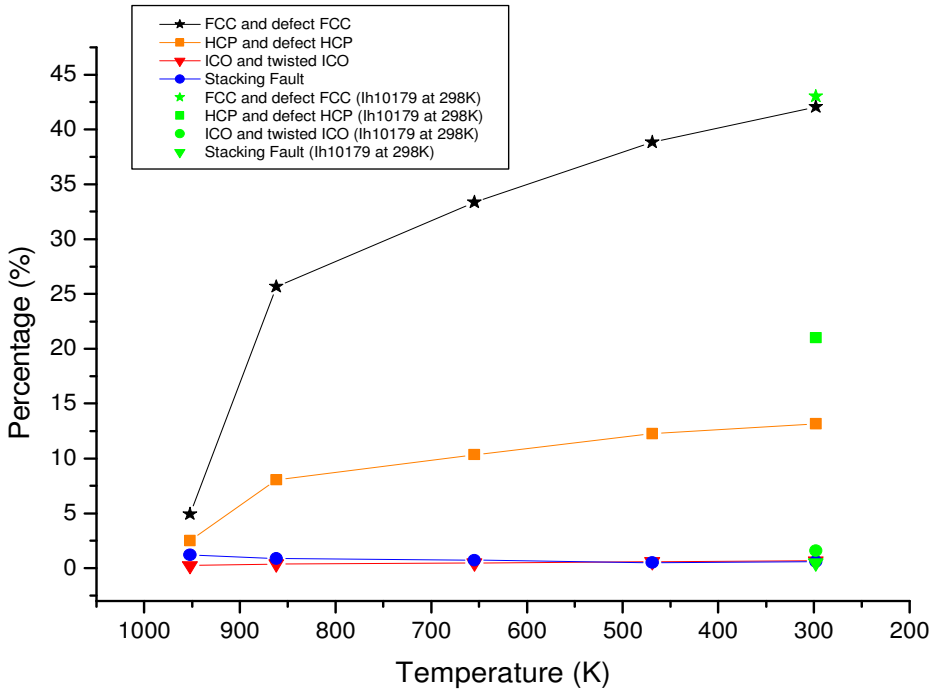


**Figure 5.2** The percentage variation of FCC, HCP, ICO (Icosahedral) and stacking fault content in an Au10179 nanoparticle during the quench.

These measures are based on calculating ring sequences about each atom [6] (section 2.4.2). The figure indicates that in quenching to 298 K the nanoparticle transforms from the disordered state to one consistent with an icosahedral structure, with large structural changes occurring between 952 K and 862 K. Figure 5.3 shows the radial distribution function of a nanoparticle at the corresponding temperatures in figure 5.1. We found that the change of physical state of gold nanocluster starts at 952K and the peaks become more and more sharp and defined during the cooling process.

In order to directly observe this structural ordering process in the nanoparticle core we use our planar graph method (section 2.4.2) to characterize the local bonding structure of the core atoms. We are able to classify the local environment about

each atom using the following colour scheme; FCC (pink), defected FCC (blue), HCP (yellow) and defected HCP (red).

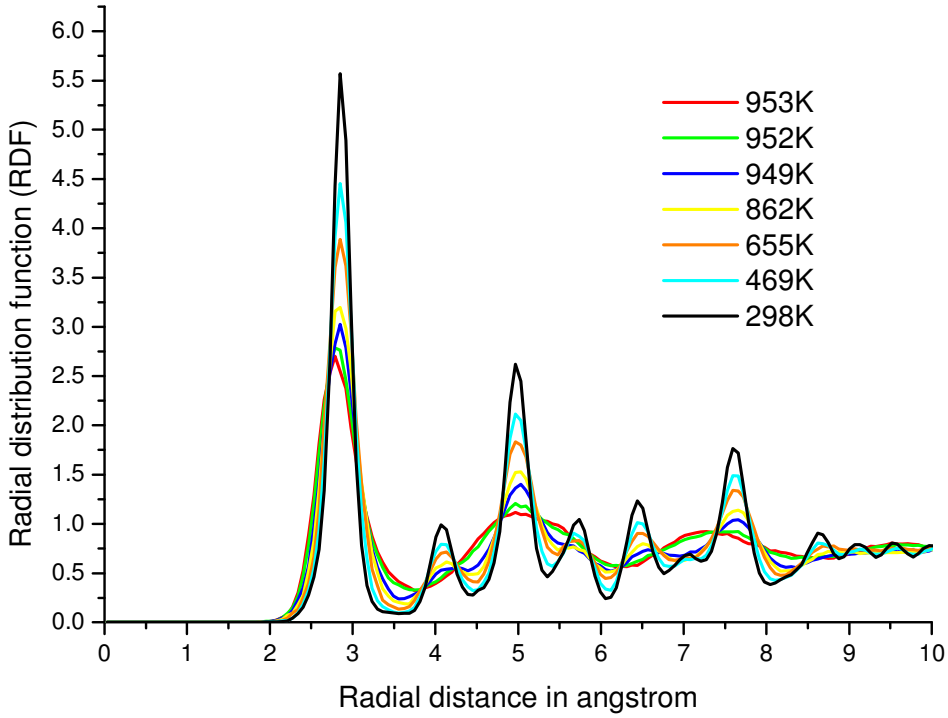


**Figure 5.3** The variation of radial distribution function of Au10179 nanoparticle during cooling process.

Figures 5.4-5.7 show snapshots of a typical gold nanoparticle at various time sequences during the evolution of the crystallization process at 949 K, which is a temperature at which large scale ordering is occurring based on Figures 5.1 and 5.2. Figures 5.4(a) and 5.4(b) shows the correlation between structural ordering occurring in the surface and core atoms after 20ps at 949 K. Figure 5.4(c), (d) and Figures 5.4(e), (f) are after 120 and 200 ps respectively. For the core atoms only atoms representing local FCC/defected FCC or HCP/defected HCP environments are represented.

## 20 ps

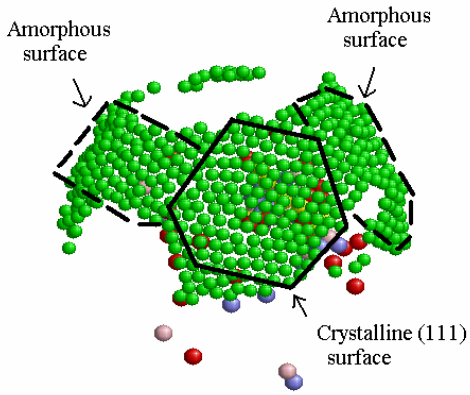


(A)

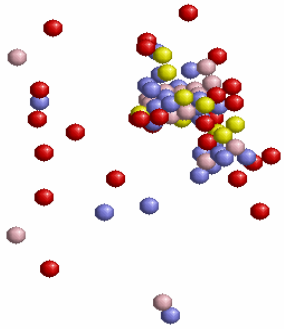

(B)

## 120 ps

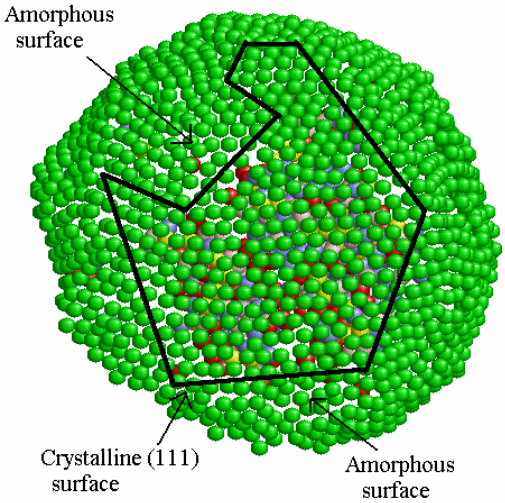


(C)

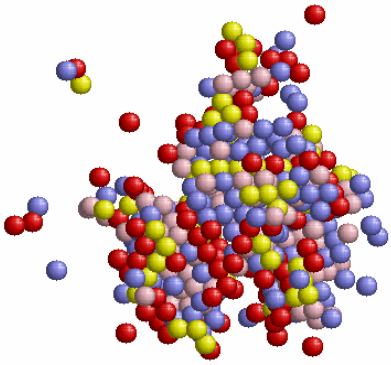

(D)

**Figure 5.4 is continued on the next page.**

## 200 ps

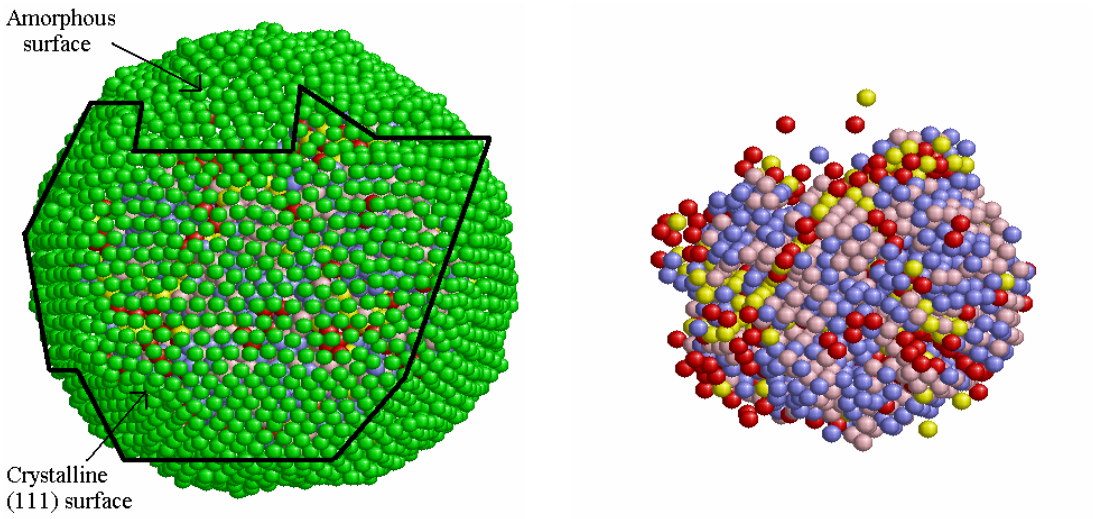


**(E)** **(F)**

**Figure 5.4** (a) and (b) The correlation between structural ordering occurring in the surface and core atoms after 20ps at 949 K; (c), (d) and (e), (f) are after 120 and 200 ps respectively. The following colour scheme is used to classify the core atoms, FCC (pink), defected FCC (blue), HCP (yellow), defected HCP (red) and surface atom (green).

The figure strongly suggests that ordering begins at the surface which precedes that of the core. For example at 20 ps, surface structural ordering is observed in the regions indicated by the black solid lines while very little evidence of ordering is found in the core. At 120ps and 200ps the crystalline regions of the core seem to lie directly below and inside that of the corresponding surface regions. From the evidence of our MD simulations, we suggest that the surface initiates a seed in the cluster core from which the core begins to crystallize. In order to trace out the early stage of crystallization, we analyze the structural evolution inside the gold nanoparticle cooled from 952K to 949K, as shown in figure 5.5. In figure 5.5, the nanocluster is at 949K (having been cooled from 952K) and the time-evolution of

crystallization is followed out to 200ps at that temperature by Molecular Dynamics. At 100ps, the small FCC fragments separated by a HCP plane appear inside the nanoparticle. At 160ps, the first, complete and five-fold symmetrical crystalline fragment is nearly formed.

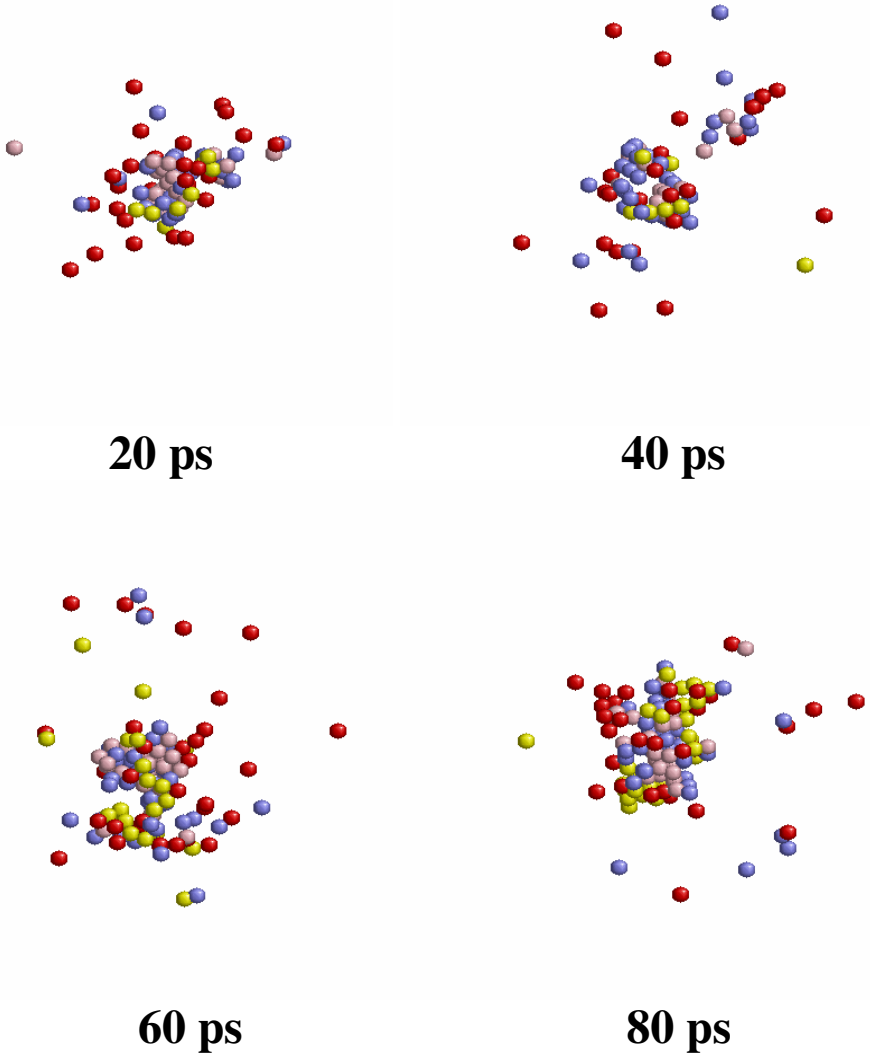


**Figure 5.5 is continued on the next page.**

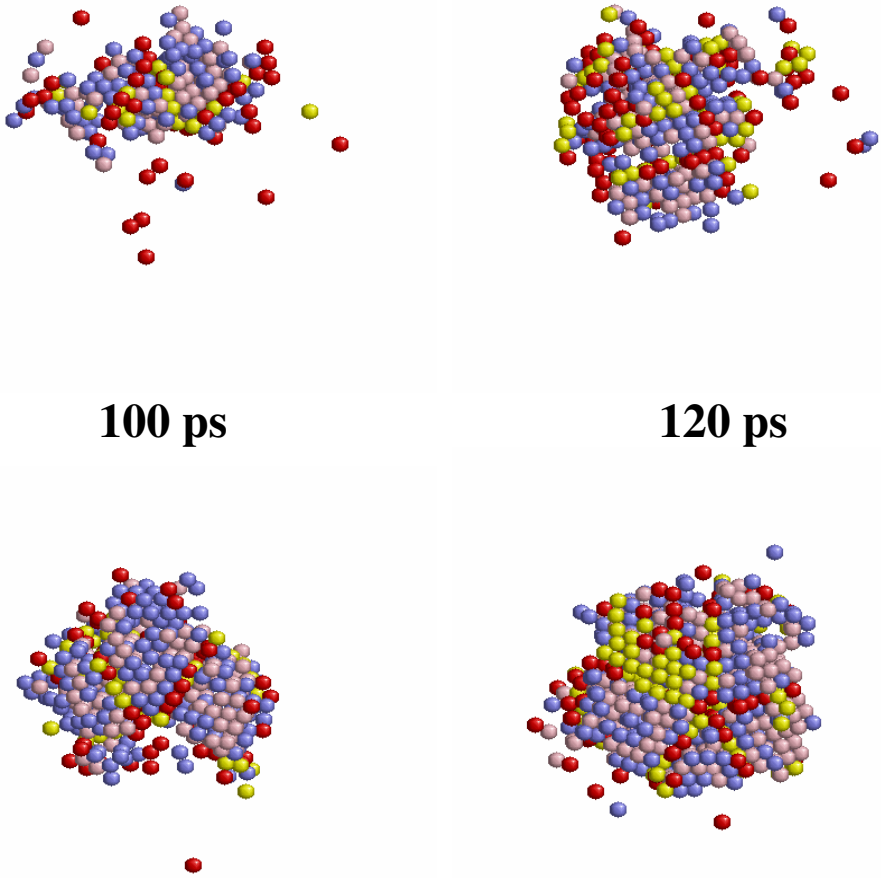

**100 ps** **120 ps**

**140 ps** **160 ps**

**Figure 5.5 is continued on the next page.**

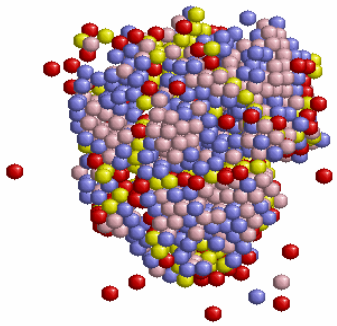

**180 ps**

**Figure 5.5** Snapshots in the time evolution of the core from 20ps to 180ps. The following colour scheme is used to classify the core atoms, FCC (pink), defected FCC (blue), HCP (yellow) and defected HCP (red).

We can also observe the time evolution of core crystallization at 949 K in Figure 5.6 which shows snapshots in the time evolution of the core corresponding to 160ps (Figures 5.6(a)), 180ps (Figures 5.6(b) and 5.6(c)) and 200ps (Figures 5.6(d)). In Figure 5.6(a) (160ps) we indicate the direction in which crystallization is preceding by red arrows and 20 ps later (Figure 5.6(b)) we observe that the atoms in the regions indicated by these arrows have transformed from a disordered state to one where the local environment is FCC or HCP. In Figure 5.6(b) we indicate (using yellow dotted lines) the regions where we believe FCC fragments or HCP planes are beginning to form. In Figure 5.6(c)(180 ps) we again indicate, using black dotted lines, regions where newly formed FCC fragments have formed at 200ps (Figure 5.6(d)).

At 949 K we can also observe the initial formation of a twin plane in the core of the gold nanoparticle after 200ps in the time evolution. Figure 5.7 shows the surface and core structure after 200ps but from 2 different visual perspectives. For

the surface atoms we show regions (black triangles) where sections of (111) planes meet at a line which we designate as a ‘twin line’, which may be a precursor to the twin plane of an icosahedral structure. In figure 5.7(c) and (d) one can observe the formation of a twin plane, indicated by an arrow, directly below the twin line at the surface.

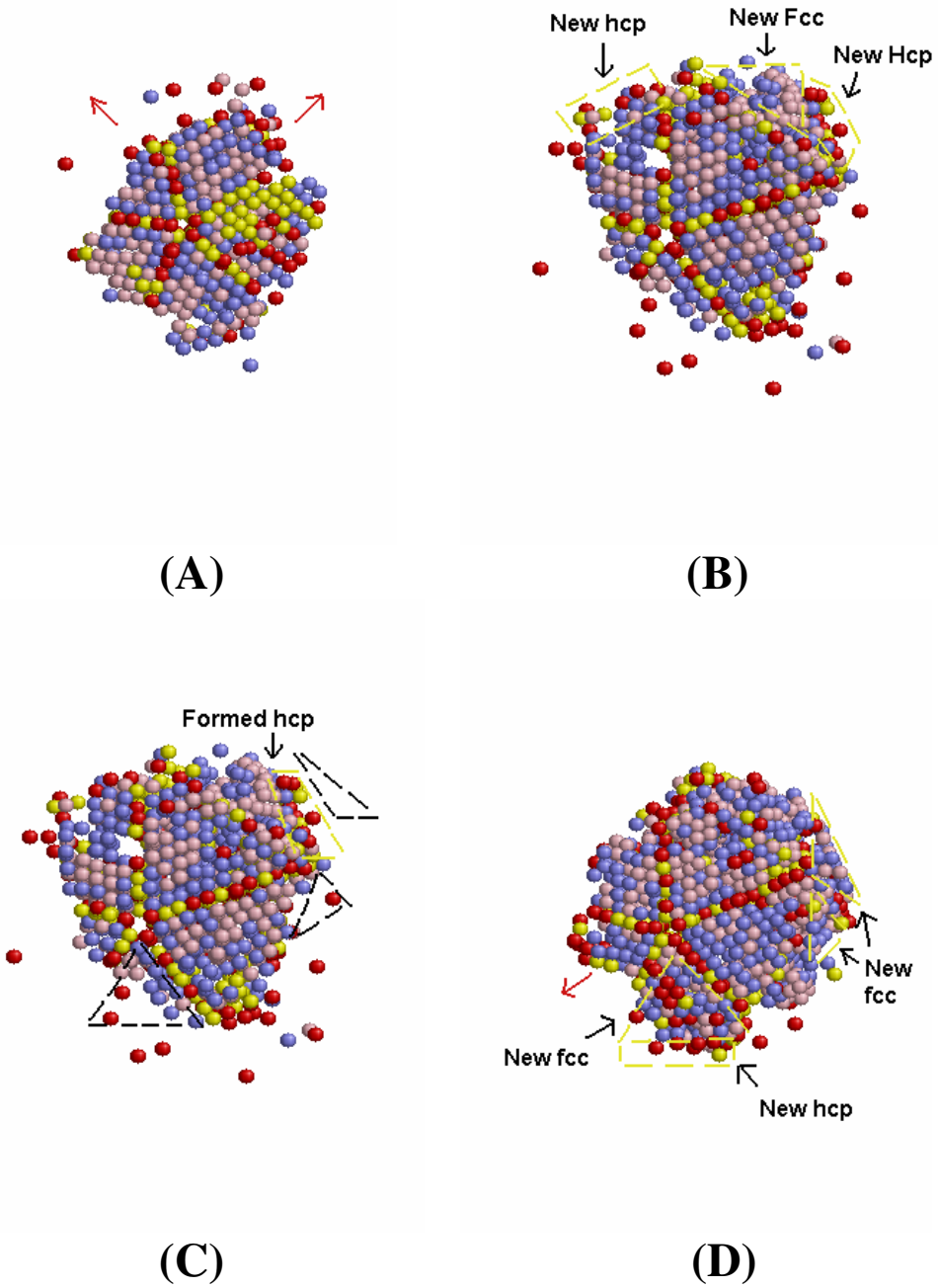


**Figure 5.6** Snapshots in the time evolution of the core at 160ps (3a), 180ps (3b and 3c) and 200ps (3d). The direction of crystallization is indicated by red arrows. The following colour scheme is used to classify the core atoms, FCC (pink), defected FCC (blue), HCP (yellow) and defected HCP (red). Yellow and dotted black lines represent the regions where we believe FCC fragments or HCP planes are beginning to form.

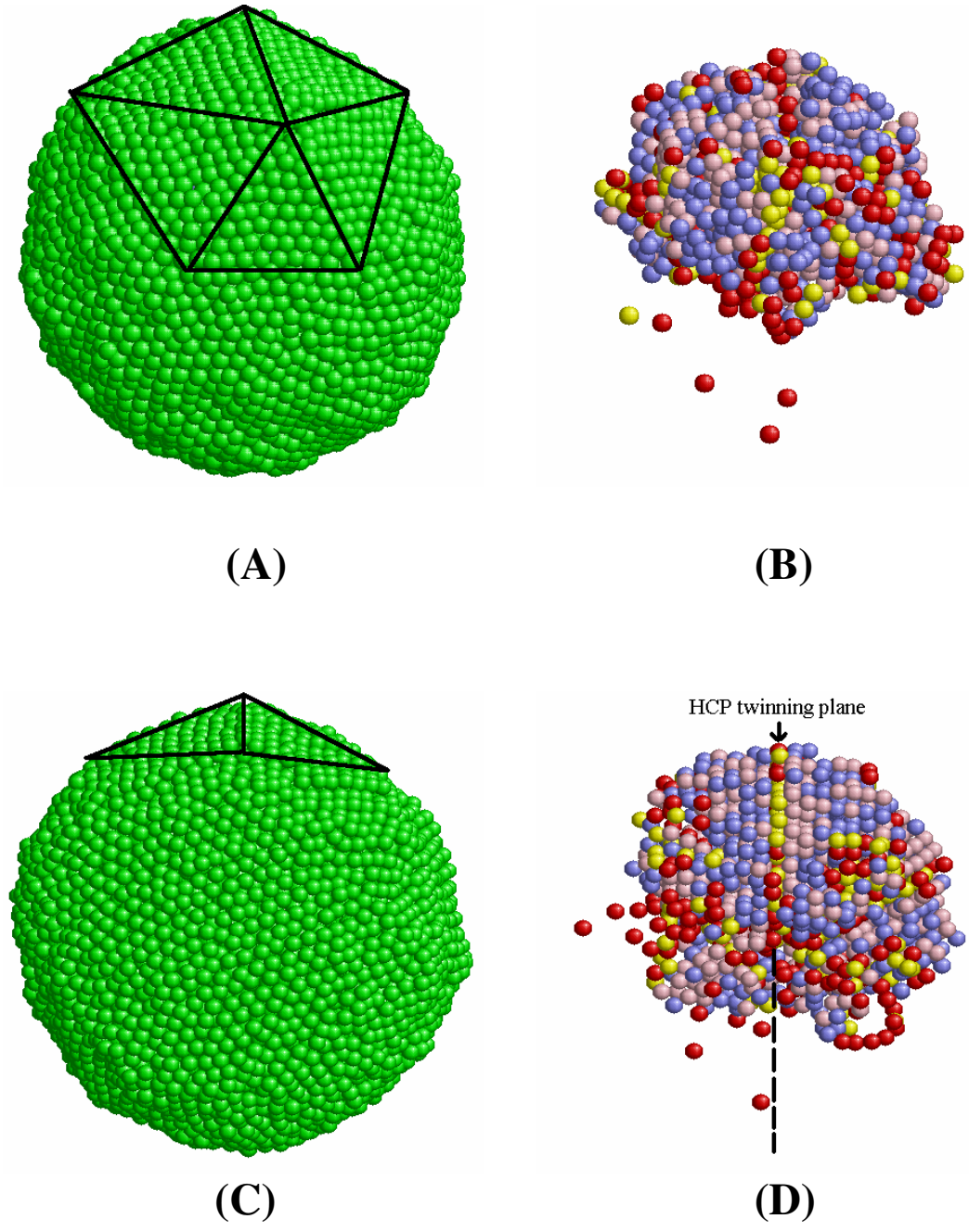


**Figure 5.7** The surface and core structure of the Au nanoparticle after 200ps from 2 different visual perspectives. The following colour scheme is used to classify the core atoms, FCC (pink), defected FCC (blue), HCP (yellow), defected HCP (red) and surface atom (green). For the surface atoms the black triangles indicate sections of (111) planes. The formation of a twin plane is shown in figure (d).

Figure 5.8 gives a plot of the Q6 order parameter with temperature for the gold nanoparticles quenched during the first 200 ps of crystallization of an Au10179 nanoparticle at 949K. The order parameter was calculated after running for 0.4ns at that particular temperature. A gradual increase of value of the Q6 order parameter is observed. In Figure 5.9 we give the results of other structural measures of crystallization over the same time range at 949K. A rapid percentage increase of FCC and HCP local structures is observed, while there is no significant change in ICO (Icosahedral) and stacking fault content in the nanoparticle. Note that Q6 value at 952K in Figure 5.1 is 0.058 while in Figure 5.8 the value increases from 0.033 (20ps) to 0.075 (200ps) at 949K. The higher value of Q6 at 952K is due to a longer simulation time compared to that at 949K. In our simulation procedure, the gold nanocluster was first cooled down to 952K with 200ps in Molecular Dynamics. Then further simulations were performed with 200ps at 952K (for figure 5.1) and 20ps at 949K (for figure 5.8) separately. As the further simulation time at 952K is longer compared to that at 949K, the nanocluster at 952K has a higher level of crystallization, and thus a higher value of Q6. In fact, the crystallization happens between 952K and 949K, but not at 949K sharply. Due to the same reason, the percentage of FCC and HCP at 952K in Figure 5.2 is higher than that at 949K in Figure 5.9.

Finally we show the core atoms for structures at temperatures corresponding to those in Figures 5.1 and 5.2 in Figure 5.10. Figure 5.10 (left) shows that as temperature decreases the particle evolves to a nearly perfect icosahedral structure consisting of blocks of FCC fragments joined by HCP twinning planes. Figure 5.10 (right) gives the evolution of the HCP twinning planes with temperature and shows that even at 298 K imperfections exist which is why the percentage of HCP particles is low compared to an ideal icosahedron in Figure 5.2.

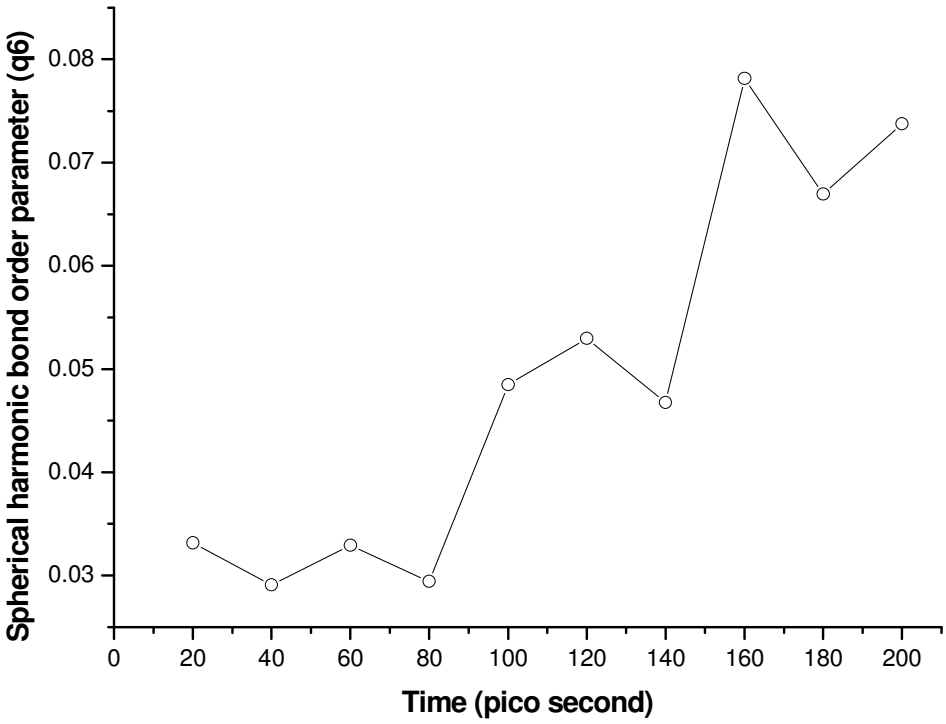


**Figure 5.8** The variation of bond order parameter (Q6) during the first 200 ps of crystallization of an Au 10179 nanoparticle at 949K.

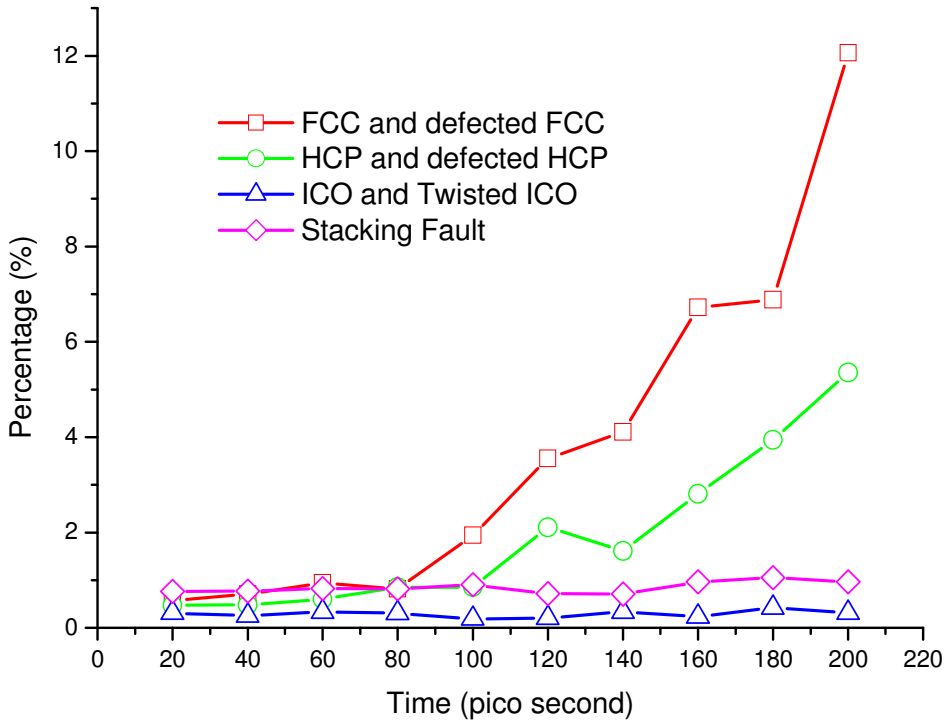


**Figure 5.9** The percentage variation of FCC, HCP, ICO and stacking fault content in an Au10179 nanoparticle during the first 200 ps of crystallization at 949K.

952K

862K

655K

469K

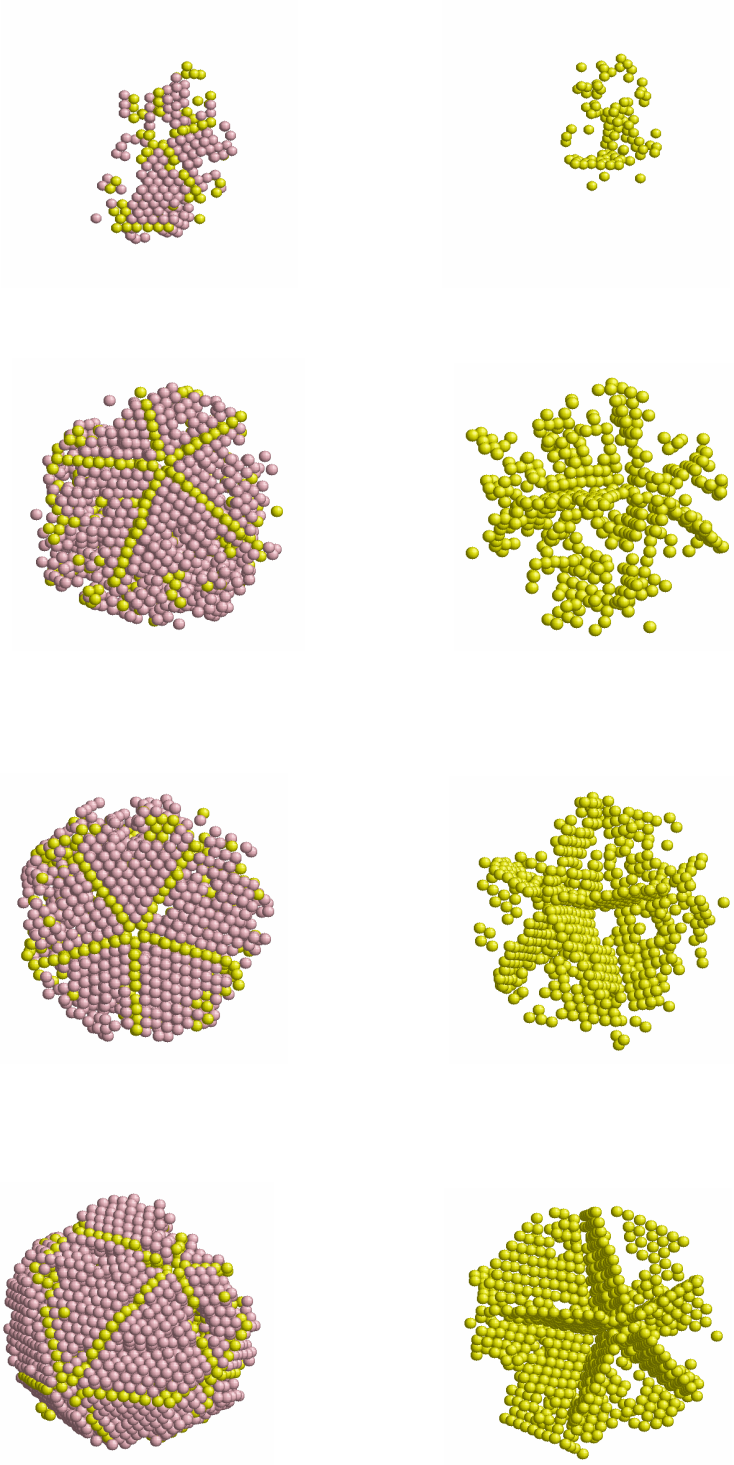

**Figure 5.10 is continued on the next page.**

**298K**

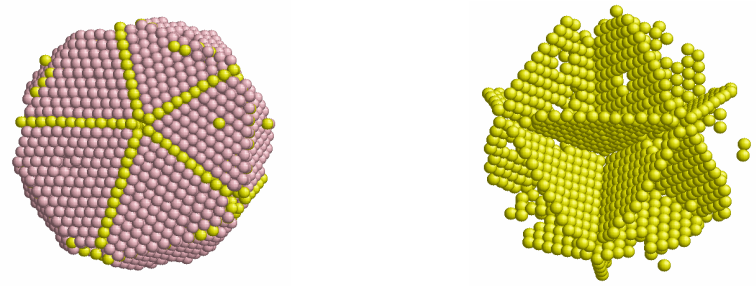

**Figure 5.10** The temperature evolution of the core atoms from 952 K to 298 K in an Au 10179 nanoparticle. FCC fragments (pink in colour) and HCP planes (yellow in colour) are shown on the left and the evolution of the HCP plane network on the right.

## 5.2 Crystallization of gold nanostructures of different sizes and quenching rates modeled by the Glue and Force-matching potentials

### 5.2.1 Glue potential

In our study, both glue and force-matching potentials predict the quenching from the melt gives nanoclusters of icosahedral morphology for the different sizes and quenching rates examined in this thesis. Here, first we discuss the crystallization of gold nanoclusters modeled by glue potential. We have already investigated the crystallization process of Au10179 atom gold nanoclusters modeled by Glue potnetial with the lowest quenching rate (Q3) in section 5.1 [9]. We found that the crystallization of the surface precedes that of the core and there is evidence of HCP twin planes forming directly below the region where the edges of two (111) surface planes meet. The nanocluster forms a defected icosahedral structure during cooling

and we observe the formation of FCC fragments and HCP planes characteristic of an icosahedral structure in the core as a function of temperature. Figures 5.11 – 5.13 shows the crystallization of Au10179 at different quenching rates and the resultant core structures at 298K. With the other two quenching rates (Q1 and Q2) (Figure 5.11 and 5.12), the crystallization process of Au10179 atom gold nanoclusters is similar to that with lower quenching rate (Q3) (Figure 5.13). The only difference is that in the early stage of crystallization with Q2, there are two regions of nucleation in the core, while there is only one in the crystallization with Q1 and Q3.

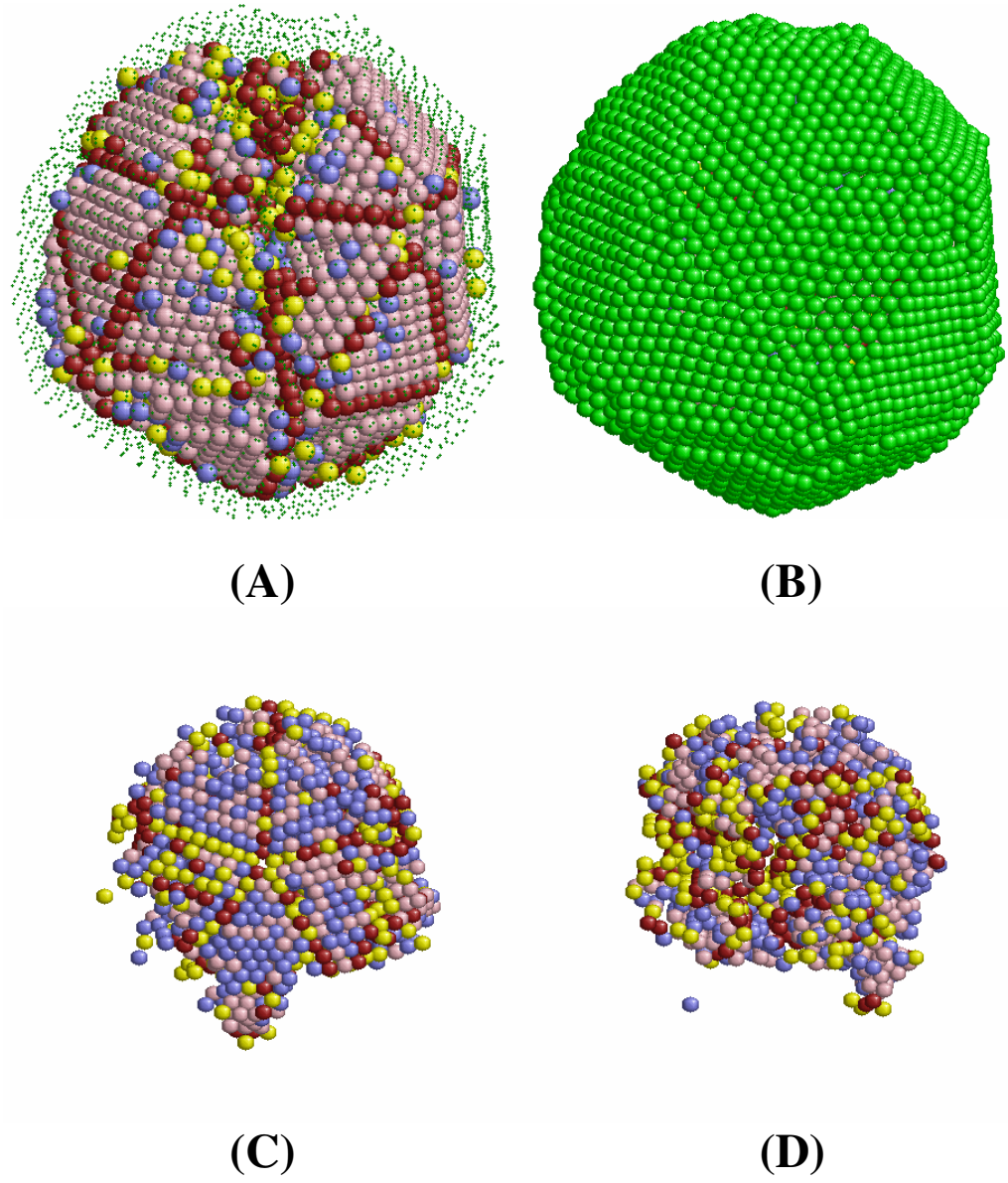


**Figure 5.11** The crystallization of Au10179 with quenching rate Q1 modeled by Glue potential and the resultant core structures at 298K: (A) Core structure and (B) Surface structure, (C) and (D) The snapshots of early crystallization of Au10179 (Q1) at 920K from two different points of view. The following colour scheme is used to classify the core atoms, FCC (pink), defected FCC (blue), HCP (yellow), defected HCP (red) and surface atom (green).

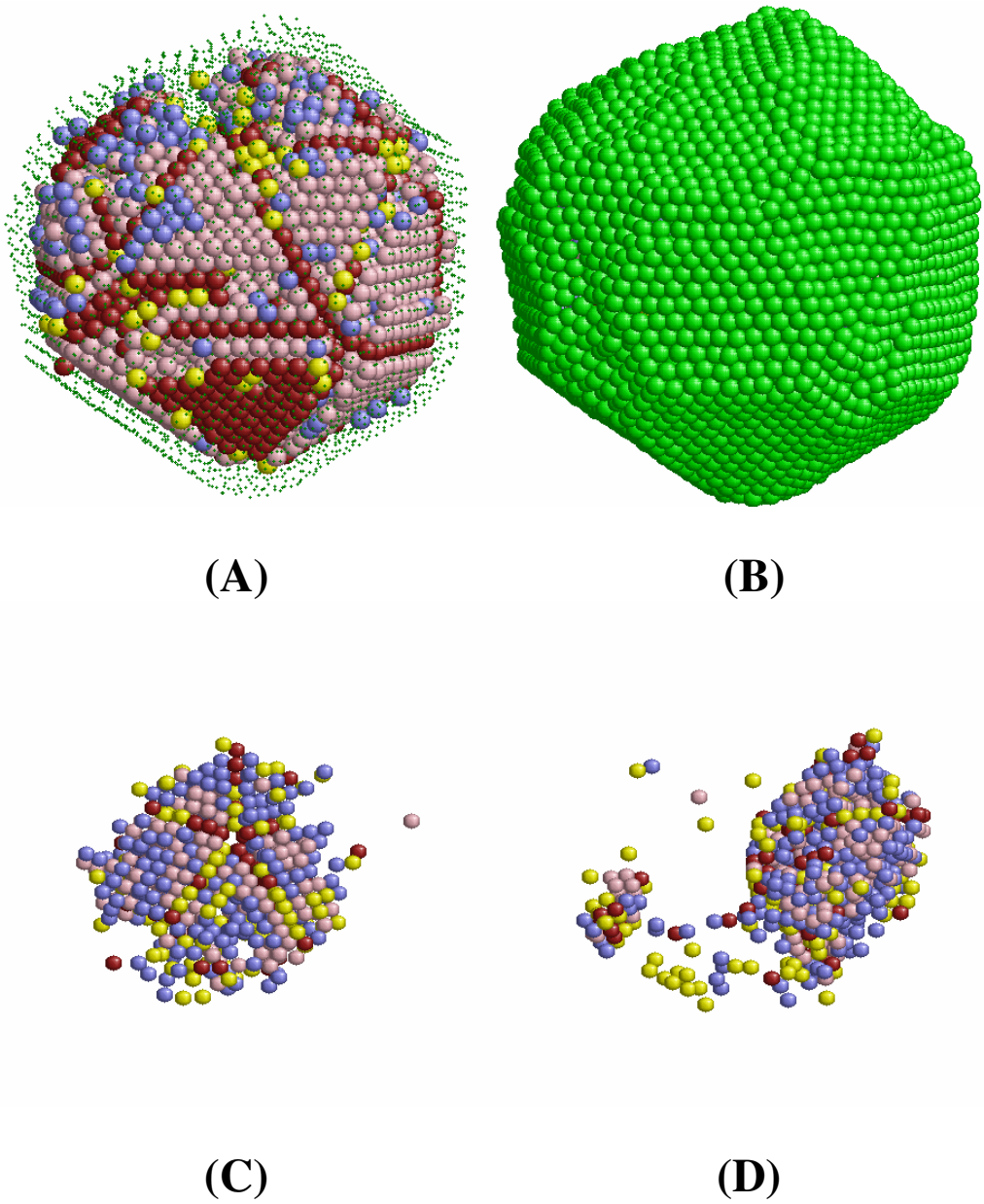


**Figure 5.12** The crystallization of Au10179 with quenching rate Q2 modeled by Glue potential and the resultant core structures at 298K: (A) Core structure and (B) Surface structure, (C) and (D) The snapshots of early crystallization of Au10179 (Q1) at 930K from two different points of view. The following colour scheme is used to classify the core atoms, FCC (pink), defected FCC (blue), HCP (yellow), defected HCP (red) and surface atom (green).

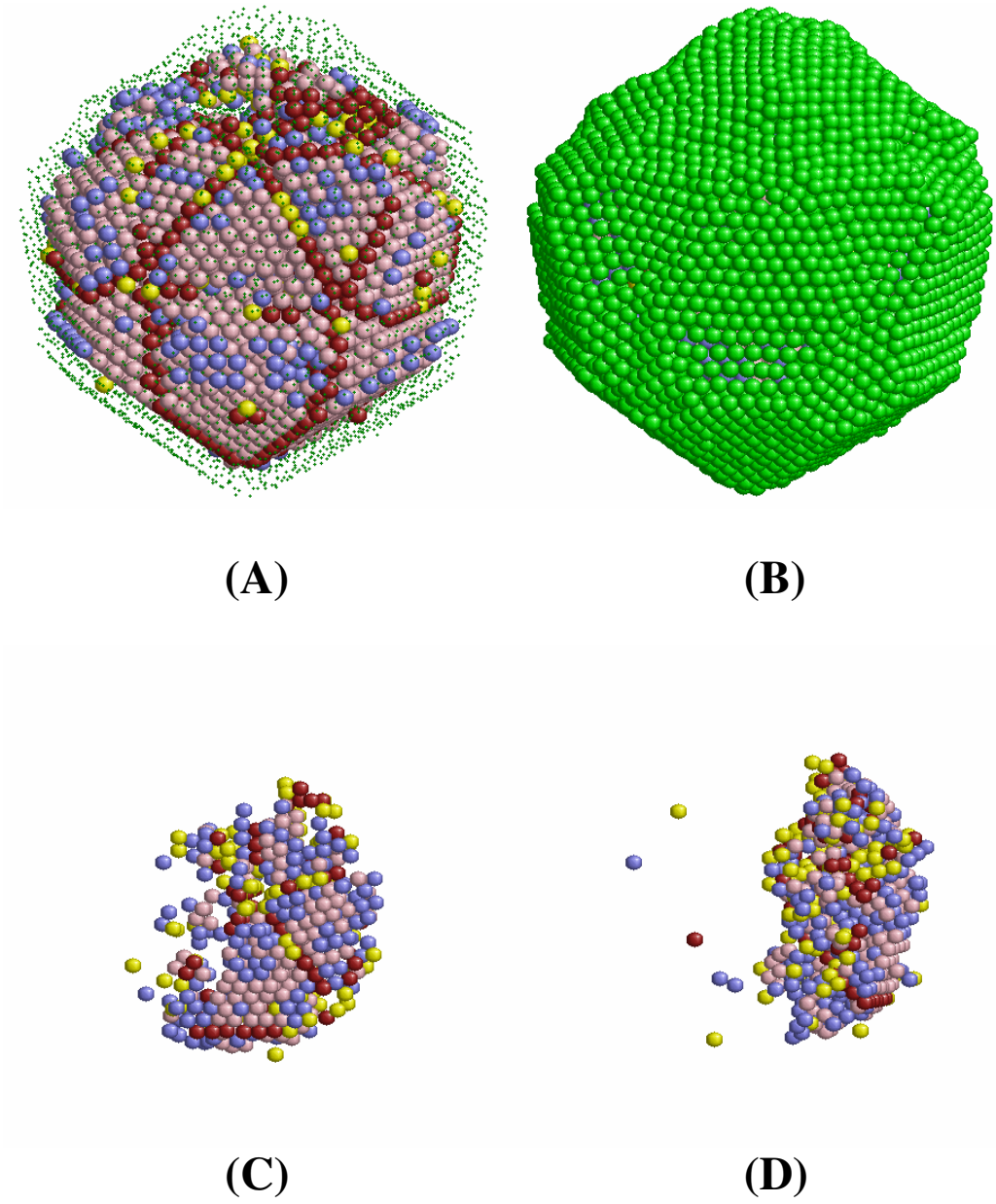


**Figure 5.13** The crystallization of Au10179 with quenching rate Q3 modeled by Glue potential and the resultant core structures at 298K: (A) Core structure and (B) Surface structure, (C) and (D) The snapshots of early crystallization of Au10179 (Q1) at 949K from two different points of view. The following colour scheme is used to classify the core atoms, FCC (pink), defected FCC (blue), HCP (yellow), defected HCP (red) and surface atom (green).

In the Q2 nanocluster, we also found that the core crystallization occurs directly below the region of surface crystallization, but the rates of growth around two origins of crystallization are not the same in the core. This provides evidence that the surface crystallization induces the core crystallization in gold nanoclusters. During the cooling process, two regions of crystallization in the core merged together, while there are some amorphous local structures in between them. Amorphous local structures in the crystalline core can be also found in the Q1 and Q3 nanoclusters, but the amount of amorphous local structure is larger in the Q2 nanocluster. We believe this structural arrangement was caused by insufficient kinetic energy of the core atoms and also the restricted atomic environment after the surface crystallization. Above the region of amorphous local structures, an extended (111) flat surface was not observed.

The Au5083 atoms nanoclusters of different quenching rates have similar early-stage crystallization behavior to Au10179 atom nanoclusters. Figures 5.14-5.16 shows the crystallization of the Au5083 at different quenching rates and the resultant core structures at 298K. The core crystallization also started below one (111) facet of five-fold symmetrical surface and proceeded to the other regions. However on the surface of the Au5083 nanocluster, the crystallization proceeded much faster than that in the core, compared to the Au10179 nanoclusters. Moreover, the surface of the Au5083 nanoclusters is less reconstructed compared to Au10179 nanoclusters.

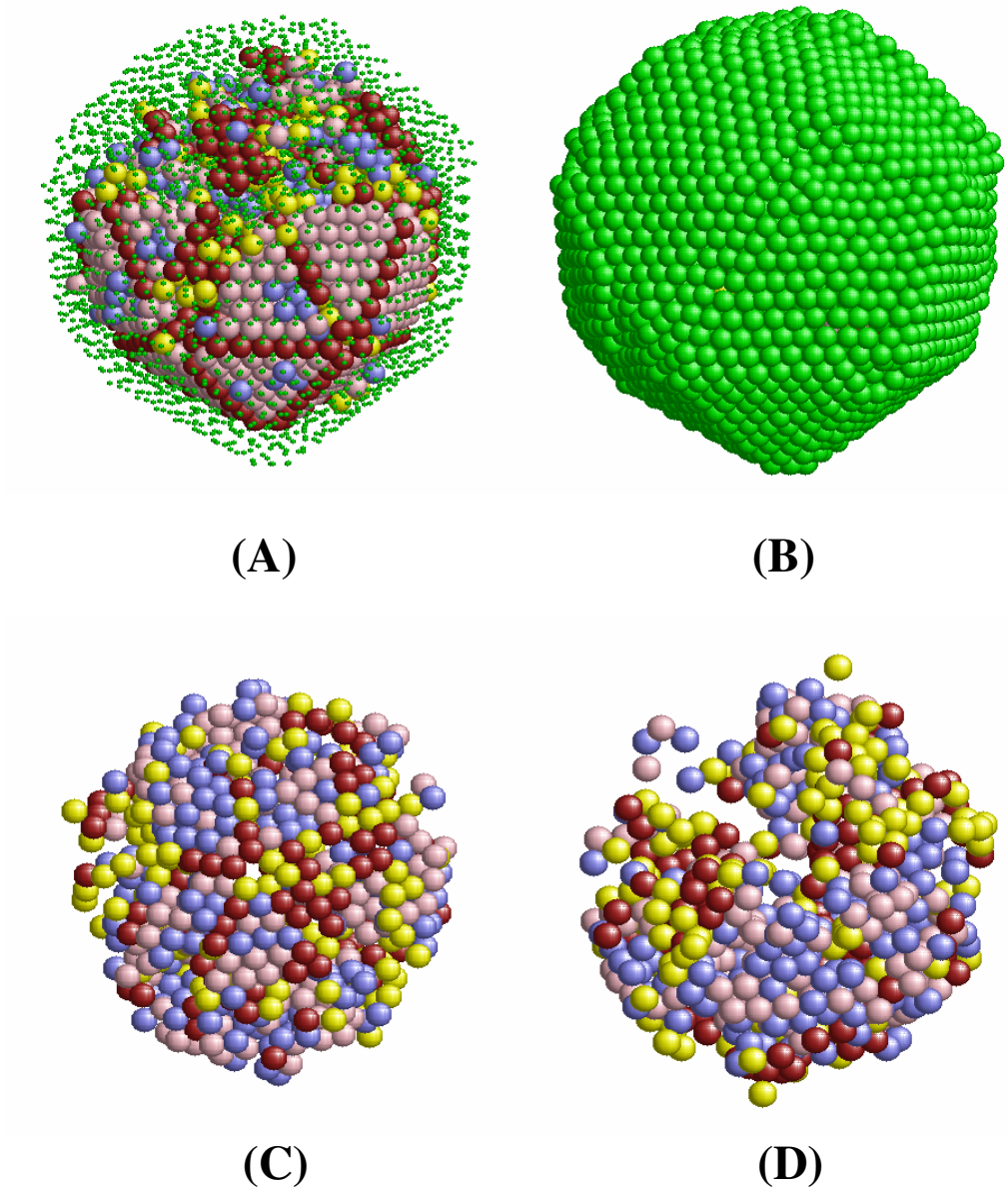


**Figure 5.14** The crystallization of Au5083 with quenching rate Q1 modeled by Glue potential and the resultant core structures at 298K: (A) Core structure and (B) Surface structure, (C) and (D) The snapshots of early crystallization of Au5083 (Q1) at 890K from two different points of view. The following colour scheme is used to classify the core atoms, FCC (pink), defected FCC (blue), HCP (yellow), defected HCP (red) and surface atom (green).

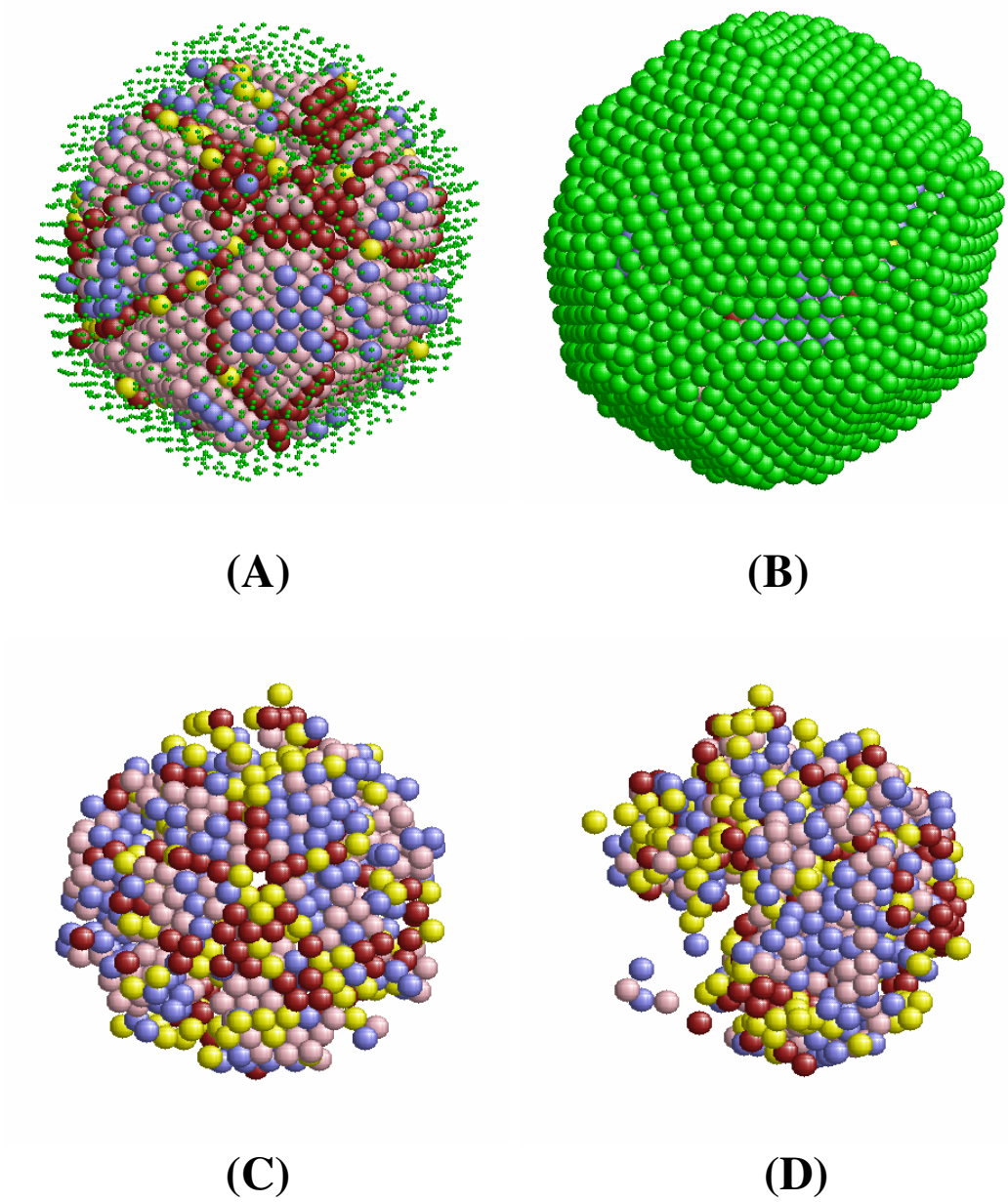


**Figure 5.15** The crystallization of Au5083 with quenching rate Q2 modeled by Glue potential and the resultant core structures at 298K: (A) Core structure and (B) Surface structure, (C) and (D) The snapshots of early crystallization of Au5083 (Q1) at 890K from two different points of view. The following colour scheme is used to classify the core atoms, FCC (pink), defected FCC (blue), HCP (yellow), defected HCP (red) and surface atom (green).

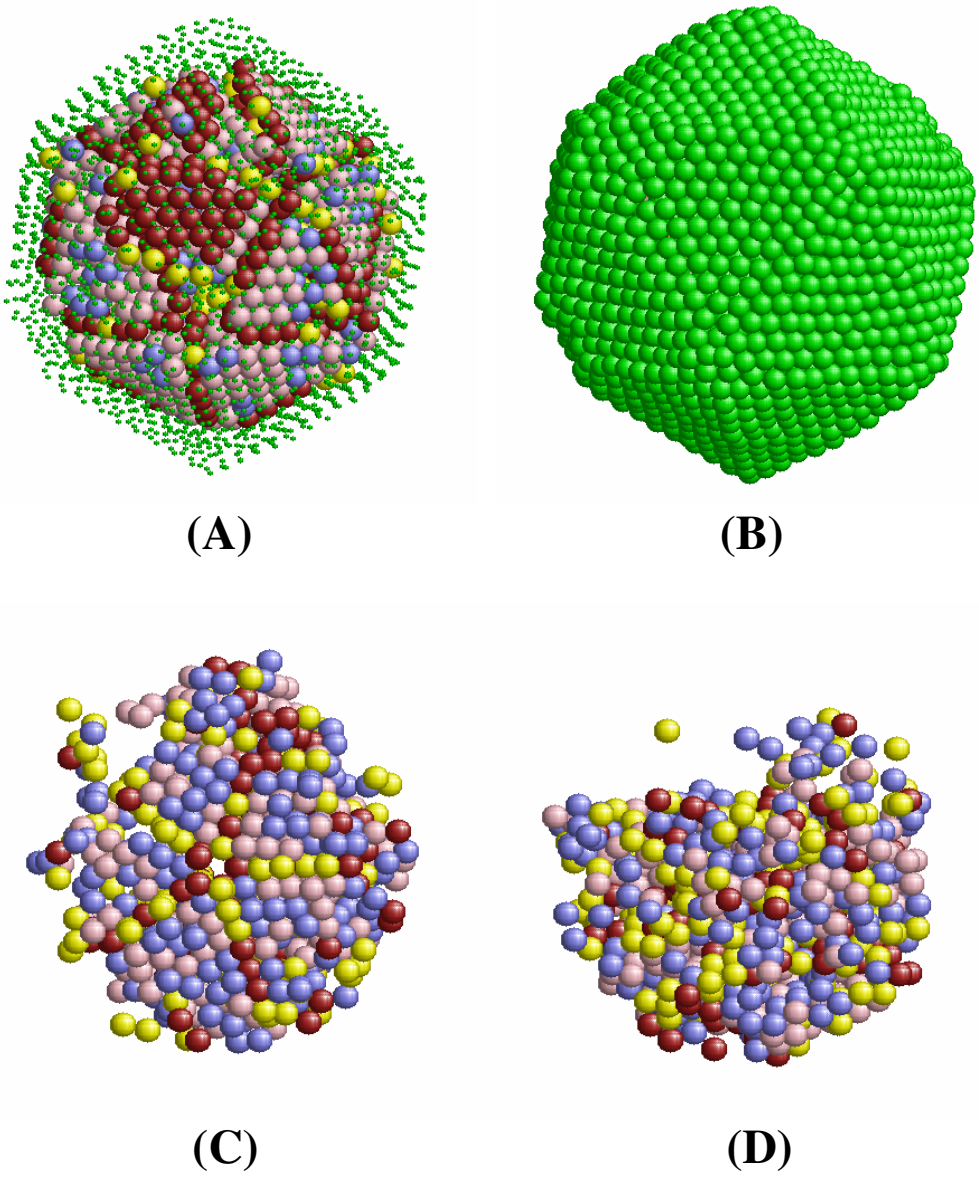


**Figure 5.16** The crystallization of Au5083 with quenching rate Q3 modelled by Glue potential and the resultant core structures at 298K: (A) Core structure and (B) Surface structure, (C) and (D) The snapshots of early crystallization of Au5083 (Q1) at 901K from two different points of view. The following colour scheme is used to classify the core atoms, FCC (pink), defected FCC (blue), HCP (yellow), defected HCP (red) and surface atom (green).

Due to much faster surface crystallization, the late-stage crystallization of Au5083 is different from Au10179. While the core crystallization proceeded inside the nanoclusters, in the amorphous region, several aggregates of local FCC structures were formed just below the extended crystalline surface. During the cooling process, the aggregates finally became part of the crystalline core of the gold nanoclusters. After the cooling process, a region of amorphous structure was also observed in Au5083 nanoclusters. As a result, both the surface and core structure of Au5083 nanoclusters, quenched with different quenching rates, are close at 298K.

Crystallization of the smallest gold nanoclusters (Au923) modeled using the glue potential was discussed in chapter 3 but for completeness we also include the main result here. We found that the Au923 nanocluster with a lower quenching rate gave a crystalline structure which is closer to the ideal icosahedral structure. The crystallization was initiated from the surface and it proceeded to the nanocluster core. At the early stage of core crystallization, we found that a small aggregate of FCC and HCP local structures were first formed at the centre of the nanocluster. During the cooling, an icosahedral crystalline core grew from the aggregate of local structures. Well-defined (111) facets were formed in the Au923 nanocluster with a little reconstruction.

### 5.2.2 Force-matching potential

Figures 5.17 and 5.18 show the variation of the bond order parameter with temperature for gold nanoclusters modeled by Glue and Force-matching potentials, respectively. The shape rise of the value of this parameter indicates the start of crystallization of the nanoclusters. From the plot, we found that not only the size of the nanoclusters and nature of the potentials, but also the quenching rate affects the freezing temperature. Figure 5.17 suggests that for the glue potential, the higher

quenching rate (Q1) causes a slightly lower temperature of freezing. In addition, we found that for both atomistic potentials, the quenching rate Q2 leads to the most crystalline core structure, with the highest value of Q6 at 298K.

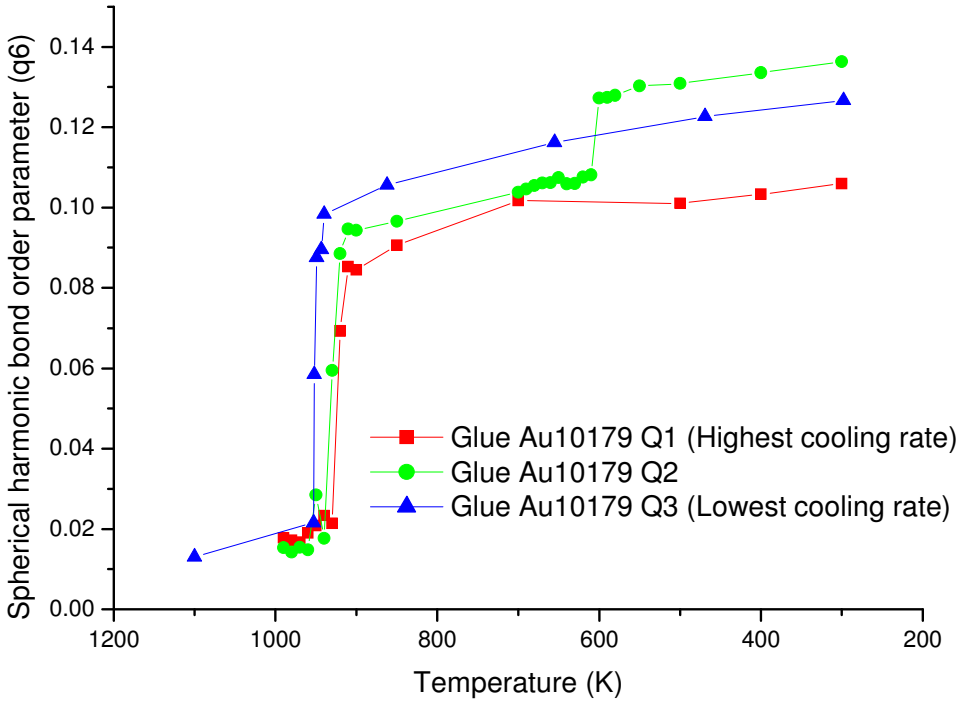


**Figure 5.17** The variation of the bond order parameter (Q6) during cooling process of 10179 atoms gold nanoclusters modeled by the Glue potential.

This indicates that adjusting quenching rate may be a way to control the level of crystallization inside the nanoparticle core. Finally, by comparing Figure 5.17 and 5.18, it is clearly shown that the gold nanoclusters simulated with the force-matching potential have generally higher freezing temperature than those with glue potential do. Other than the freezing temperature, the gold nanoclusters modeled by the Force-matching potential order slightly differently, compared to that modeled by the Glue potential during crystallization process. Figure 5.19 shows surface morphologies of Q3 Au923 and Q3 Au10179 modeled by Glue and Force-matching potential respectively.

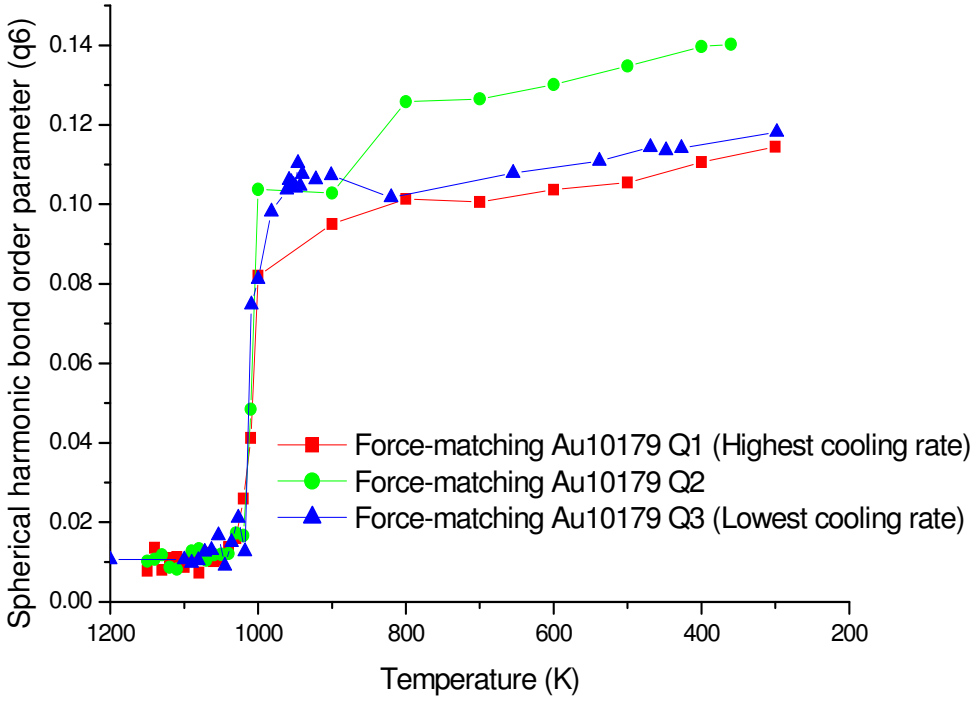


**Figure 5.18** The variation of the bond order parameter (Q6) during cooling process of 10179 atom gold nanoclusters modeled by the Force-matching potential.

Compared to the Glue potential, the Force-matching potential favours the formation of extended (111) facets on nanocluster surface without reconstruction. In addition, sharp edges between two adjacent (111) facets and a vertex of five-fold symmetry were often observed in all sizes of gold nanoclusters using the force-matching potential. For Au10179 nanoclusters of all quenching rates, the crystallization of the surface still precedes that of the core, but at the early stage of core crystallization, we found that the local FCC and defected FCC structures which are separated by an array of HCP atoms, were widely distributed below the crystalline surface of the gold nanocluster, instead of forming a large block of crystalline FCC in the case of gold nanoclusters modeled by the Glue potential, as shown in Figure 5.20 – 5.22.

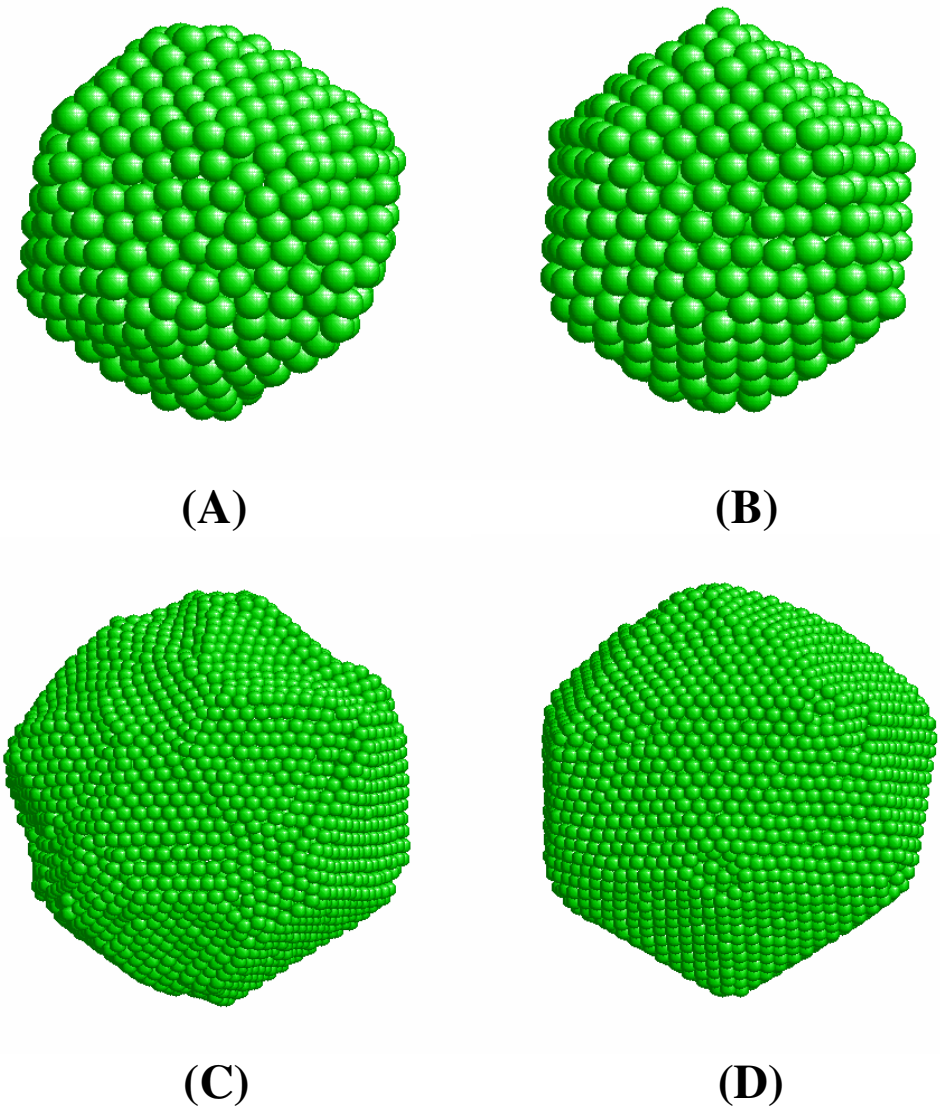


**Figure 5.19** The surface morphologies of gold nanoclusters: (A) Q3 Au923 (Glue), (B) Q3 Au923 (Force-matching) (C) Q3 Au10179 (Glue), (D) Q3 Au10179 (Force-matching).

At the late stage of crystallization, two large blocks of crystalline FCC were formed in Q1 and Q3 Au10179 nanoclusters, and their dimensions were very close. At 298K, these two crystalline blocks were separated by a layer of amorphous atoms (sandwich-like). But in Q2 Au10179 nanocluster, only a small gap filled with amorphous atoms was observed. For Au5083 nanocluster of all quenching rates, the

crystallization process and also the resultant structures are close to that modeled by the Glue potential.

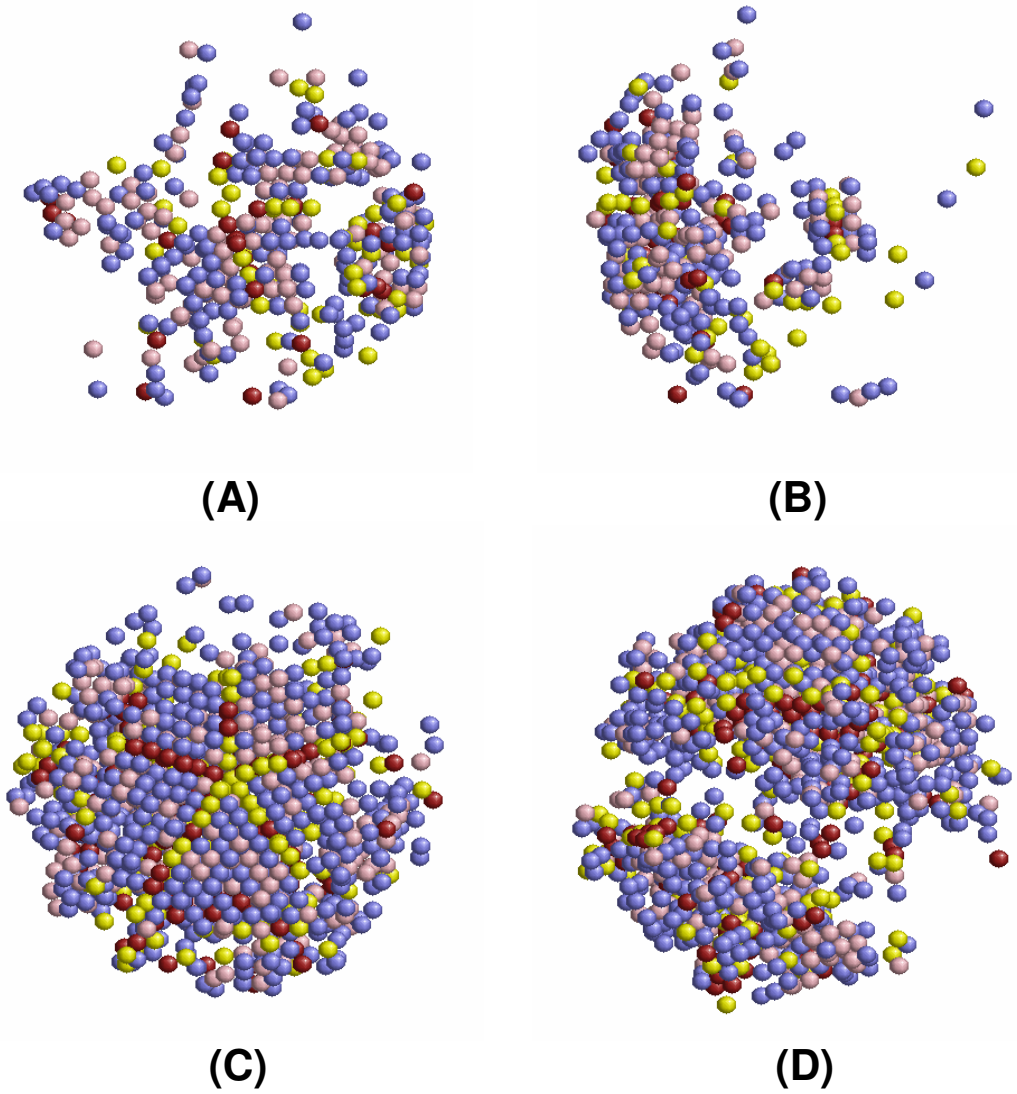


**Figure 5.20 is continued on the next page.**

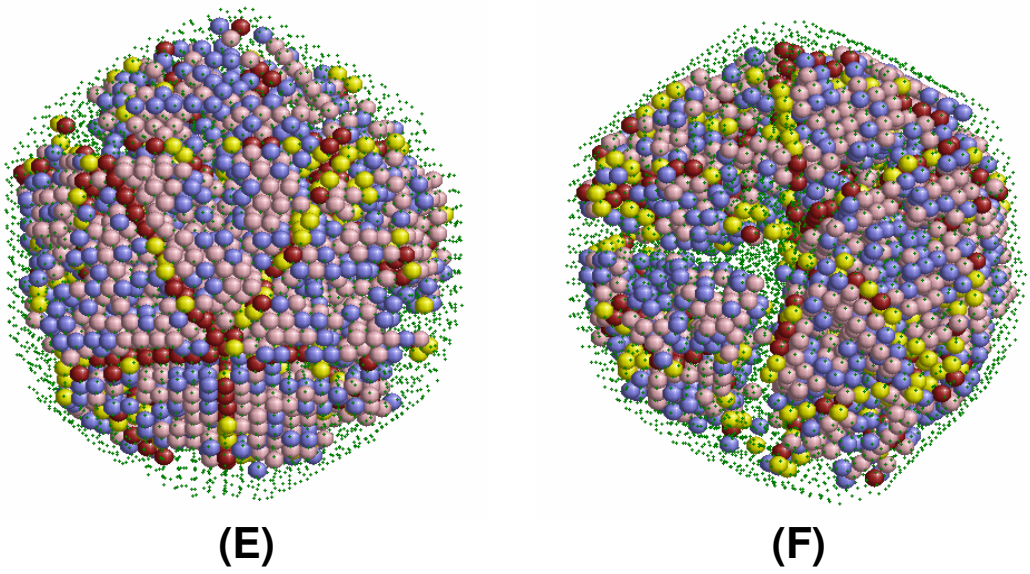


**Figure 5.20** The early crystallization of Au10179 (Q1) modeled by Force-matching potential: (A), (B) The structure from two different points of view at 1010K; (C), (D) The structure from two different points of view at 1000K; (E), (F) The resultant core structures from two different points of view at 298K. The following colour scheme is used to classify the core atoms, FCC (pink), defected FCC (blue), HCP (yellow), defected HCP (red) and surface atom (green).

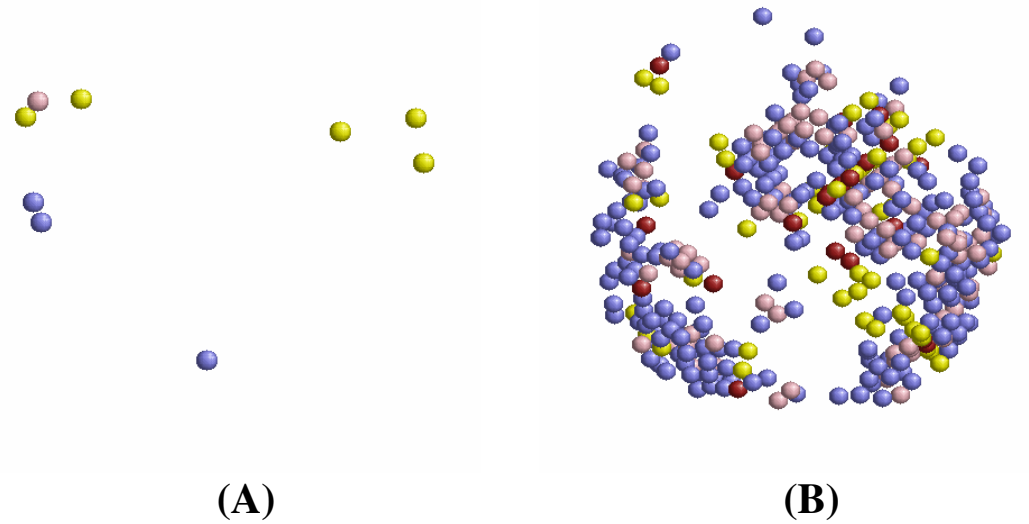


**Figure 5.21 is continued on the next page.**

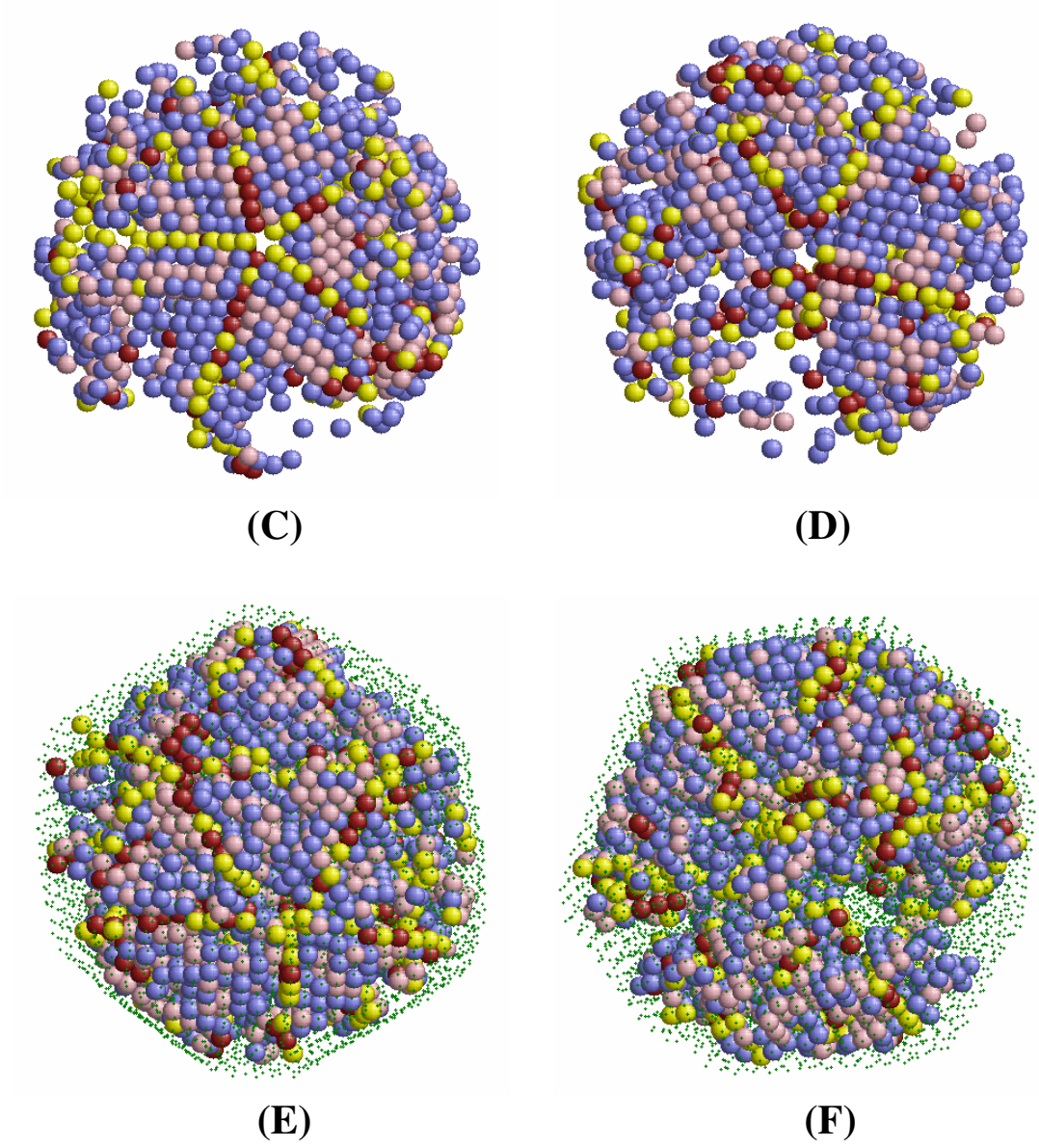


**Figure 5.21** The early crystallization of Au10179 (Q2) modeled by Force-matching potential: (A) The structure at 1020K; (B) The structure at 1010K; (C), (D) The structure from two different points of view at 1000K; (E), (F) The resultant core structures from two different points of view at 298K. The following colour scheme is used to classify the core atoms, FCC (pink), defected FCC (blue), HCP (yellow), defected HCP (red) and surface atom (green).

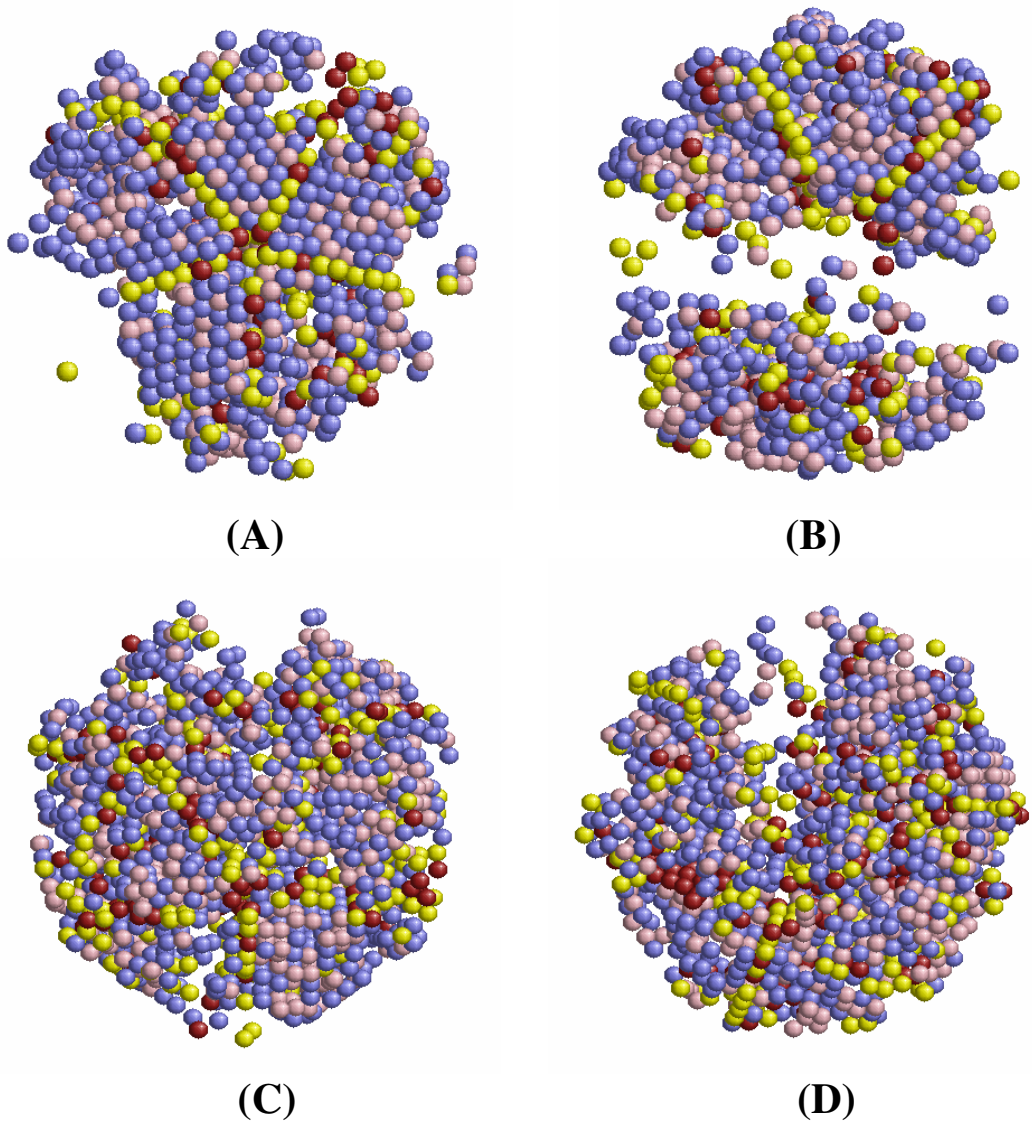

**(A)** **(B)**

**(C)** **(D)**

**Figure 5.22 is continued on the next page.**

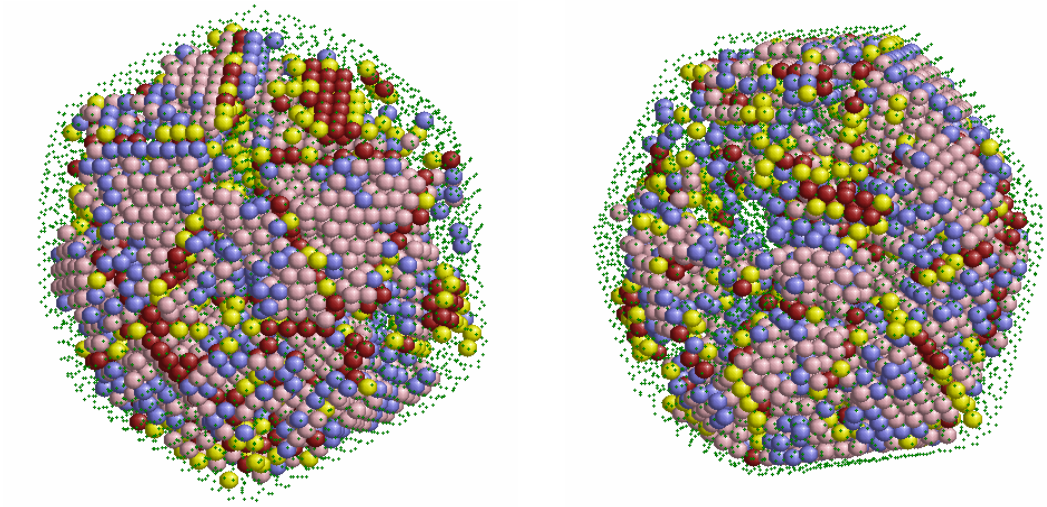

**(E)** **(F)**

**Figure 5.22** The early crystallization of Au10179 (Q3) modeled by Force-matching potential: (A), (B) The structure from two different points of view at 1010K; (C), (D) The structure from two different points of view at 1000K; (E), (F) The resultant core structures from two different points of view at 298K. The following colour scheme is used to classify the core atoms, FCC (pink), defected FCC (blue), HCP (yellow), defected HCP (red) and surface atom (green).

In contrast, the Au923 nanoclusters modeled by the Force-matching potential behave very differently from that modeled by the Glue potential. Figure 5.23 shows the core structure of Q2 Au923 nanoclusters modeled by the Glue and the Force-matching potential at 298K. At all quenching rates, a nearly perfect icosahedral nano surface was formed above 800K, but a significant crystalline core inside the nanocluster was not observed during the cooling process. Instead, a mixture of regular FCC and HCP, defected FCC and HCP, and amorphous structures was observed in the core region of gold nanoclusters of all quenching rates.

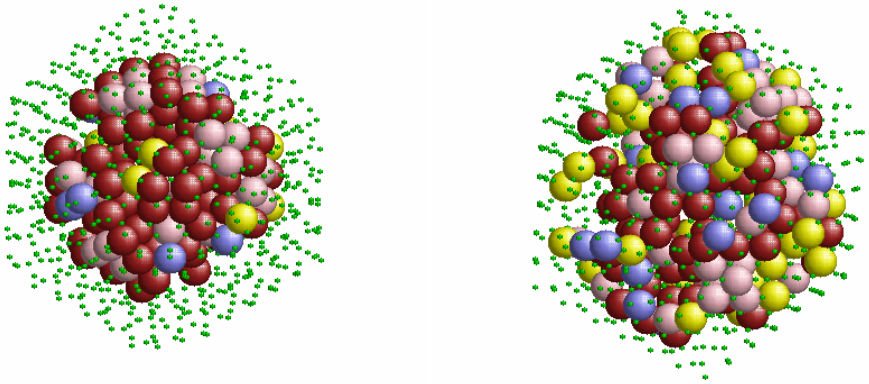

**(A)** **(B)**

**Figure 5.23** The core structure of Q2 Au923 nanoclusters modeled by (A) Glue and (B) Force-matching potential at 298K. The following colour scheme is used to classify the core atoms, FCC (pink), defected FCC (blue), HCP (yellow), defected HCP (red) and surface atom (green).

## 5.3 Conclusion for crystallization of gold nanostructures

To conclude, although the two atomistic potentials we applied gave different surface structures and also mechanisms for core crystallization during the cooling process, both potential predicted icosahedral-like morphology within the nanocluster size range examined in this study, which is in good agreement with the TEM observation of gold nanoclusters under vacuum [4]. Also, the surface crystallization of icosahedral gold nanoclusters were shown to be a significant effect on the behavior of core crystallization. There is strong evidence showing that crystallization of the surface precedes that of the core and leads the orientation of core crystallization for both potentials. Also, it is clearly that there is a strong preference of the formation of (111) surface in gold nanoparticles modeled by Force-Matching potential, compared to that modeled by Glue potential. Thus, due to the difference in surface crystallization, the formation pathways to icosahedral structure predicted by these two potential are also different. On the other

hand, the freezing temperature of the gold nanparticles modeled by Glue potential is lower than that modeled by Force-Matching potential however Glue potential gives a higher freezing (melting) temperature of bulk FCC gold than Force-Matching potential does. Again, we believe the stronger preference of surface crystallization modeled by Force-Matching potential causes a higher freezing temperature of the gold nanoparticles.

Gold nanoclusters with less than 1000 atoms have been studied by Nam et al. using EAM potentials [1, 2], and they concluded that the formation of icosahedral morphology of small gold nanoclusters during cooling is caused by surface-induced mechanism and that this is a kinetic process, rather than a thermodynamical process [1]. In this study we further show how surface crystallization affects the overall crystallization of gold nanoclusters of different sizes and quenching rates. Finally, two potential

As the experimental observation of crystallization process of nanoparticles is lacking, we cannot make the conclusion on which potential is more suitable to simulate gold nanoparticle. In the future, more assessment to the suitability of these two potentials can be made by modeling the zero-dimensional gold nanoparticle in different mediums (e.g. model solvent and water molecules) and one-dimensional gold nanostructures (e.g. rod and wire).

**References**

[1] H.S. Nam, N. M. Hwang, B. D. Yu, D. Y. Kim and J. -K. Yoon, Phys. Rev. B, **71**, 233401 (2005).

[2] H.S. Nam, N. M. Hwang, B. D. Yu and J. –K. Yoon, Phys. Rev. Lett., **89**, 275502 (2002).

[3] Y. H. Chui, R. J. Rees, I. K. Snook, B. O'Malley and S. P. Russo, J. Chem. Phys., **125**, 114703 (2006).

[4] K. Koga and K. Sugawara, Surf. Sci., **529**, 23 (2003); K. Koga, T. Ikeshoji and K. Sugawara, Phys. Rev. Lett., **92**, 115507 (2004).

[5] B. O'Malley, Molecular dynamics of crystallization in the hard sphere system, Ph.D. thesis, RMIT (2001)

(Available at http://mams.rmit.edu.au/6g0wr8cwl4b1.pdf);

B. O'Malley and I. K. Snook, Phy. Rev. Lett., **90**, 085702 (2003).

[6] B. O'Malley and I. K. Snook, J. Chem. Phys., **123**, 054511 (2005).

[7] F. Ercolessi, E. Tosatti and M. Parrinello, Phys. Rev. Lett., **57**, 719 (1986).

[8] Available at http://www.pas.rochester.edu/~wangyt/algorithms/index.html

[9] Y. H. Chui, I. K. Snook. and S. P. Russo, Phys. Rev. B, revised for publication (2007).

# Chapter 6

# Conclusion and future work

In this thesis we studied gold nanostructures of different sizes and morphologies using Molecular Dynamics and two EAM based atomistic potentials, the 'Glue' and 'Force-matching' potentials. Although the glue and the force-matching potentials were originally developed from bulk gold systems, the structures predicted by these two potentials are in good agreement with the experimental observation of gold nanoclusters in the size range 3-8 nm in vacuum. The crystallization mechanism of the icosahedral-like gold nanoclusters of different sizes was also studied. The effect of the glue and the force-matching potentials on the crystallization of icosahedral gold nanoclusters was shown. We also examined relative stability and crystallization kinetics of these gold nanoclusters.

Importantly, we found that surface atoms play a vital role in the crystallization of gold nanostructures of different sizes. In this study, even for a large nanoparticle with over 10000 atoms and a relatively lower surface atom /bulk atom ratio, the surface crystallization critically affects the overall crystallization process. Moreover, using the glue potential, we found that the surface reconstructed icosahedral gold nanoclusters of all sizes are the most thermodynamically favorable. The reconstruction of the nanoparticle surface must, therefore, effectively contribute to the stability of the gold nanoparticles.

Compared to some traditional analysis methods, such as the radial distribution function (RDF), topological planar graph ring sequencing lets us understand more about the local environment of every atom inside the nanoparticle. The analysis of core atoms by the planar graph ring sequencing method provided a deeper understanding of how the atoms locally pack with each other while crystallization proceeds.

In the future, we hope to our extend study to one-dimensional gold nanostructures (rods, wires and tubes). The study of surface induced phase transformation, thermal stability and surface reconstruction of one-dimensional nanostructures would make an interesting study. Alternatively, hollow gold nanostructures, which have been recently discovered and studied experimentally and which contain a high ratio of surface atoms would make an interesting comparison to the nanoclusters studied in this thesis, and we are beginning to investigate these nanostructures. The prediction of some properties, such as the thermal stability of hollow particles of different sizes and thickness, is highly desirable for material scientists, due to the potential usage of these structures in drug delivery, as an optical imaging contrast agent and for cancer treatment.

Finally, the theoretical study of the assembly of gold nanostructures on different surfaces is important to the development of nano-devices using gold particles. Combining with different theoretical methods, such as Accelerated Molecular Dynamics and Kinetic Monte Carlo methods, the assembly could be modeled and simulated and some properties, such as thermal conductivity and stability, could be predicted. Our planar graph ring sequencing methods would provide valuable insight into the self-assembly process as well as the crystallization of one-dimensional or hollow structures.